



Andreas Postl, BSc

**Simulation of High-Resolution Scanning Transmission
Electron Microscope Images using Gold-Nickel Models
and Comparison with Experiment**

MASTER'S THESIS

to achieve the university degree of

Diplom-Ingenieur

Master's degree programme: Technical Physics

submitted to

Graz University of Technology

Supervisor

Ao.Univ.-Prof. Dipl.-Ing. Dr.techn. Werner Grogger

Co-Supervisor

Dipl.-Ing. Dr.techn. Christian Gspan

Institute of Electron Microscopy and Nanoanalysis

Graz, December 2017

Affidavit

I declare that I have authored this thesis independently, that I have not used other than the declared sources/resources, and that I have explicitly indicated all material which has been quoted either literally or by content from the sources used. The text document uploaded to TUGRAZonline is identical to the present master's thesis.

Date

Signature

“The first principle is that you must not fool yourself and you are the easiest person to fool.”

– Richard Feynman

Abstract

This work reports on the simulation of high-resolution scanning transmission electron micrographs of Au-Ni models in the high-symmetry zone axis [001] of the face-centered cubic crystal structure and the contrast analysis of the obtained images. Models with variously arranged nickel substituents in a gold matrix were created and multislice simulations were performed. Changes in the simulated images caused by the variation of model and microscope parameters were investigated. In the process, particular attention was paid to the recordings originating from high-angle annular dark field detectors, which feature exceptionally good contrast with respect to differing atomic numbers. The meticulous evaluation of the results comprises the effects of model thickness, Ni concentration, convergence angle of the primary electron beam, and collection angle of the detectors on measured electron intensities. The alloy Au-Ni exhibits spinodal decomposition for certain chemical compositions and temperature ranges. In the course of approaching this phenomenon, a program that performs Monte Carlo simulations of the lattice relaxation of bimetallic alloys was developed in order to cope with lattice distortions accompanying the demixing.

Complementarily, Au-Ni specimens, in which the spinodal decomposition had been activated before, were imaged using a transmission electron microscope and a scanning transmission electron microscope. The results emerging from the simulations were surveyed concerning their informative value for the purpose of analyzing experimental micrographs at atomic resolution. Computer-aided concepts were realized to extract suitably conditioned information from greyscale images or image series respectively. It is evident that a quantitative comparability without systematic errors is hard to reach, since real laboratory conditions in modern electron microscopy do not conform to idealized simulation parameters. The superordinate goal of this work is to represent a contribution to the vision of making precise quantitative composition determination of suitable materials based on the contrast in scanning transmission electron microscope images possible.

Kurzbeschreibung

Diese Arbeit untersucht die Simulation von Hochauflösungsrastertransmissionselektronenmikroskopaufnahmen von Au-Ni-Modellen in der hochsymmetrischen Zonenachse [001] der kubisch flächenzentrierten Kristallstruktur und berichtet von der Kontrastanalyse der erhaltenen Bilder. Es wurden Modelle mit unterschiedlich angeordneten Nickel-Substituenten in einer Gold-Matrix erstellt, an denen Multislice-Simulationen durchgeführt wurden. Die Veränderungen in den simulierten Bildern aufgrund der Variation verschiedener Modell- sowie Mikroskopparameter wurden untersucht. Dabei wurde besonderes Augenmerk auf jene Aufnahmen gelegt, die von ringförmigen Großwinkel-Dunkelfeld-Detektoren stammen und daher außerordentlich guten Kontrast hinsichtlich variierender Ordnungszahl bieten. Die Auswertung der Resultate umfasst die Auswirkungen von Modelldicke, Ni-Konzentration, Konvergenzwinkel des Primärelektronenstrahls und Erfassungswinkel der Detektoren auf gemessene Elektronenintensitäten. Im Zuge der Untersuchung des Phänomens der spinodalen Entmischung, das die Legierung Au-Ni für bestimmte Bereiche von chemischer Zusammensetzung und Temperatur aufweist, wurde ergänzend ein Programm zur Monte-Carlo-Simulation der Gitterrelaxation von bimetallischen Legierungen entwickelt, um mit der Entmischung einhergehenden Gitterverzerrungen gerecht zu werden.

Komplementär wurden Au-Ni-Proben nach Aktivierung des Mechanismus der spinodalen Entmischung mithilfe eines Transmissionselektronenmikroskops und eines Rastertransmissionselektronenmikroskops abgebildet. Die Ergebnisse, die aus den Simulationen hervorgehen, wurden auf ihre Aussagekraft bezüglich der Analyse experimenteller Aufnahmen bei atomarer Auflösung hin überprüft. Dazu wurden computerunterstützte Konzepte realisiert, um aus Grauwertbildern bzw. -bildserien für diesen Zweck brauchbar aufbereitete Informationen zu gewinnen. Eine quantitative Vergleichbarkeit ohne systematische Fehler ist offenkundig schwierig zu erzielen, da reale Laborbedingungen in der modernen Elektronenmikroskopie keineswegs mit idealisierten Simulationsparametern übereinstimmen. Das übergeordnete Ziel dieser Arbeit ist es, einen Beitrag zur Ermöglichung präziser quantitativer Bestimmung der chemischen Zusammensetzung geeigneter Materialien aufgrund des Kontrasts in Rastertransmissionselektronenmikroskopbildern darzustellen.

Acknowledgments

Initially, I would like to thank Univ.-Prof. Dr. Ferdinand Hofer, head of the Institute of Electron Microscopy and Nanoanalysis of the TU Graz (FELMI) and the Graz Centre for Electron Microscopy (ZFE Graz), for giving me the chance to work on this master's thesis, for providing a workplace at the mentioned institution and for the discussions of technical nature.

My sincere thanks go to my supervisor Univ.-Prof. Dr. Werner Grogger for all the informative professional conversations and discussions, and especially for advising me that carefully while I was compiling and composing the present thesis. His exceptional ability to clearly express scientific issues and his keen sense for students' needs have been very inspiring for me.

I would like to express my cordial gratitude to Dr. Christian Gspan for the transmission of his knowledge and for carrying our experimental investigations out. I am very grateful to him for his great patience and his always encouraging words when I almost felt overwhelmed by work.

With the hope that I was not utterly tedious, warm thanks also go to Dr. Daniel Knez, who supplied me with so many great ideas and inputs. I thank him for the numerous in-depth talks, which were incredibly revealing to me.

Big thanks go to the graduate and postgraduate students at the institute, and all other members of the FELMI-ZFE who I have not mentioned yet. Many of them made valuable contributions to this work. I appreciated the warm and respectful working environment a lot.

A humble-minded word of thanks goes to my fellow students and friends Kathi, Krissi, Martin, Max, Philip, Roman, and Sebi, with whom I have experienced so much throughout the last years. Admittedly, it is hard to find a phrase worthy of their meaning in my life. I warm-heartedly hope that we will still meet a good many times in future.

Last, I would like to thank my family. I am deeply grateful to my parents and my younger brother for the unconditional encouragement during my studies and my whole life, and for ceaselessly believing in me in every sense.

Table of Contents

Abstract	vi
Kurzbeschreibung	vii
Acknowledgements	viii
Notes and clarifications	xi
Guidelines	xi
List of acronyms	xii
Used software	xiii
1. Introduction and goals	1
2. Fundamentals and methods	3
2.1. The gold-nickel system	3
2.2. STEM	6
2.2.1. Electron detectors	6
2.2.2. Image contrast	9
2.3. HRSTEM image simulation	11
2.3.1. The multislice method	11
2.3.2. Simulation software package QSTEM	12
2.4. Quantitative HRSTEM image analysis	12
2.5. Simulated lattice relaxation of binary alloys	16
2.5.1. Potentials	16
2.5.2. Metropolis-Hastings algorithm (Monte Carlo)	21
2.5.3. Velocity Verlet algorithm (Molecular Dynamics)	23
2.5.4. Autocorrelation function	23
2.6. Statistics and data analysis	25
3. Results and analysis	27
3.1. Simulation results	27
3.1.1. QSTEM images of models with a perfect fcc lattice	29
3.1.2. Lattice relaxations	47
3.1.3. QSTEM images of relaxed models	60
3.1.4. QSTEM CBED images with small convergence angle	63

Table of Contents

3.2. Experimental results	66
3.2.1. STEM micrographs	67
3.2.2. TEM and SAED images	79
4. Conclusion	81
4.1. Summary	81
4.2. Uncertainties regarding the comparability of simulation and experiment	83
4.3. Outlook	84
Bibliography	85
List of Figures	91
List of Tables	95
Appendix	97
A. Code snippets	97
A.1. Julia	97
A.2. MATLAB	106
B. How to get QSTEM simulations done	118

Notes and clarifications

Guidelines

The following applies to any section of this thesis.

1. If the proportion or concentration of an element is not precisely declared "at%", "vol%", "atomic fraction", or "volume fraction", the numbers stand for atomic fractions.
2. As a German native speaker, I frequently feel confused - and sometimes irritated - about different meanings of (mathematical) symbols and dissimilar symbols with the same meaning when reading English and German literature in quick succession. It might happen the reader hits such a situation of confusion in this thesis. On that account, the following explanatory notes should establish clearness:
 - \propto ... proportional to
 - \approx ... approximately (mostly used in a numerical context)
 - \cong ... approximately equal to (used for analytical simplifications)
 - \ln or \log ... natural logarithm (used interchangeably)
 - \Leftrightarrow ... equivalent to
3. [value1] .. [value2] specifies a range from [value1] to [value2].
4. An uncertainty statement $x = 135.2(12)$ is equivalent to $x = 135.2 \pm 1.2$. The parenthesized value always refers to the least significant digit(s).
5. Reciprocal lattice vectors and their norm are labeled \vec{G}_{hkl} and G_{hkl} . As for the basis, I use the crystallographic convention $\vec{b}_1 := \frac{\vec{a}_2 \times \vec{a}_3}{\vec{a}_1 \cdot (\vec{a}_2 \times \vec{a}_3)}$ without a factor of 2π , so that the relationship between reciprocal and real space becomes $G_{hkl} = d_{hkl}^{-1}$. Accordingly, all spatial frequencies q in reciprocal space correspond to $r_q = q^{-1}$ in real space.

List of acronyms

ABF	annular bright field
ADC	analog-to-digital converter
ADF	annular dark field
BF	bright field
BIB	broad ion beam
BSE	backscattered electron
CBED	convergent beam electron diffraction
DF	dark field
EAM	embedded atom model
EDX	energy dispersive X-ray spectroscopy
EELS	electron energy loss spectroscopy
FFT	fast Fourier transform
FWHM	full width at half maximum
GUI	graphical user interface
HAADF	high-angle annular dark field
HRSTEM	high-resolution scanning transmission electron microscope/microscopy
HRTEM	high-resolution transmission electron microscope/microscopy
IFFT	inverse fast Fourier transform
MC	Monte Carlo
MD	Molecular Dynamics
MH	Metropolis-Hastings
PCA	principal component analysis
PM	photomultiplier
SAED	selected area electron diffraction
SDOM	standard deviation of the (sample) mean
SE	secondary electron
SEM	scanning electron microscope/microscopy
STEM	scanning transmission electron microscope/microscopy
TDS	thermal diffuse scattering
TEM	transmission electron microscope/microscopy
WDX	wavelength dispersive X-ray spectroscopy
ZL	zero loss

Used software

Apart from obligatory software, such as operating system, basic text editors, or browsers, any used applications are listed below.

Application	Version	Weblink
ATOM	1.19.6 ia32	atom.io
CrystalMaker [®] for Windows	9.2.8	www.crystallmaker.com
Gatan Digital Micrograph	2.31.734.0	www.gatan.com
Inkscape	0.92.2	www.inkscape.org
IrfanView	4.38	www.irfanview.com
JabRef	3.8.2	www.jabref.org
jems	4.5230U2017	www.jems-saas.ch
Julia compiler	0.5.0	julialang.org
LAMMPS	26 Jan 2017	lammms.sandia.gov
MATLAB [®]	R2015a (8.5.0.197613)	www.mathworks.com
Paint.NET "Classic"	4.0.17	www.getpaint.net
QSTEM	2.40	www.qstem.org
TeX Live	2016	www.tug.org/texlive
TeXstudio	2.12.6	texstudio.sourceforge.net

1. Introduction and goals

Modern high-resolution electron microscopy is unimaginable without computer-controlled guidance of microscopes and all the possibilities of computer-aided analysis. In addition, computer simulations have found their way into many domains of natural and technical sciences, including electron microscopy. In many cases, the conduct of simulations aims to deduce general laws and to predict the behavior of real systems.

During my last year's work at the Institute of Electron Microscopy and Nanoanalytics¹, numerous simulations of high-resolution scanning transmission electron micrographs were performed. Without access to results from properly corresponding experiments, the explanatory power of these simulation types would have been severely limited. Therefore, the simulated results were compared to experiments at the Austrian Scanning Transmission Electron Microscope (ASTEM), a microscope of the type FEI™ Titan³ G2 60-300.

The gold-nickel system features some interesting phenomena, e.g. there is a region in temperature and chemical composition in which spinodal decomposition of the solid alloy occurs. The consequences of this continuous demixing mechanism, which are periodic concentration modulations in certain crystallographic directions (without the formation of separate phases) and lattice distortions, are visible in conventional TEM and SAED images. Quantitatively, they show the wavelength of the modulations and the magnitude of the distortions, but they are unsuitable in terms of concentration determination. Z-contrast (HAADF-STEM) imaging is more appropriate for this purpose. In addition, if viewed from the perspective of HAADF-STEM, the material contrast is quite good for this alloy because the atomic numbers of Au and Ni are wide apart. This fact should facilitate the quantitative composition determination.

Keeping that in mind, the first goals were to create Au-Ni models of different consti-

¹www.felmi-zfe.at

1. Introduction and goals

tution and to obtain STEM images computed via a multislice algorithm. Next, an *ab initio* concept in order to quantify the contrast in BF- and DF-STEM images had to be excogitated and realized. The most important aim was to learn more about *how* the pictures are generated, e.g. to spot which aspects of Au-Ni specimens and the microscope itself lead to which effects in the actual pictures.

An ambitious long-term vision squired this work. Imagine the following situation, in which an electron microscopist has just recorded some STEM lattice images and monologizes: "Alright, that's a good image. Let me take a look at the intensities. Where is the simulation table? ... Okay, got it, 43 percent iron here and 28 there!"

2. Fundamentals and methods

2.1. The gold-nickel system

This short introduction to the gold-nickel alloy system should make the course of action during this work comprehensible. The occurring phenomenon of spinodal decomposition is the background, which inspired how exactly the high-resolution STEM simulations have been carried out.

The binary alloy system Au-Ni features some interesting properties. On the one hand, gold has an fcc structure at room temperature (298.15 K), an atomic number of 79, and a lattice constant of $(4.079 \pm 0.001) \text{ \AA}$, which has often been (re-)determined in the past, e.g. by Straumanis (1971) and Harada & Ohshima (1981). On the other hand, nickel has an fcc structure as well, but a much lower atomic number of 28, and a significantly shorter lattice parameter of $(3.524 \pm 0.001) \text{ \AA}$, which was measured by In-Kook Suh *et al.* (1988) and many others. Due to the large difference in length of the lattice constants, substitutional foreign atoms of one of the two metals in a matrix of the other lead to extensive distortions of the crystal. This effect will later be demonstrated by dint of TEM images and quantitatively analyzed by MC- and MD-simulations.

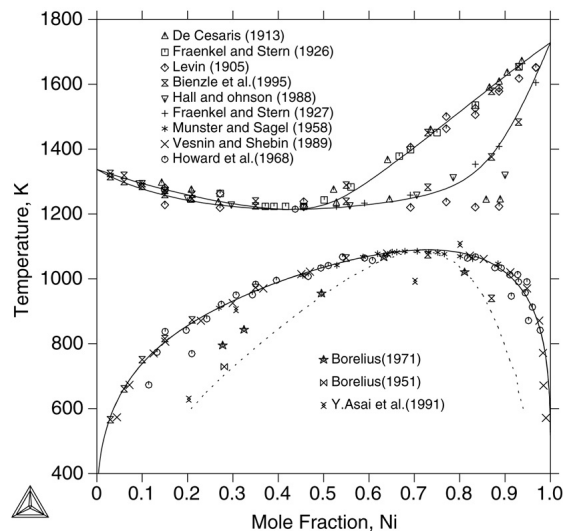


Figure 2.1.: "The Au–Ni phase diagram (solid line) and spinodal line (broken line) calculated from the present thermodynamic description in comparison with experimental measurements ..."; figure and caption from the paper by Wang *et al.* (2005, fig. 1)

A phase diagram of the alloy is shown in figure 2.1. The solid system is completely soluble at temperatures above 1083 K. For lower temperatures, a two-phase field with an asymmetric miscibility gap can be observed, within which decomposition occurs by nucleation. This discontinuous phase separation has been the topic of research over a long period of time (Köster & Dannöhl, 1936; Underwood, 1954; Gust *et al.*, 1976; Hofer, 1982). For temperatures below roughly 600 K, no grains with varying elemental composition appear, but the alloy continuously forms structures with sinusoidal concentration modulations in a coherent crystal lattice (see e.g. figure 2.4). This demixing mechanism was theoretically investigated and named "spinodal decomposition" by Cahn (1961). As explained and described in the materials science book by Gottstein (2014, p. 418-423), it can occur for mixtures with concentrations near the maximum of the $G(c)$ -

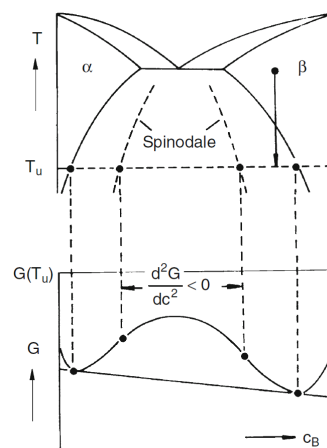


Figure 2.2.: Schematic illustration of the phase diagram (top) and the Gibbs free energy (bottom) of a mixed phase with miscibility gap; figure from the book by Gottstein (2014, p. 422, Abb. 9.10)

curve, where G is the Gibbs free energy and c the concentration of one of the elements. The spinodal decomposition mechanism lowers the Gibbs free energy if the concentration is in the right-curved region of the function (see figure 2.2). This can easily be justified as follows: Chords connecting the concentration points of the decomposed structure indicate its Gibbs free energy and lie below the curve. The inflection points of $G(c)$ for all temperatures shape the chemical spinodal line in the phase diagram. The coherent spinodal line, below which this kind of decomposition actually happens, is shifted to lower temperatures. Specific details about this topic can be found in the book by Predel (1982).

An overview of investigations into the modulated structures of Au-Ni alloys up to that point was given by Hofer & Warbichler (1985). Spinodal decomposition occurs in the $\{100\}$ - and the $\{111\}$ -planes. Fukano (1961) and Moss (1966) found the first experimental evidence, Wu (1978) observed modulations for alloys with Ni-concentrations of 53 and 77 at.%, and Woodilla & Averbach (1968) used electron diffraction to investigate 20 to 60 at.% Ni-alloys. The latter found a critical temperature of 493 K at about 45 at.% and concentration modulation wavelengths from 6.5 Å (54 at.% Ni) to 13 Å (22 at.% Ni) in the $\langle 100 \rangle$ -directions, which were determined by measuring the distances between fundamental reflections and their satellites, which

stem from the concentration modulations, in diffraction patterns like shown in figure 2.4.

The spinodal decomposition mechanism was verified for higher temperatures and higher Ni-concentrations by Fukano (1961). Later, Hofer (1982) and Hofer & Warbichler (1984, 1985) studied the region of spinodal decomposition extensively again and summarized the results of their own and previous works regarding the accurate course of the spinode in the phase diagram (see figure 2.3). As for electron diffraction, besides the satellites at the fundamental reflections (200), (020), (220), ..., Hofer (1982) recognized {110}- and {310}-reflections (see figure 2.4), which are, as ascertained later, piercing points caused by atomic defects.

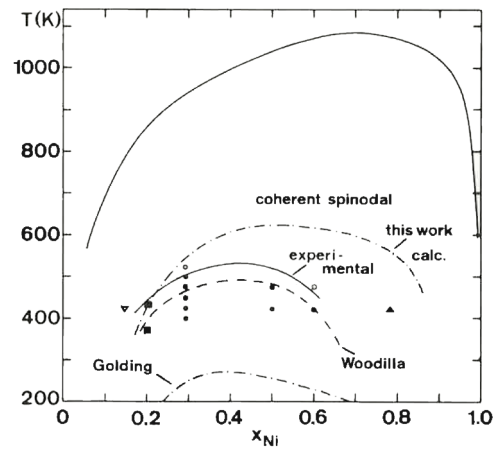


Fig. 5. Phase diagram of solid Au-Ni alloys with chemical and coherent spinodal and the region of spinodal decomposition.
 ● modulated structures observed this work
 ○ no modulations
 ■ spinodal decomposition observed by Fukano⁶⁾
 ▲ modulations observed by Sinclair et al.²⁾
 ▽ no modulations by Wu⁵⁾.

Figure 2.3.: "Phase diagram of solid Au-Ni alloys ..."; figure from the paper by Hofer & Warbichler (1985, fig. 5)

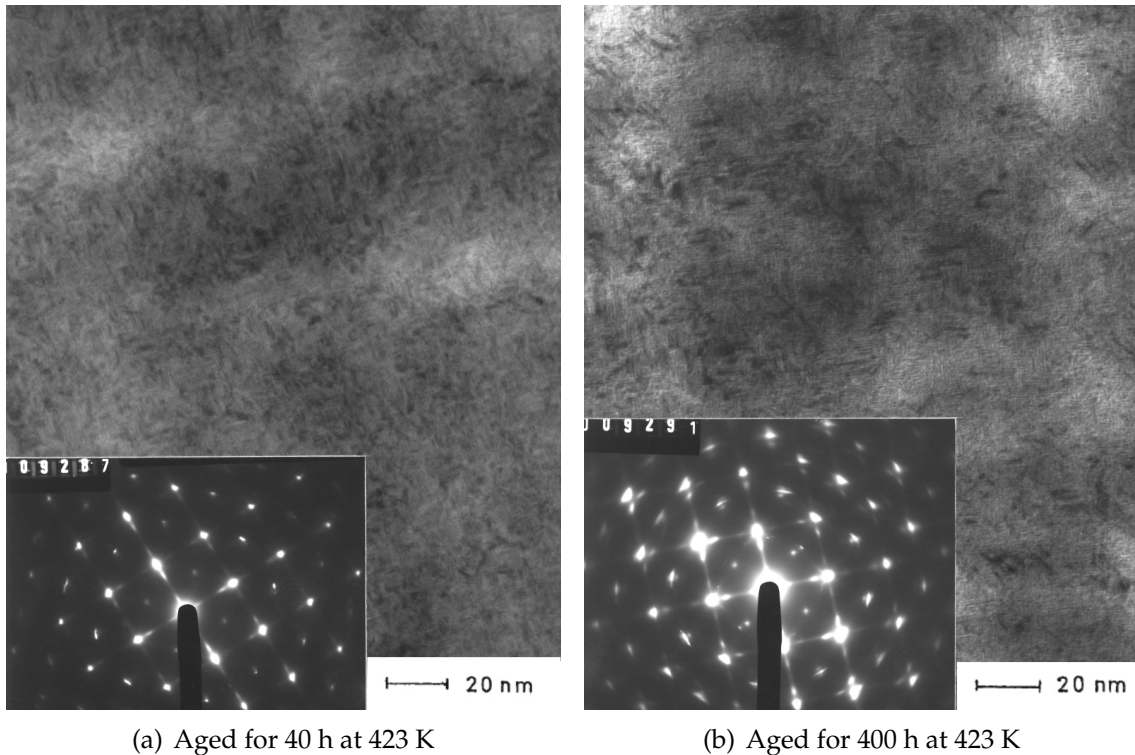


Figure 2.4.: Transmission electron micrographs and electron diffraction images of a Au-Ni specimen with $c_{Ni} = 0.291$ for different annealing durations, [001] zone axis; from the PhD thesis by Hofer (1982, p. 131ff, Abb. 42 & 44)

2.2. STEM

The following section is a brief summary of STEM aspects relevant to this thesis. It covers electron detector types and their setup for STEM imaging as well as basics regarding the STEM contrast formation. Essentially, its content is an excerpt from the book about (S)TEM by Williams & Carter (1998, ch. 7.3, 9.4, 22) and should help readers who are little familiar with STEM to get along in the results section. Additionally, some details about the practical work are given (used collection angles, concept of contrast).

Unlike to TEM imaging, STEM images are not generated once at a time. The beam is a fine probe with a diameter in the range of 1 Å for modern HRSTEMs, which is scanned across a section of the specimen. For every scan position, the transmitted electron signal is measured and a pixel is generated. Note that, in contrast to SEMs, where the beam pivots around a point before/above the specimen, the scanning beam of STEMs² has to be parallel to the optic axis at all times and positions.

2.2.1. Electron detectors

Functionality

In STEMs, two kinds of electron detectors other than the fluorescent screen play a major role: Semiconductor detectors and scintillator-photomultiplier systems. The first is realized by creating a p-n junction in a semiconducting material. Electrons with sufficient kinetic energy that hit the p-n junction excite valence-band electrons across the band gap and put them into the conduction band. The number of electron-hole pairs created per incoming electron depends on the kinetic energy. In order to measure the electron count, an external bias in reverse direction is applied and the electric current is measured. In (S)TEM practice, if a beam of high-energy electrons hits the detectors, enough electron-hole pairs are created such that the internal bias of the p-n junction is sufficiently high to separate the electrons and holes and no external bias is needed. Due to the large capacitance of semiconductor detectors they are not responsive to fast changes in the intensity of the electron signal. Their bandwidth is in the range of 100 kHz.

Scintillator-photomultiplier detectors, on the other hand, can be made of materials

²more precisely: the axis of the convergent beam cone

for which the emission of light rapidly decays after being struck by electrons, such as Ce-doped yttrium-aluminum garnet (YAG). Thus they have a broad bandwidth in the MHz-range. Additionally, their noise level is low compared to semiconductor devices. Although scintillator-PM detectors exhibit some disadvantages as well, such as higher susceptibility to radiation damage, higher costs and lower energy-conversion efficiency, they are preferred over the semiconductor detector for general electron detection.

Types of imaging

In the following, I completely skip SE/BSE imaging (more important in the domain of SEM), diffraction images, and EELS/EDX/WDX mapping, and just mention some details about bright field and dark field imaging.

Figure 2.5 is a sketch of how the STEM detection system looks like. The objective lens focuses the incident electron beam, which hits the specimen under a certain angle range with respect to the optical axis. Its upper boundary is called the convergence (semi-)angle and usually abbreviated by α . Knowing that not all transmitted electrons will travel in the same direction, one can position detectors at different locations in order to obtain diversified information about specimens. In general, the corresponding detector regions are well-defined by a solid angle range with respect to the optical axis. Since usually circular or annular axis-on-axis³ detectors are used, the angle enclosed by the trajectory of a transmitted electron and the optical axis of the microscope becomes the identifying parameter. Henceforth, it is called collection (semi-)angle or semi-angle of collection and subsequently abbreviated by β . For a specific detector in an experiment, the

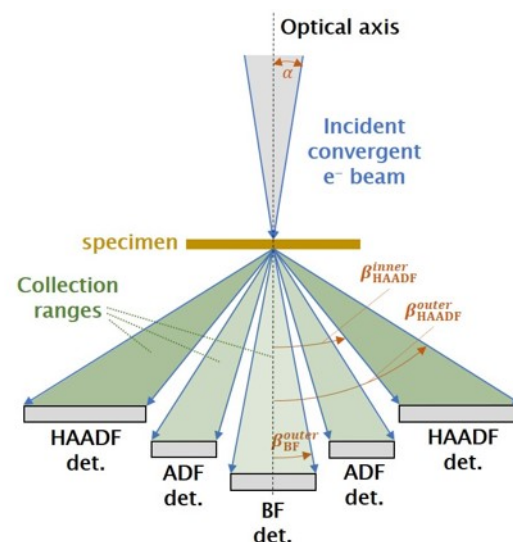


Figure 2.5.: Schematic of the detector setup for STEM imaging; The detectors have to be imagined circular/annular. The sketch is neither length-preserving nor conformal to angles.

³coincident detector and microscope axis

2. Fundamentals and methods

Table 2.1.: Juxtaposition of collection semi-angle ranges for FEI Titan³ G2 60-300 (β_{exp}) and QSTEM simulations (β_{sim}); Values for Titan from the PhD thesis by Knez (2017, p. 22f)

detector	$\beta_{\text{exp}} / \text{mrad}$	$\beta_{\text{sim}} / \text{mrad}$
BF	[not measured]	0 .. 40
ABF	[not measured]	$\frac{\alpha}{2} .. \alpha$
ADF	12.5 .. 28*	[not used]
HAADF	62.2 .. 214*	73.5 .. 200

* valid for a nominal camera length of 91 mm

range of β can be changed by varying the camera length⁴. We classify STEM electron detectors into the following types, whereat the denoted collection angle boundaries should not be considered strict but as approximate reference values:

Bright field (BF)

A BF detector is circular, intercepts the direct beam and collects unscattered and forward-scattered electrons, typically with $\beta \approx 0 .. 40$ mrad.

Annular bright field (ABF)

This detector is also disc-shaped, but has a circular hole in its center. The defining criterion is $\beta_{\text{outer}} \stackrel{!}{=} 2\beta_{\text{inner}}$ and the usual range of an ABF detector is $\beta \approx 10 .. 20$ mrad.

Annular dark field (ADF)

In principle, in order to perform DF STEM imaging one can shift the stationary diffraction pattern in such a way that a specific beam of scattered electrons hits the BF detector. Though, usually there is a dedicated axis-on-axis detector for this purpose, namely the ADF, which collects electrons scattered to higher angles with respect to the optical axis. The typical β -range is 50 .. 100 mrad.

High-angle annular dark field (HAADF)

We can use another detector that sits around the ADF and collects electrons scattered out to even higher angles, $\beta \approx 100 .. 200$ mrad for instance. So-called high-angle annular dark field images are obtained this way. HAADF-STEM images most notably feature highly sensitive contrast regarding the mean atomic number (Z-contrast, see section 2.2.2), which makes this kind of detector particularly interesting. The focus of this thesis clearly lies on HAADF imaging and Z-contrast between gold-rich and nickel-rich regions.

Table 2.1 gives an overview of the used collection semi-angle ranges, both experimentally and in simulations.

⁴effective distance between specimen and screen/detector

2.2.2. Image contrast

A widely-used definition is the Weber contrast

$$C_W(I_1, I_2) := \frac{(I_2 - I_1)}{I_1} = \frac{\Delta I}{I_1} = \frac{I_2}{I_1} - 1. \quad (2.1)$$

As a rule of thumb we can state that $|C_W| < 5\%$ cannot be detected by the human eye. There is an inconsistency coming along with this definition of contrast, because $C_W = +x$ does not correspond to the same relative change in intensity as $C_W = -x$. This is why I plotted values of $\frac{I_2}{I_1}$ in semi-logarithmic representation or the quantity

$$C_{\ln}(I_1, I_2) := \ln\left(\frac{I_2}{I_1}\right) \quad (2.2)$$

in linearly scaled graphs in the present work. Since equal values of the modulus of C_{\ln} correspond to the same effective contrast, e.g. $|C_{\ln}(I, 2I)| = |C_{\ln}(I, \frac{1}{2}I)|$, the variable C_{\ln} is in accordance with the perceived brightness in the Weber-Fechner law, which was formulated by Fechner (1860, ch. XXIII, p. 89ff). The human detection limit for contrast expressed in terms of C_{\ln} is again roughly $\pm 5\%$.⁵

Mass-thickness and Z-contrast

Variations of the specimen properties mass density, (mean) atomic number, and thickness affect the beam-specimen interaction.⁶ In general, heavier elements and thicker specimen regions appear darker in BF-STEM images, but brighter in DF-STEM images. Z-contrast represents the atomic limit of mass contrast where detectable scattering stems from single atoms or atom columns (Williams & Carter, 1998).

HAADF-STEM images exhibit exceptionally strong Z-contrast. The contrast in the micrographs mainly arises from incoherent elastic scattering and quasi-elastic phonon scattering (TDS). The actual Z-dependency of the HAADF signal varies significantly from case to case. The TDS contribution increases with Z, approximately as $Z^{1.5}$ (Williams & Carter, 1998). For single incoherent elastic scattering events and at the limit of high angles, one would obtain a quadratic dependency of intensity on

⁵For low values $C_W(x, y) \leq 1$, we have $C_{\ln}(x, y) \approx C_W$, because the first-order approximation of $\ln(x)$ is $x - 1$ (Taylor series at $x_0 = 1$).

⁶Of course, there are many other properties which have an effect on the interaction as well.

the atomic number in accordance with the cross section for Rutherford scattering⁷ (Nellist & Pennycook, 2000), which holds true for Mott as well as for Dirac scattering. Assume I_Z abbreviates the intensity after the effects of all parameters other than the atomic number (e.g. noise, thickness background, ...) have been eliminated. The exponent γ in $I_Z \propto Z^\gamma$ becomes lower than 2 due to screening effects and multiple scattering events (dynamic scattering) in combination with electron channeling. The latter plays a major role if the probe beam is oriented in a zone axis of a crystal. Thus, values given in literature are not uniform and they do not cover every case. Kirkland (2010, p. 107) found $\approx Z^{1.5}$ to $Z^{1.7}$ for ADF-STEM simulations of very thin specimens (only a few atoms thick). For two atom species in the same column parallel to the incident beam, we have to distinguish between two different assumptions. If we acted on the assumption that scattering from two atoms can be added coherently, we would expect $I_Z^c \propto (Z_A + Z_B)^{\gamma_c}$. This leads to $I_Z^c \propto (c_A Z_A + c_B Z_B)^{\gamma_c} = \bar{Z}^{\gamma_c}$ for an atom column with the elemental concentrations c_A and c_B , where \bar{Z} is the mean atomic number (Brydson, 2011, p. 90ff). But, since we assume mostly incoherent scattering, we expect

$$I_Z^i \propto c_A Z_A^{\gamma_i} + c_B Z_B^{\gamma_i} = \overline{Z^{\gamma_i}},$$

which can be rewritten to

$$I_Z^i \propto Z_B^{\gamma_i} + [\bar{Z} - Z_B] \frac{Z_A^{\gamma_i} - Z_B^{\gamma_i}}{Z_A - Z_B} = f_1(\gamma_i, Z_A, Z_B) + f_2(\gamma_i, Z_A, Z_B) \bar{Z}. \quad (2.3)$$

The intensity I_Z^i actually is a linear function of \bar{Z} . If either c_A or c_B becomes zero, I_Z^i gets equal to I_Z^c .

As for the thickness dependence of HAADF intensities, Carter *et al.* (2016, ch. 11.1, p. 284ff) stated that the first-order prediction for perfect incoherence along a column of atoms would be a linear behavior of the scattered intensity as a function of thickness, because scattering cross sections of individual atoms could just be added up. There are several reasons leading to a non-linear behavior. Excited phonons have a finite coherence length of a few atomic spacings in the direction of the beam. Based solely on this effect, the initial thickness dependence would go as t^2 . For thicker specimens, after a few atom monolayers, channeling and beam broadening get important. These effects result in a strong contribution from the atoms in the first channeling peak, independent of thickness, and a background that is higher, the thicker the crystal is.

⁷charged particles without spin

Furthermore, the finite probe current limits the rise of the detected intensity⁸ (Nellist & Pennycook, 2000).

Diffraction contrast

If the sample is crystalline, electrons can get coherently elastically scattered by Bragg diffraction. Depending on whether Bragg's condition is fulfilled or not and whether BF or DF imaging is concerned, grains with different orientations appear darker or brighter. In addition, bendings within a grain lead to diffraction contrast as well. Note that diffraction contrast is negligibly weak in DF-STEM imaging when compared to mass-thickness and Z-contrast, but can be the predominant reason for contrast in BF-STEM images (Williams & Carter, 1998).

2.3. HRSTEM image simulation

Currently, there are two widespread approaches when it comes down to the simulation of HR(S)TEM images of thick specimens (more than a few atoms thick): The Bloch wave eigenvalue solutions and multislice algorithms. QSTEM uses the latter method, which is briefly discussed here.

2.3.1. The multislice method

The specimen is sectioned into slices split by plains perpendicular to the incident beam. The incoming electron wave function is modified by the specimen slice and transferred to the next slice. There exist different calculation methods for the transfer, however, all of them have one thing in common: The wave function $\psi_{n+1}(x)$ after the $(n + 1)$ -th slice can be determined from $\psi_n(x)$ and does not depend on any other slice before the n -th. A detailed description of the multislice method can be found in the book by Kirkland (2010).

TDS effects can also be included into multislice simulations. This is, for instance, achieved by so-called frozen phonon multislice methods, which QSTEM offers an option for. Multiple calculations for different thermal displacements of the atoms,

⁸(!) conservation of energy

"frozen" configurations, are performed and averaged over. This approach is reasonable because lattice vibrations happen on a much larger time scale (typical period of 10^{-13} s) than the transmission of (S)TEM electrons through specimens (about $3 \cdot 10^{-17}$ s for a 100-keV-electron and a 10-nm-specimen). (Hawkes & Spence, 2008, p. 93f)

2.3.2. Simulation software package Q(uantitative)STEM

This software package (Koch, 2016) has been developed by Prof. C. T. Koch (HU Berlin) during the work on his PhD thesis (Koch, 2002). It offers the simulation of TEM, STEM and coherent CBED images. The user has to create a specimen model in advance, which QSTEM can replicate in space. Scanning window size and sample tilt are flexible. A lot of microscope parameters are adjustable: Acceleration voltage, defocus, astigmatism, spherical and chromatic aberration coefficients, higher order aberrations, temperature, energy spread of the beam, convergence angle, beam tilt, dwell time, gun brightness...

As for detectors, an arbitrary number (limited by the capacities of the computing system, of course) can be set. A specific collection angle range can be assigned to each of them. Hence, in order to simulate HAADF images for a large collection angle width, e. g. $\beta = 100 \dots 150$ mrad, it is practicable to insert many detectors each with some fraction of the total range, e. g. one for $\beta = 100 \dots 110$ mrad, one for $\beta = 110 \dots 120$ mrad, and so on. In the post-processing, one can arbitrarily sum over specific detectors that were split before. This approach leads to a significant gain in information.

A brief introduction to the usage of QSTEM is given in the appendix B.

2.4. Quantitative HRSTEM image analysis

Quite a lot of research dealing with quantitative composition determination from HAADF-STEM at atomic resolution has been going on within the last two decades (e.g. Anderson *et al.* (1997); LeBeau *et al.* (2008); Martinez *et al.* (2014)). A prerequisite for that purpose is the reversibility of the imaging process, which includes all steps between when electrons hit the detector and when the final image is produced. After the electrons reach the detector, the time-averaged electron flux is converted to

a detector signal (photon flux or current depending on the detector type), which is then processed by electronic units and transferred to an analog-to-digital converter (ADC). Linearity of this process is desirable in order enable us to quite easily back-calculate. This, however, cannot always be ensured, e.g. if the detector signal and or the ADC output become under- or oversaturated (LeBeau & Stemmer, 2008).

In the following, the signal manipulation between detector and ADC is described, because the elimination of its effect on intensity ratios is mandatory for meaningful quantitative analysis of experimental image data. Later, the functionalities of the MATLAB code emerged from the wish to automatedly analyze HR(S)TEM micrographs are sketched.

Signal-processing electronics: Settings ‘Contrast’ and ‘Brightness’

(S)TEM control panels usually feature turning knobs for the settings ‘Contrast’ and ‘Brightness’. The microscopes used for this work were both manufactured by the same company and, according to the device manuals, these two settings affect the detector signal in the following manner: Because the original intensity is too low to be detected by the analog-to-digital (ADC) converter, an amplification between detector and ADC is necessary. Its amount is varied via the ‘Contrast’ setting. Because the amplified signal has to remain within the allowed boundaries of the ADC, an offset has to be applied as well. This is controlled by the ‘Brightness’ setting. The user cannot change or revert these modifications once a micrograph has been taken, because they happen before the conversion from a current to a digital value. Figure 2.6 is a sketch of the described situation.

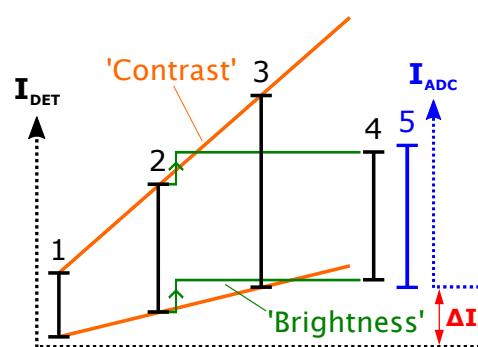


Figure 2.6.: Illustration of the effects of the signal-processing parameters ‘Contrast’ and ‘Brightness’; 1 is the original signal range, 2 and 3 are signal ranges amplified by ‘Contrast’, 4 is the the signal range 2 offset by ‘Brightness’, and 5 is the allowed ADC input range. The two intensity scales indicate the zero-point shift between detector and ADC. A drawing in the user’s manual for FEI Titan³ G2 60-300 (section "Detector control") served as a template for this figure.

A secondary goal of this thesis was to verify or falsify whether the signal modifica-

tion obeys the linear law

$$I_{\text{ADC}}(C, B) = I_{\text{DET}} \cdot k_C \cdot C + k_B \cdot B - \Delta I_0, \quad (2.4)$$

where I_{ADC} is the intensity value corresponding to the current flowing through the analog side of the ADC, I_{DET} is the detector output intensity, C and B are the numerical values for the settings 'Contrast' and 'Brightness', k_C and k_B are proportionality constants, and ΔI_0 is the zero-point shift between detector and ADC.

In general, both settings change intensity ratios and thereby contrast according to the definitions in equations (2.1) and (2.2), which is why the terms are put between single quotation marks. If equation (2.4) holds true, we can get rid of the 'Brightness' and the (unknown) zero-point shift for the most part, simply by subtracting the mean vacuum level⁹ after leaving 'Contrast' and 'Brightness' unchanged. We obtain

$$I_{\text{ADC}}^*(C) = I_{\text{ADC}}(C, B) - I_{\text{ADC,vac}}(C, B) = (I_{\text{DET}} - I_{\text{DET,vac}}) \cdot k_C \cdot C, \quad (2.5)$$

in which C , directly correlated with the setting 'Contrast', does actually not affect contrast as defined above.

Peak detection and quantification for experimental ADF/HAADF micrographs

We had visions of a dedicated application able to accomplish the following: Read grey scale image files, subtract the vacuum level, apply a noise filter, search for peaks or valleys - probably corresponding to atom columns in HR(S)TEM images - in the grey scale matrix, calculate an objective and normalized value for every found peak, and display the results in a way such that the viewer is capable of capturing the essential in the twinkling of an eye.

I am very grateful that Dr. Daniel Knez generated a nicely working solution including a graphical user interface for most of all tasks mentioned above. His application, which I could supplement with a few subtleties, works for files in the formats TIF, DM3, DM4, and IMG¹⁰. One can opt for a patch-based principal component analysis (Patch-PCA), introduced by Pearson (1901), or a mean filter. In most cases, maxima are reliably found for user-defined 'minimum intensity' (threshold) and 'minimum

⁹mean grey scale value in an image of vacuum

¹⁰QSTEM output

distance'. The segmented image can be displayed in a diagram type defined by Voronoi (1908). Finally, for every maximum, the grey scale values within an adjustable pixel radius are summed. The resulting peak intensity distribution is visualized in a histogram. One might claim that a 2D Gaussian fit would be more appropriate - and indeed, it is. We tried to implement that, but it took us too long to make it working properly (automate starting parameters, catch various exceptions, find the best iteration method, convergence criteria, ...), so at some point we just stopped because we did not feel the time investment may be worth it for our purpose. In order not to swell this paragraph, demonstrating illustrations are consciously omitted here. Once the reader moves on to the experimental results section 3.2.1, and figure 3.44 respectively, potential obscurities will hopefully become superfluous.

Simulated image series

As mentioned at the beginning of this thesis, a main objective was to identify the effects of a few microscope and specimen parameters on detected electron intensities. While varying each parameter one at a time, performing basically the same simulation again and again produces a lot of data. Rapidly I realized that, at the end of my simulation work, there would be about ten to twenty thousand simulated images to be analyzed. It is self-explanatory this cannot be done manually in a reasonable amount of time. Although the application described in the previous paragraph can, in principle, be used for simulated images as well, the computing time is way too long either.

Therefore, it was crucial to write another relatively extensive MATLAB code capable of quickly reading and analyzing multislice image series. Fortunately, a noise filter is obsolete and the crystal model inputs can be standardized in such a way as to get all the peaks at well-defined positions throughout a series, making the dynamic peak search unnecessary. All images were source size corrected with a probe diameter of 70 pm (FWHM), which is equal to the probe size of the experimentally used HRSTEM Titan. As for the peak intensity determination, the values within a tunable pixel radius were summed, just as we did it in the code for experimental images. Finally, all intensities corresponding to the same domain, e.g. pure gold atom columns, were averaged, resulting in a normalized numerical value, e.g. I_{Au} .

The plots include graphs of absolute as well as relative electron intensities (used definition of contrast see equation (2.2)) stemming from gold/nickel/mixed atom

columns against thickness, collection semi-angle, mean atomic number, or nickel concentration for different convergence angles and Au-Ni alloy models.

2.5. Simulated lattice relaxation of binary alloys

After a few weeks of STEM image simulation activity, in order to get closer to reality we started to work on and with simulation software suitable to carry out lattice relaxations of the created virtual Au-Ni alloy models. The original models, despite possessing structures originating from spinodal decomposition, still had a perfect fcc lattice with a parameter of $a = 4.07894 \text{ \AA}$, so the interatomic distances were $a\sqrt{2}/2$ between nearest neighbors and a between second-nearest neighbors. We dealt with up to 13500 atoms in total and utilized an embedded atom model (EAM) potential in a Monte Carlo (MC) algorithm and a Molecular Dynamics (MD) integration at constant temperature. In addition, a Finnis and Sinclair potential has been implemented into the MC code.

2.5.1. Potentials

Finnis and Sinclair form, 'RTS'

Sutton & Chen (1990) published fcc metal potential parameters (see table 2.2) for the following form according to Finnis & Sinclair (1984):

$$E = \epsilon \left[\frac{1}{2} \sum_i \sum_{j \neq i} V(r_{ij}) - c \sum_i \rho_i^{\frac{1}{2}} \right], \quad (2.6)$$

in which

$$V(r_{ij}) = \left(\frac{a}{r_{ij}} \right)^n \quad (2.7)$$

and

$$\rho_i = \sum_{j \neq i} \left(\frac{a}{r_{ij}} \right)^m. \quad (2.8)$$

$V(r_{ij})$ is a repulsive pair potential term corresponding to the Coulomb interaction of two atoms, ρ_i is the electron density at the site of atom i arising from all other atoms, r_{ij} is the distance between atoms at the sites i and j , and a is the lattice constant. ϵ is

Table 2.2.: Finnis and Sinclair potential: Fcc metal parameters computed for a cut-off radius of 2 lattice constants; Values from the paper by Rafii-Tabar & Sutton (1991, p. 221)

	ϵ / eV	c	m	n
Ni	1.5713e-2	39.755	6	9
Cu	1.2386e-2	39.755	6	9
Rh	4.9371e-3	145.658	6	12
Pd	4.1790e-3	108.526	7	12
Ag	2.5415e-3	145.658	6	12
Ir	2.4489e-3	337.831	6	14
Pt	1.9835e-2	34.428	8	10
Au	1.2794e-2	34.428	8	10
Pb	5.5772e-3	45.882	7	10
Al	3.3307e-2	16.460	6	7

a parameter with the dimension of energy, c a dimensionless parameter, and n and m are positive integer values.

Rafii-Tabar & Sutton (1991) later expanded the model to be suitable for binary fcc metallic alloys. In the generalized form, the potential energy can be expressed as follows:

$$E = \frac{1}{2} \sum_i \sum_{j \neq i} \epsilon_{ij} \left(\frac{a_{ij}}{r_{ij}} \right)^{n_{ij}} - \sum_i \epsilon_i c_i \left[\sum_{j \neq i} \left(\frac{a_{ij}}{r_{ij}} \right)^{m_{ij}} \right]^{1/2} \quad (2.9)$$

Here, one has to respect that

$$\epsilon_{ij} = \begin{cases} \epsilon^{AA} & \text{if sites } i \text{ and } j \text{ are both occupied by an A atom} \\ \epsilon^{BB} & \text{if sites } i \text{ and } j \text{ are both occupied by a B atom} \\ \epsilon^{AB} & \text{if sites } i \text{ and } j \text{ are occupied by different elements.} \end{cases} \quad (2.10)$$

ϵ^{AA} and ϵ^{BB} name the parameter ϵ of the pure metals A and B, whereas a determination rule for ϵ^{AB} has to be defined. The same applies to the parameters a , c (exception: c^{AB} does not occur), m , and n . Rafii-Tabar and Sutton assumed the Lorentz-Berthelot mixing rules

$$\epsilon^{AB} = \sqrt{\epsilon^{AA}\epsilon^{BB}}, \quad a^{AB} = \sqrt{a^{AA}a^{BB}}, \quad (2.11)$$

$$m^{AB} = \frac{1}{2} (m^{AA} + m^{BB}), \quad n^{AB} = \frac{1}{2} (n^{AA} + n^{BB}). \quad (2.12)$$

Henceforth, this potential is called 'RTS'.

2. Fundamentals and methods

Table 2.3.: EAM potential: Parameters for gold and nickel; Values from the paper by Zhou *et al.* (2004, TABLE III)

	Au	Ni
$r_e / \text{\AA}$	2.885034	2.488746
f_e	1.529021	2.007018
σ_e	19.991632	27.562015
σ_s	19.991509	27.930410
α	9.516052	8.383453
β	5.075228	4.471175
\tilde{A} / eV	0.229762	0.429046
\tilde{B} / eV	0.356666	0.633531
κ	0.356570	0.443599
λ	0.748798	0.820658
G_{n0} / eV	-2.937772	-2.693513
G_{n1} / eV	-0.500288	-0.076445
G_{n2} / eV	1.601954	0.241442
G_{n3} / eV	-0.835530	-2.375626
G_0 / eV	-2.980000	-2.700000
G_1 / eV	0	0
G_2 / eV	1.706587	0.265390
G_3 / eV	-1.134778	-0.152856
η	1.021095	0.469000
G_e / eV	-2.978815	-2.699486

Embedded atom model, ‘Zhou’

Johnson (1989) and Wadley *et al.* (2001) derived an EAM potential for binary alloys with a form as follows:

$$E = \frac{1}{2} \sum_i \sum_{j \neq i} \phi_{ij}(r_{ij}) + \sum_i F_i(\rho_i), \quad (2.13)$$

at which

$$\phi(r) = \frac{\tilde{A} \exp \left[(-\alpha (\frac{r}{r_e} - 1)) \right]}{1 + (\frac{r}{r_e} - \kappa)^{20}} - \frac{\tilde{B} \exp \left[(-\beta (\frac{r}{r_e} - 1)) \right]}{1 + (\frac{r}{r_e} - \lambda)^{20}} \quad (2.14)$$

and

$$\rho_i = \sum_{j \neq i} f_j(r_{ij}) \quad (2.15)$$

with

$$f(r) = \frac{f_e \exp \left[-\beta \left(\frac{r}{r_e} - 1 \right) \right]}{1 + \left(\frac{r}{r_e} - \lambda \right)^{20}}. \quad (2.16)$$

$\phi_{ij}(r_{ij})$ is the pair energy between atoms at the sites i and j separated by a distance r_{ij} and $F_i(\rho_i)$ is the so-called embedding function that corresponds to the embedment of an atom i into a site with a local electron density ρ_i arising from all other atoms. r_e is the spacing between nearest neighbors in equilibrium ($r_e = a\sqrt{2}/2$ for fcc). \tilde{A} , \tilde{B} , α and β are the model parameters, supplemented by the cut-off parameters κ and λ . As for the embedding function, the equations are

$$F(\rho) = \begin{cases} \sum_{i=0}^3 G_{ni} \left(\frac{\rho}{0.85\sigma_e} - 1 \right)^i & \rho < 0.85\sigma_e \\ \sum_{i=0}^3 G_i \left(\frac{\rho}{0.85\sigma_e} - 1 \right)^i & 0.85\sigma_e \leq \rho < 1.15\sigma_e \\ G_e \left[1 - \left[\ln \left(\frac{\rho}{\sigma_s} \right) \right]^\eta \right] \left(\frac{\rho}{\sigma_s} \right)^\eta & 1.15\sigma_e \leq \rho \end{cases} \quad (2.17)$$

with the parameters G_{ni} and G_i for $i = 0..3$, G_e , σ_e , σ_s and η . Note that the RTS-potential can also be transformed into an EAM form with the definitions $F_i := -\epsilon_i c_i \sqrt{\rho_i}$ and $\phi_{ij} := \epsilon_{ij} V_{ij}$.

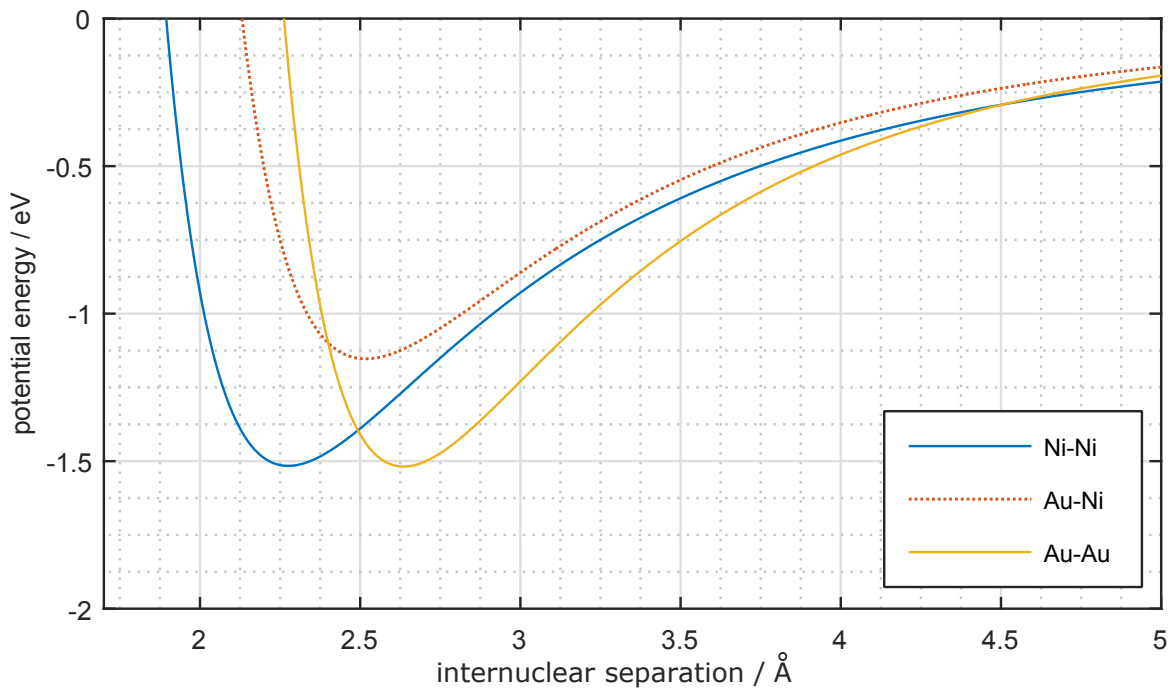
The alloy model shows an adaption for ϕ . The pair potential for different elements A and B is

$$\phi^{AB} = \frac{1}{2} \left[\frac{f^b(r)}{f^a(r)} \phi^{AA} + \frac{f^a(r)}{f^b(r)} \phi^{BB} \right]. \quad (2.18)$$

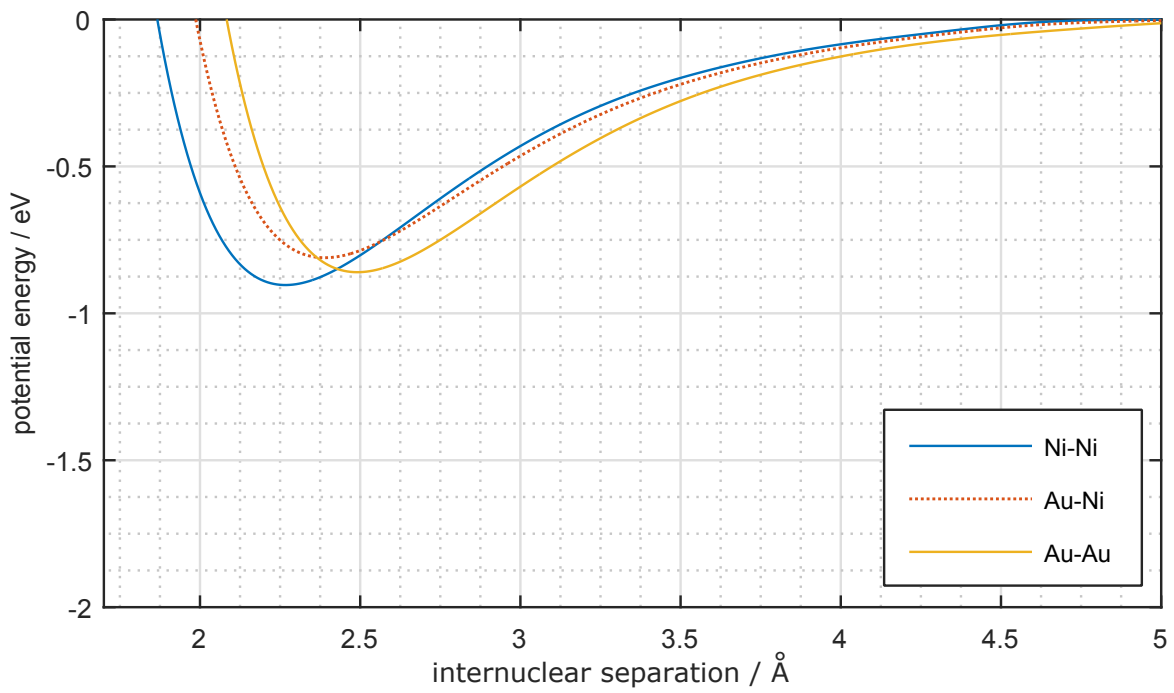
The assignment to ϕ_{ij} is the same as for the RTS-parameters according to equation (2.10). Table 2.3 contains all needed parameters for gold and nickel, which were calculated by Zhou *et al.* (2001). Henceforth, this potential is called ‘Zhou’.

The shapes of the discussed potentials for two atoms are drawn in figure 2.7. We put on record that the RTS-potential is steeper near its minimum in all cases. This will be reflected in a higher atom mobility during the MC-simulation. It is also very interesting that the RTS-potential minimum lies about 50 % lower than the minimum of the Zhou-potential. Anyway, for models with a larger number of atoms, say $N \geq 1000$, we will find that the relative difference in total energy is within ± 3 %. This apparent inconsistency is justified by the insight that the Zhou-parametrization of the embedding energy is not suited for models which are too small.

2. Fundamentals and methods



(a) RTS-potential



(b) Zhou-potential

Figure 2.7.: Two-atom energies of the pairs Au-Au, Au-Ni, and Ni-Ni vs. interatomic separation for the RTS- and the Zhou-potential

Periodic boundary conditions (p.b.c.)

Simulating crystal models small compared to real bulk specimens¹¹ requires the implementation of p.b.c. in order to get rid of or at least reduce surface effects. In this frame, p.b.c. mean that the model can be periodically repeated, with the effect that an atom located at one side of the surface becomes a neighbor of an atom at the opposite side. One needs to calculate (evidently distance-dependent) potential energies, which implies the introduction of a box size. An MC step can then propose a single atom displacement or a box size change. In the second case, the random walk is performed in the space of logarithmic volume instead of length, as suggested by Frenkel & Smit (2002, p. 122).

2.5.2. Metropolis-Hastings algorithm (Monte Carlo)

This well-known Monte Carlo sampling method was introduced by Metropolis *et al.* (1953) and later generalized by Hastings (1970). A detailed explanation of the algorithm and its broad scope of application can be found in numerous works about computational physics, such as the book by Binder & Heermann (1988). Respecting importance sampling, it creates an ergodic Markov chain¹² of states x according to the Boltzmann distribution

$$\pi(x) = \frac{1}{Z} \exp(-\beta E(x)), \quad \beta := k_B T, \quad (2.19)$$

with the probability density $\pi(x)$, the energy $E(x)$, the Boltzmann constant k_B , the temperature T , and the normalization constant $Z = \int \exp(-\beta E(x)) dx$.

The self-composed code was written in the high-level programming language Julia, which was invented by Bezanson *et al.* (2012), and is compatible to version 0.5.0. Some important ideas for the practical implementation originate from the course "Computer simulations" at TU Graz. Further concepts were adapted from the book by Frenkel & Smit (2002, ch. 5). Individual code fragments were adopted from the PhD thesis by Knez (2017), values of physical constants were downloaded from the National Institute of Standards and Technology (2017, [online]).

¹¹In the scope of this work, models in the range of up to $60 \times 60 \times 60 \text{ \AA}^3$ (cube of $15 \times 15 \times 15 = 3375$ Au unit cells, 13500 atoms for fcc) were simulated.

¹²In this context, a Markov chain is a sequence of generated states in which a subsequent state only depends on a limited number of previous states, not on all before. In the case of Metropolis-Hastings, any state solely depends on its predecessor.

The proposal probability from state x to y is the same as vice versa, which leads to the acceptance probability

$$p_{x \rightarrow y}^{\text{acc}} = \min\left(1, \frac{\pi_y}{\pi_x}\right) = \min\left(1, e^{-\beta \Delta E}\right), \quad \Delta E := E(y) - E(x). \quad (2.20)$$

Furthermore, due to the high number of atoms ($N = 13500$) the simulation program needed to deal with, we were forced to make a trade-off. If we had calculated the total energies according to equations (2.9) and (2.13) from section 2.5.1 for every MC step and used only one CPU, just thermalizing the system would have taken several months on a state-of-the-art personal computer.

Clearly, because this thesis is not about efficiently parallelizing tasks on computer systems, we truncated the calculation of ΔE . To clarify, let the random number generator roll k and the MH algorithm propose to displace the k -th atom. For equation (2.9) (RTS-potential), the sum over i is left out and we define the "single-atom energy"

$$E_k(x) := \sum_{j \neq k} \epsilon_{kj} \left(\frac{a_{kj}}{r_{kj}(x)} \right)^{n_{kj}} - \epsilon_k c_k \left[\sum_{j \neq k} \left(\frac{a_{kj}}{r_{kj}(x)} \right)^{m_{kj}} \right]^{1/2}. \quad (2.21)$$

The difference

$$\Delta E_k := E_k(y) - E_k(x) \quad (2.22)$$

is not the same as ΔE , because the terms for any i in equation (2.9) are changed if atom k is displaced, not only the summand with $i = k$. As for the difference $\Delta E_k - \Delta E$, we do not commit a systematic error for the pair potentials, as all contributions not taken into account in the first sum in equation (2.21), namely for any pair of i and j with $i \neq k$ and $j \neq k$, remain unaffected. In contrast to this, the truncation does change the embedding energy difference. In other words: Moving atom k does not only affect the pair energies and the embedding energy of k itself, but also changes the electron density at any other site and, with it, the embedding energy of any atom other than k . As equation (2.13) is qualitatively equivalent to equation (2.9), the same holds true for the Zhou-potential. By applying the simplification

$$p_{x \rightarrow y}^{\star \text{acc}} = \min\left(1, e^{-\beta \Delta E_k}\right), \quad (2.23)$$

we took the loss of detailed balance, but reduced the computational effort from $\mathcal{O}(N^2)$ to $\mathcal{O}(N)$, where N is the number of atoms. Though, the extensive validation process as well as the promising results of the simulations proved that the violated

MH algorithm is feasible at least (see section 3.1).

2.5.3. Velocity Verlet algorithm (Molecular Dynamics)

The symplectic second-order¹³ integrator used in the Molecular Dynamics simulations is based upon the well approved method commonly known as the Stoermer-Verlet algorithm. It was applied to Molecular Dynamics by Verlet (1967) and its Velocity Verlet adaption, which stands out due to improved numerical stability, has been stated by Swope *et al.* (1982, p. 648f, Appendix). It obeys the calculation rules

$$x_{n+1} = x_n + h \cdot v_n + \frac{h^2}{2} \cdot f(x_n) \quad (2.24)$$

$$v_{n+1} = v_n + \frac{h}{2} \cdot [f(x_{n+1}) + f(x_n)], \quad (2.25)$$

where x_n and v_n are position and velocity after the n -th time step, $f(x)$ is the acceleration (calculated by Newton's law), and $h = \Delta t = t_{n+1} - t_n$ is the size of a time step.

The conducted MD simulations have been carried out via LAMMPS¹⁴, a voluminous open source software package developed by Plimpton *et al.* (2017). They were performed at constant temperature, so neither the total energy nor the total momentum is conserved. This enables the system to be relaxed and thermodynamically equilibrated. More information about Molecular Dynamics at constant temperature can be found in the book by Frenkel & Smit (2002, ch. 6.1).

2.5.4. Autocorrelation function

The statistical autocorrelation function is the Pearson correlation of process values at different times. The following statements are heavily based on the lecture notes belonging to the computer simulations course mentioned above.

Let X_τ be the random variable of a stochastic process X at time τ . We assume that $\langle X_\tau \rangle = \langle X \rangle$ and $\text{var}(X_\tau) := \langle X_\tau^2 \rangle - \langle X_\tau \rangle^2 = \langle X^2 \rangle - \langle X \rangle^2$ are time-independent. Then the autocorrelation function between two points in time with a lag of t does

¹³global error is $\mathcal{O}(\Delta t^2)$

¹⁴Large-scale Atomic/Molecular Massively Parallel Simulator

not depend on τ and becomes simplified to

$$\rho(t) := \frac{\text{cov}(X_\tau, X_{\tau+t})}{\text{std}(X_\tau)\text{std}(X_{\tau+t})} = \frac{\langle (X_0 - \langle X \rangle) (X_t - \langle X \rangle) \rangle}{\langle X^2 \rangle - \langle X \rangle^2}. \quad (2.26)$$

Stable estimator

Anyway, for a particular realization of a stochastic process (e.g. a time series with values $a_0, a_1, a_2, \dots, a_n$) estimators of quantities such as expectation values (e.g. the average value $\bar{a} := \frac{1}{N} \sum_{i=1}^N a_i$ as an estimator of $\langle A \rangle$) and the autocorrelation function have to be used. For the MC simulations, the so-called empirical autocorrelation function

$$\rho^E(t) := \frac{\sum_{j=1}^{N-t} (a_j - \bar{a}(t)) (b_j - \bar{b}(t))}{\sqrt{\sum_{j=1}^{N-t} (a_j - \bar{a}(t))^2 \sum_{k=1}^{N-t} (b_k - \bar{b}(t))^2}}, \quad (2.27)$$

was evaluated, where

$$b_j := a_{j+t} \quad (2.28)$$

$$\bar{a}(t) := \frac{1}{N-t} \sum_{j=1}^{N-t} a_j \quad (2.29)$$

$$\bar{b}(t) := \frac{1}{N-t} \sum_{j=1+t}^N a_j. \quad (2.30)$$

It contains time-dependent estimators $\bar{a}(t) \neq \bar{b}(t)$, which in fact cause the high stability of $\rho^E(t)$.

Autocorrelation times

In time series of Monte Carlo simulations, the autocorrelation function typically is a sum of decaying exponential functions:

$$\rho^E(t) = \sum_i c_i \exp\left(-\frac{t}{\tau_i}\right). \quad (2.31)$$

Therefore, autocorrelations on different time scales τ_i can be estimated from the slope of $\rho^E(t)$ in a semi-logarithmic plot versus t . In order to be able to estimate the autocorrelation function reliably, the simulation length should be at least a hundred

times larger than the largest autocorrelation length τ_{\max} . The so-called integrated autocorrelation time

$$\tau_{\text{int}} \stackrel{N \gg \tau_{\max}}{\approx} \frac{1}{2} + \sum_{t=1}^N \rho(t) \quad (2.32)$$

is used to calculate the actual variance of an observed average value

$$\sigma_a^2 = \frac{\sigma_{a_i}^2}{\frac{N}{2\tau_{\text{int}}}}, \quad (2.33)$$

so the effective number of measurements is lowered by a factor of $2\tau_{\text{int}}$.

2.6. Statistics and data analysis

Briefly, some basic statistical concepts, which were mainly used for the validation of the Monte Carlo relaxation code and the analysis of the relaxed models, are denoted. Additionally, the Gaussian model function used here and there is declared.

Key values

Let $\{x_i\}$ be a finite sample of N values. We define the sample mean

$$\bar{x} := \frac{1}{N} \sum_{i=1}^N x_i \quad (2.34)$$

and the sample variance

$$s_x^2 := \frac{1}{N-1} \sum_{i=1}^N (x_i - \bar{x})^2. \quad (2.35)$$

From the central limit theorem the standard deviation of the sample mean (SDOM)

$$s_{\bar{x}} = \frac{s_x}{\sqrt{N}} \quad (2.36)$$

can be derived.

The sample median \tilde{x} is any real value for which

$$p(x_i \leq \tilde{x}) \geq 0.5 \quad \wedge \quad p(x_i \geq \tilde{x}) \geq 0.5 \quad (2.37)$$

2. Fundamentals and methods

is satisfied, where p is the relative frequency of occurrence. If the condition is true for a range of values $\tilde{x}_{\min} \dots \tilde{x}_{\max}$, which might be the case if N is even, one usually takes $\tilde{x} = \frac{1}{2}(\tilde{x}_{\min} + \tilde{x}_{\max})$.

Furthermore, the sample coefficient of variation¹⁵

$$c_v := \frac{s}{\bar{x}} \quad (2.38)$$

and the sample skewness

$$v := \frac{\frac{1}{N} \sum_{i=1}^N (x_i - \bar{x})^3}{s_x^3} \quad (2.39)$$

were used as statistical indicators.

(Dunn, 2010, ch. 5, 6)

Fitting of Gaussian functions to series of data points

Whenever the assumption that an obtained data set is approximately normally distributed was somewhat meaningful, even if the distribution of the values was not symmetric to an extremely high degree, the model function

$$f(\mu_{\text{gf}}, \sigma_{\text{gf}}, a, d, x) = d + a \exp \left[-\frac{1}{2} \left(\frac{x - \mu_{\text{gf}}}{\sigma_{\text{gf}}} \right)^2 \right] \quad (2.40)$$

was used.

¹⁵also known as the relative sample standard deviation

3. Results and analysis

The outcomes of the comprehensive simulation activities are presented beforehand, because this work was about simulating and analyzing simulation results for the most part. Anyway, since possessing knowledge of the experimental results in advance is crucial to understand the course of action during the simulation part, especially readers unfamiliar with the topic are advised to swap the order and glance over the experimental section first.

In the simulation section 3.1 I rigorously focus on two aspects. First, the sequential explanation and annotation of the realized simulation concepts should allow the reader to comprehend the process of approaching experimental results step-by-step. Second, the numerous graphs are described and interpreted as objectively as possible, but for all that, assumptions concerning unaccounted effects are not omitted.

As far as the experimental section 3.2 is concerned, the main focus is layed on presenting obtained (S)TEM images and the quantitative analysis of them. In addition, opportunities to compare the results of experiments and simulations are demonstrated by means of an example. The limitations of the comparability are sketched later in section 4.2.

3.1. Simulation results

To start with, a perfect fcc gold matrix, featuring no crystal defects and deformations, was created and STEM images of it were simulated via QSTEM. All the simulations have been performed with the specimen model in the [001] zone axis. The obtained images were analyzed in a quantitative manner with respect to the specimen thickness t and the angles aforementioned in section 2.2.1 and figure 2.5, namely the convergence angle α of the primary electron beam and the collection angle β of the detector.

Next, gold-nickel alloy models were made. First, the gold atoms of a single atom column in the direction of the electron beam were substituted by nickel atoms. Every further model contained a gradually more complex arrangement of substitutional nickel atoms in the gold matrix. After generating simulated images of these, the quantitative analysis was continued and the effects of nickel impurities were investigated. Although the models were unrealistic due to the absence of lattice deformations, the results constitute a reference point for what happens in the micrographs.

Later, models closer to real spinodally decomposed gold-nickel specimens were created by performing lattice relaxations with MC- and MD-simulations. A major difficulty for the comparability with experiments arose from the computational effort. For every QSTEM simulation, a trade-off between size of the simulated scanning region, resolution and model thickness had to be found. The models' thickness was 60 nm at most, whereas the experimentally investigated specimen regions are at least as thick as that.

Complementarily, diffraction patterns were simulated, using coherent CBED simulations in combination with a very small convergence angle in order to approximate SAED images.

In order not to overload this section with figures too heavily, not every single effect is explicitly depicted graphically for every model. Instead, as every subsequent model has new properties, the respective result analysis is more focused on aspects not present in the previous one. Unless otherwise noted, features elaborated for a simple model apply for the structurally more complicated ones as well.

QSTEM settings

In well conformity with the Titan microscope, the following parameters were used:

- Acceleration voltage: 300 kV (De Broglie wavelength $\lambda_B \approx 1.97$ pm)
- 3rd order spherical aberration coefficient (C_s): 0.001 mm
- Astigmatism coefficient: 0
- Defocus: -1.7 nm (Scherzer condition)
- Chromatic aberration coefficient (C_c): 1 mm
- Primary electron energy distribution width: 0.6 eV
- Temperature: 300 K

- Number of TDS runs to be averaged over: 30
- Dwell time: 1 μ s, no beam damage considered

3.1.1. QSTEM images of models with a perfect fcc lattice

All models that were not put into our alloy relaxation code are listed and specified in table 3.1. Figure 3.1 illustrates them schematically in a smaller style, since drawings of the full-size models would not emphasize the substantial aspects that well.

The first models handed over to QSTEM were quite uncomplicated in terms of structure and composition. Due to the simplicity of the arrangement of substitutional foreign Ni atoms it was possible to generate models 1 to 4 by manipulating a Crystallographic Information File downloaded from FIZ Karlsruhe - Leibniz Institute for Information Infrastructure (2016, [online], Coll. Code 52700) with the CrystalMaker software package (Palmer *et al.*, 2016, [online]).

As the Ni substituent distribution becomes more complex and thereby more realistic, a graphical solution in which selecting atoms is done by drawing a frame around them gets unsuitable. For this reason, a few MATLAB scripts were written in order to create the desired XYZ-files (see appendix A.2). According to the description in table 3.1, the code, for instance, generates model 5 with $c_{\text{Ni}}(x, y, z) = \sin^2(\frac{x}{\lambda}\pi) \cdot (c_{\text{max}} - c_{\text{min}}) + c_{\text{min}}$. Up to a rounding error, the value of $c_{\text{Ni}}(x_i)$ is valid for a specific (100)-plane with $x = x_i$. In y - and z -direction, the Ni atoms are randomly distributed by utilization of the MATLAB command `randperm`.

Table 3.1.: Overview of the nickel impurities in the models used without lattice relaxation

model no.	type of Ni impurity
1	none
2	single atom column $\parallel \vec{z}$, [001]
3	single (100) lattice plane
4	parallel (100) lattice planes, distance = $2 \cdot a_{\text{Au}}$, periodically
5	sine-squared-shaped modulation in \vec{x} -direction, $\lambda = 2 \cdot a_{\text{Au}} = 0.815788 \text{ nm}$, $c_{\text{min}} = 0$, $c_{\text{max}} = 0.6$
6	sine-squared-shaped modulation in \vec{x} -direction, $\lambda = 0.77 \text{ nm}$, $c_{\text{min}} = 0$, $c_{\text{max}} = 1$

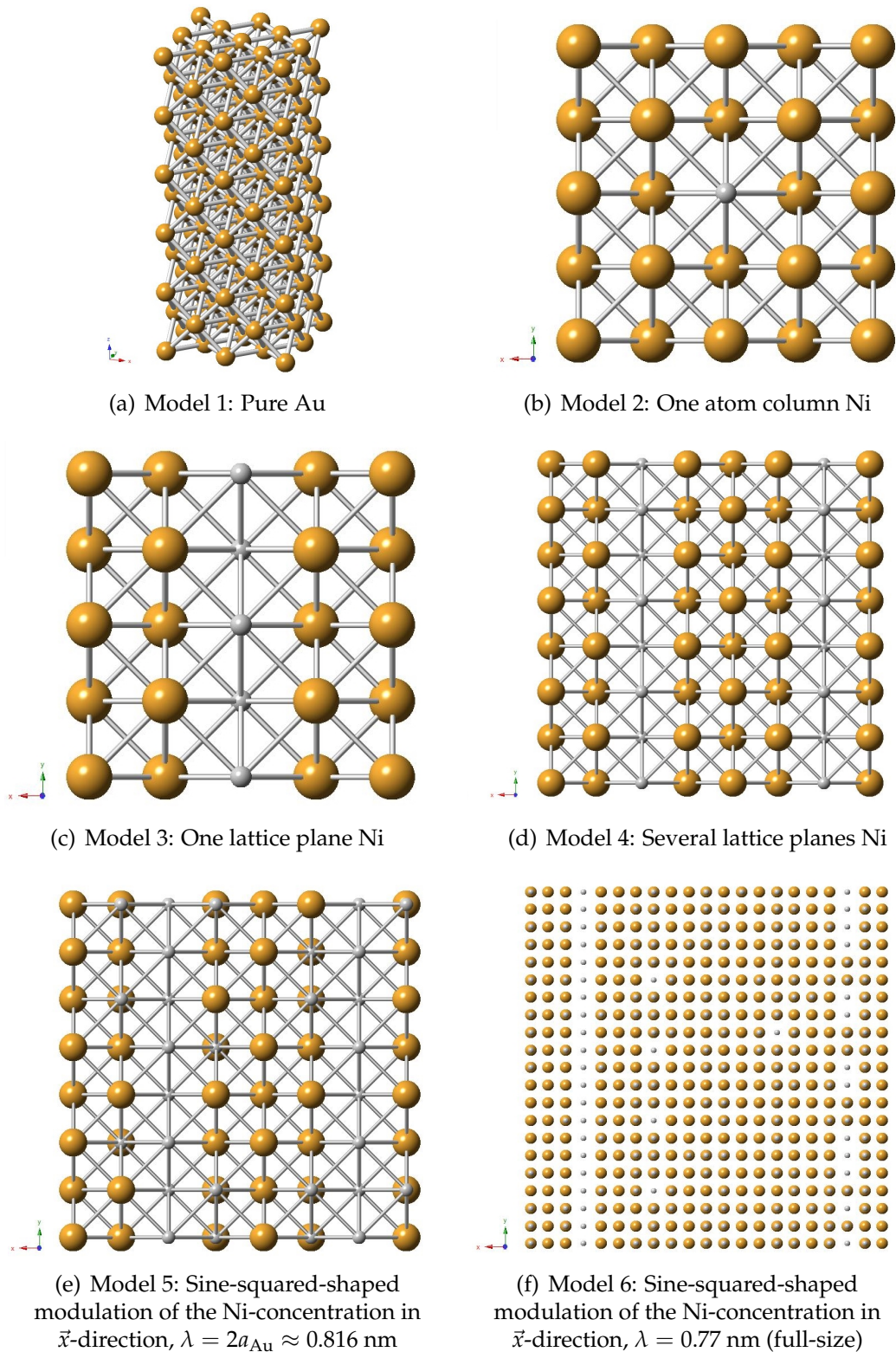


Figure 3.1.: Inclined crack of simulation model 1 (a) and views of models 2 to 6 along the [001] direction (b to d); All structures have a perfect fcc lattices with $a = a_{\text{Au}} = 0.407894$ nm. The large golden spheres represent Au atoms, the small silver ones are Ni. The lines link nearest neighbors in the lattice and their primary purpose is to illustrate the 3D topography.

Model 1: Pure Au

The first model had a size of $4.07894 \times 4.07894 \times 61.18410 \text{ nm}^3$ ($10 \times 10 \times 150$ fcc unit cells) and consisted of 66371 atoms. The number of atoms is greater than $10 \cdot 10 \cdot 150 \cdot 4$, because in each direction the confining conventional unit cells are completed in order to obtain inversion symmetry. The electron beam was scanned across a square of $1 \times 1 \text{ nm}^2$ and, hence, covered 5×5 columns containing 150 or 151 atoms each.

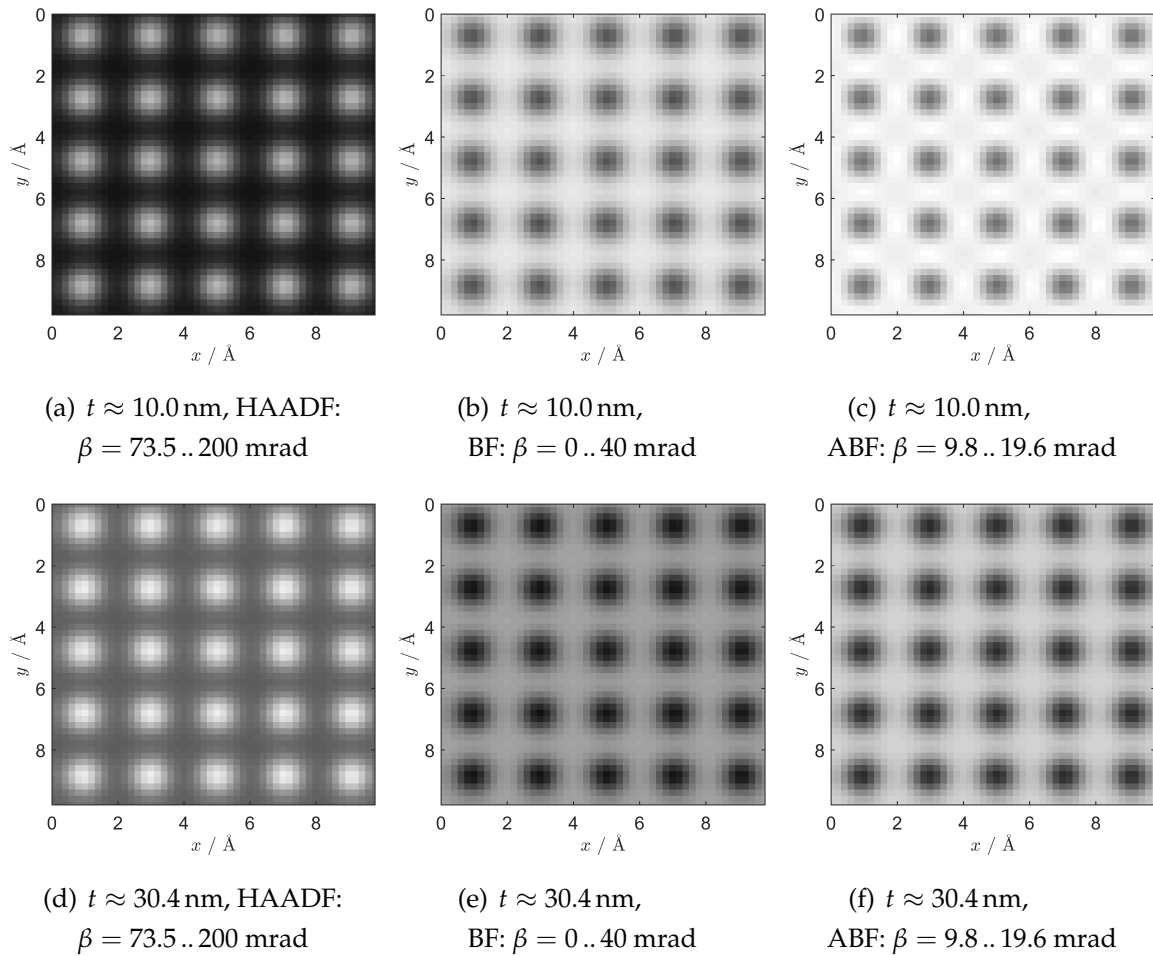


Figure 3.2.: Model 1: QSTEM HAADF-, BF-, and ABF-images for different thicknesses t ; The convergence angle was $\alpha = 19.6 \text{ mrad}$. The color scale is not the same for images of different detectors. Black and white in the pictures correspond to intensity values of 0.0 and 0.3 for HAADF-images, 0.6 and 1.0 for BF-images, and 0.3 and 0.6 for ABF-images. Thus, the comparability between detectors by means of these images is limited to a qualitative manner.

Figure 3.2 shows exemplary QSTEM images of this model. The atom columns appear bright in the HAADF- and dark in the BF- and ABF-images. The contrast between

3. Results and analysis

10 and 30 nanometers in thickness can clearly be seen by the human eye. Besides that, we recognize a distinctly increased background intensity in the HAADF image for $t \approx 30$ nm (see figure 3.2(d)) when compared to the one for $t \approx 10$ nm (see figure 3.2(a))

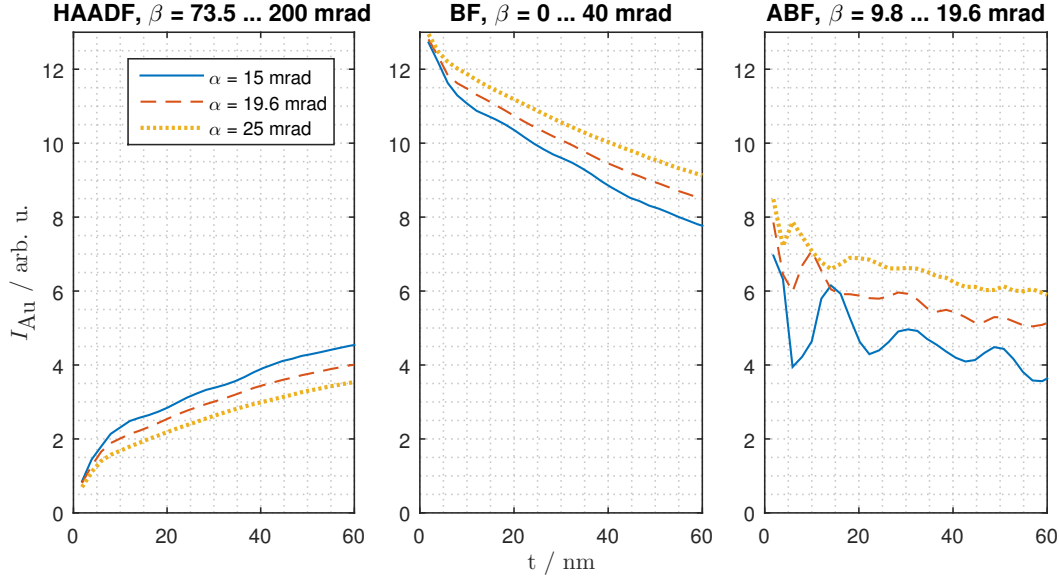


Figure 3.3.: Model 1: Average HAADF-, BF-, and ABF-intensity of gold atom columns vs. thickness for different convergence semi-angles

Figure 3.3 shows the electron intensity stemming from the locations of the gold atoms columns and hitting the different detectors as a function of the model thickness. We see that the intensity is a non-linear function of thickness for all investigated detector types. The HAADF-intensity increases substantially with thickness up to about 5 nm, then there is a gentle kink between 5 and 10 nm and after that the slope further flattens out. This behavior can be reasoned by coherent phonon scattering for low penetration depths and the presence of electron channeling conditions in the [001] zone axis (see fundamentals section 2.2.2) and is similar to the frozen phonon results for Sr and Ti-O columns obtained by LeBeau *et al.* (2008, FIG. 3). In the BF images we observe the opposite behavior. The ABF signal shows oscillating characteristics, which could not be justified. The periodicity changes with the convergence angle. The distance between the maxima seems not to correspond to extinction distances in crystalline gold, but we are not entirely sure whether it is somehow associated with the observed oscillations. Furthermore, the collection angle range in the BF region was split into four sections, namely $\beta = 0 \dots 9.8$ mrad, $9.8 \dots 19.6$ mrad (ABF), $19.6 \dots 29.4$ mrad, and $29.4 \dots 39.2$ mrad, but the intensity-versus-

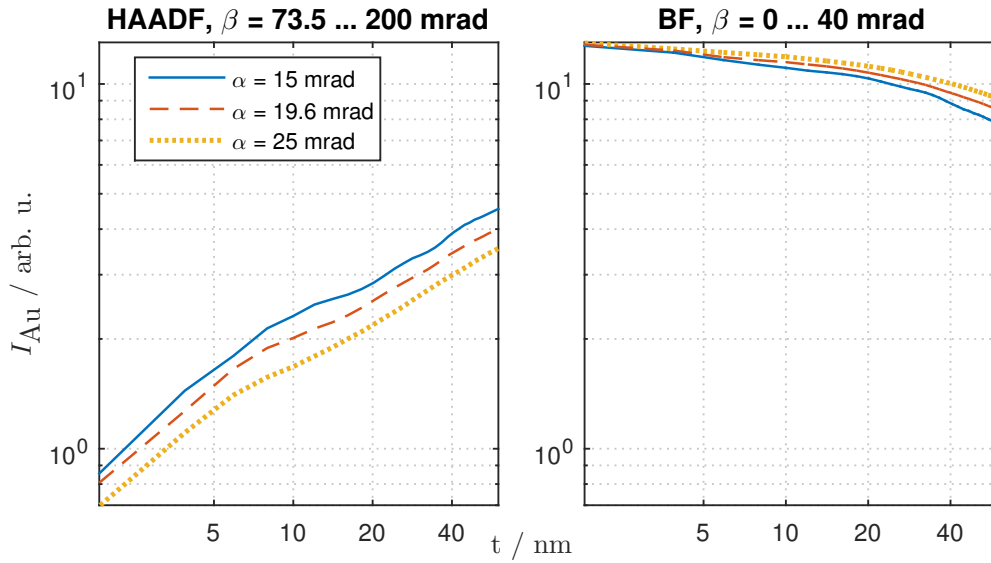


Figure 3.4.: Model 1: Log-log plot of mean HAADF- and BF-intensity vs. thickness for different convergence semi-angles

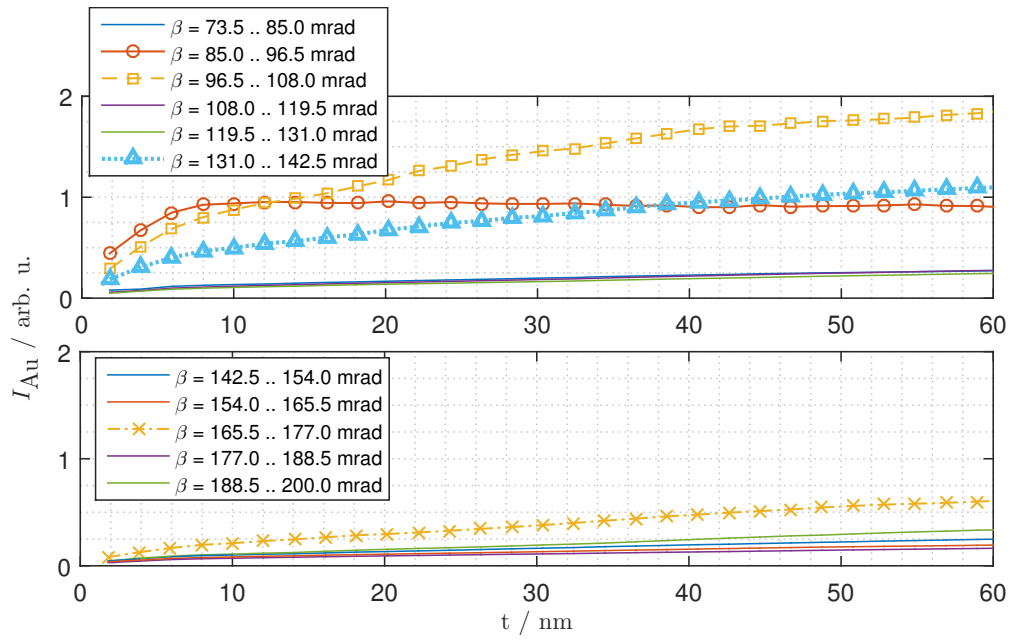
thickness curves exhibit an irregular behavior for β -ranges other than the one of the ABF (no figure). As far as the convergence angle is concerned, the intensity becomes lower in HAADF images with higher α , but higher in BF/ABF images. The higher the convergence angle is chosen, the lower the slope $\Delta I / \Delta t$ gets for all detector types. The speculative presumption that the mean convergence semi-angle of the incoming electrons adds to the scattering angle, with the effect that more electrons are scattered to higher angles with respect to the optical axis for higher convergence semi-angles, is disconfirmed.

In figure 3.4, the same HAADF- and BF-data is illustrated again, but in log-log representation. The absolute value of the slope in these graphs is correlated with the relative thickness contrast $\left| \ln \frac{I(r, t_{\text{ref}})}{I(t_{\text{ref}})} \right|$. For a given r , the HAADF relative thickness contrast is almost constant for thicknesses in this range, being slightly better for thin specimens. The BF relative thickness contrast is much weaker than in the HAADF, but its dependence on thickness is higher. It gets better for thicker specimens. In addition, lower convergence angles enhance the BF relative thickness contrast, whereas the convergence angle has a minor effect on the HAADF contrast.

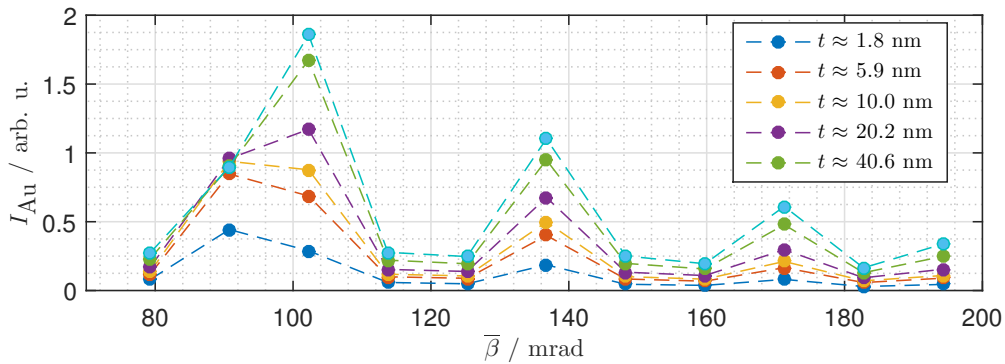
As mentioned in section 2.3.2, the total collection semi-angle range for the HAADF detector, $\beta = 73.5 \dots 200$ mrad, was split into 11 evenly large regions, each 11.5 mrad in width, corresponding to annular "subdetectors". Figure 3.5 illustrates the angular distribution of the electrons scattered into the HAADF region. We would ex-

3. Results and analysis

pect monotonously decreasing intensities with increasing angles if we considered incoherent and no multiple scattering (Remember: Rutherford differential scattering cross-section $\frac{d\sigma}{d\Omega} \propto \sin(\theta/2)^{-4}$). This expectation is not met. The majority of electrons hit the detector in regions corresponding to 4 subdetectors which are not neighbors with regard to their β -range. For $\beta = 85 \dots 96.5$ mrad, the intensity grows linearly up to $t \approx 6$ nm, then flattens out and decreases slightly for $t \geq 20$ nm. All other intensity curves in figure 3.5(a) have a positive slope and a negative curvature.



(a) Absolute intensity vs. thickness split by collection angle



(b) Absolute intensity vs. mean collection semi-angle for various thicknesses;

The values of the mean collection semi-angle $\bar{\beta}$ are the centers of the HAADF subdetectors' β -ranges, e.g. $\bar{\beta} = 79.25$ mrad for $\beta = 73.5 \dots 85.0$ mrad.

Figure 3.5.: Model 1: Average HAADF-intensity of gold atom columns vs. thickness (a) and average HAADF-intensity vs. mean collection semi-angle (b) for $\alpha = 19.6$ mrad

Model 2: One Ni atom column

This model had a single Ni atom column parallel to the [001]-direction in its center and was identical to model 1 at all other points. The most interesting questions concern the Au-Ni contrast and whether the presence of Ni atoms affect the intensity of neighboring Au atoms. To get an idea of how QSTEM images of this model look like, one per detector is shown in figure 3.6.

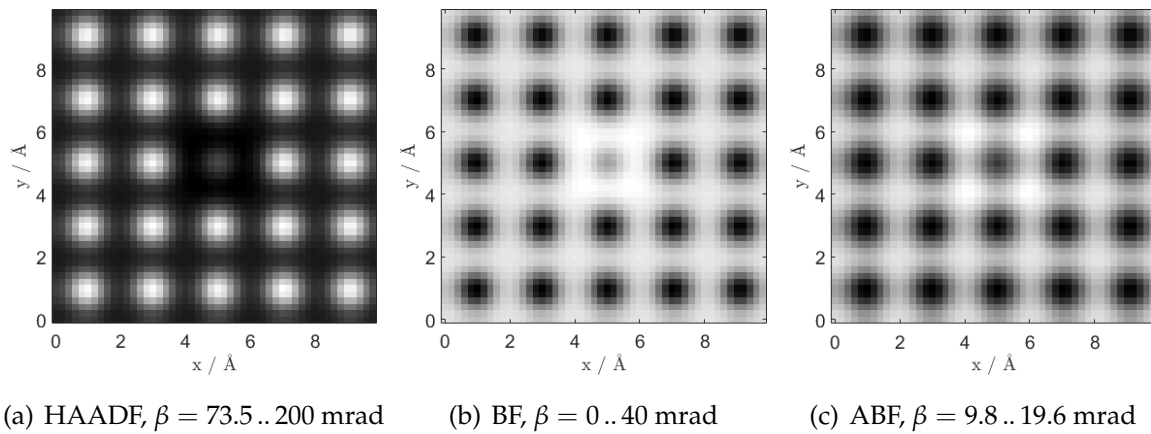


Figure 3.6.: Model 2: QSTEM HAADF-, BF-, and ABF-image for $t \approx 20.2$ nm and $\alpha = 19.6$ mrad. Note that the given pictures are only suitable for qualitative comparison, because the color scale is not the same for images of different detectors.

As for the convergence semi-angle, larger values lead to a little better HAADF-, but slightly worse BF- and ABF-contrast (no figure). The effect is below $\pm 2\%$ and was not topic of further investigations. From now on, all results arise from simulations with a convergence angle of $\alpha = 19.6$ mrad.

Figure 3.7 shows the absolute intensity stemming from the nickel column as well as the intensity ratio of nickel and gold as a function of thickness, both for all three used detector types. The absolute intensity for gold columns is not visualized there, because the changes compared to figure 3.3 concerning model 1 are very small (see below for details on HAADF). As for nickel, both the HAADF- and BF-intensity are extensively linear functions of thickness, indicating that channeling effects should be quite weak for nickel. The ABF-intensity exhibits an oscillating behavior, as we noticed for gold as well. The HAADF-contrast is better, the thinner the specimen model is. The relative intensities should approach 1 for large thicknesses at the point of electron opacity. As far as the BF-contrast is concerned, it remains roughly constant in the investigated thickness range. Due to the oscillating signal in ABF images, they

3. Results and analysis

offer better Au-Ni contrast than the BF detector for some thickness values. Although the BF-/ABF-contrast is distinctly detectable by the human eye, because the relative intensity values are mostly above 1.1 resulting in contrast values of $C_{In} \geq 10\%$, it is much weaker than for HAADF images.

Regarding the HAADF detector, the absolute gold, the absolute nickel, and the relative nickel-to-gold intensity, all as a function of thickness, split by collection angle and normalized with respect to the number of atom columns, are depicted in figure 3.8. The gold intensities can be compared to figure 3.5(a). Their behavior is very similar to model 1. The relative deviation from model 1 and between Au columns next to the Ni column and farther away from it, is lower than 2%. Outliers were not statistically evaluated due to their rare occurrence, however, a deviation greater than 4% has not been observed. As for the nickel column, the angular distribution of electrons scattered to the HAADF collection range is different, resulting in the Au-Ni contrast varying from subdetector to subdetector. At some points, the relative intensities cross the zero-contrast-line ($I_{Ni} : I_{Au} = 1$) and the nickel column appears brighter than the gold columns on average.

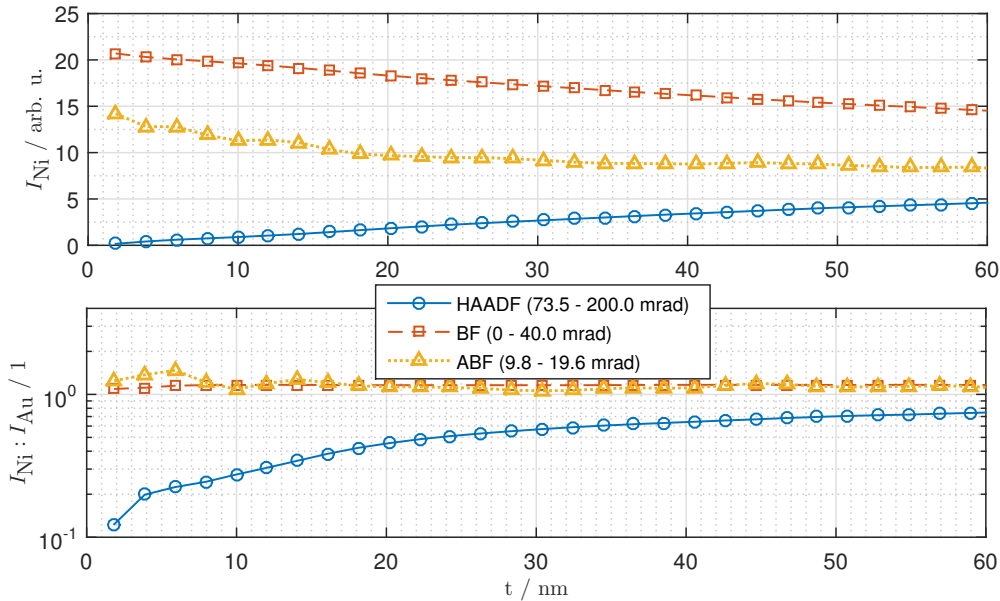


Figure 3.7.: Model 2: Average HAADF-, BF-, and ABF-intensity of nickel atom columns vs. thickness (top) and relative nickel-to-gold intensity vs. thickness in a semi-logarithmic plot corresponding to the Au-Ni contrast (bottom); In the contrast plot, data points far away from the line $\log_{10}(I_{Ni} : I_{Au}) = 0$ represent better contrast than points closer to it. The semi-logarithmic representation is used because the perceived contrast is proportional to the logarithm of the intensity ratio (see section 2.2.2). Equal visual distances in direction of the ordinate correspond to equal intensity ratios.

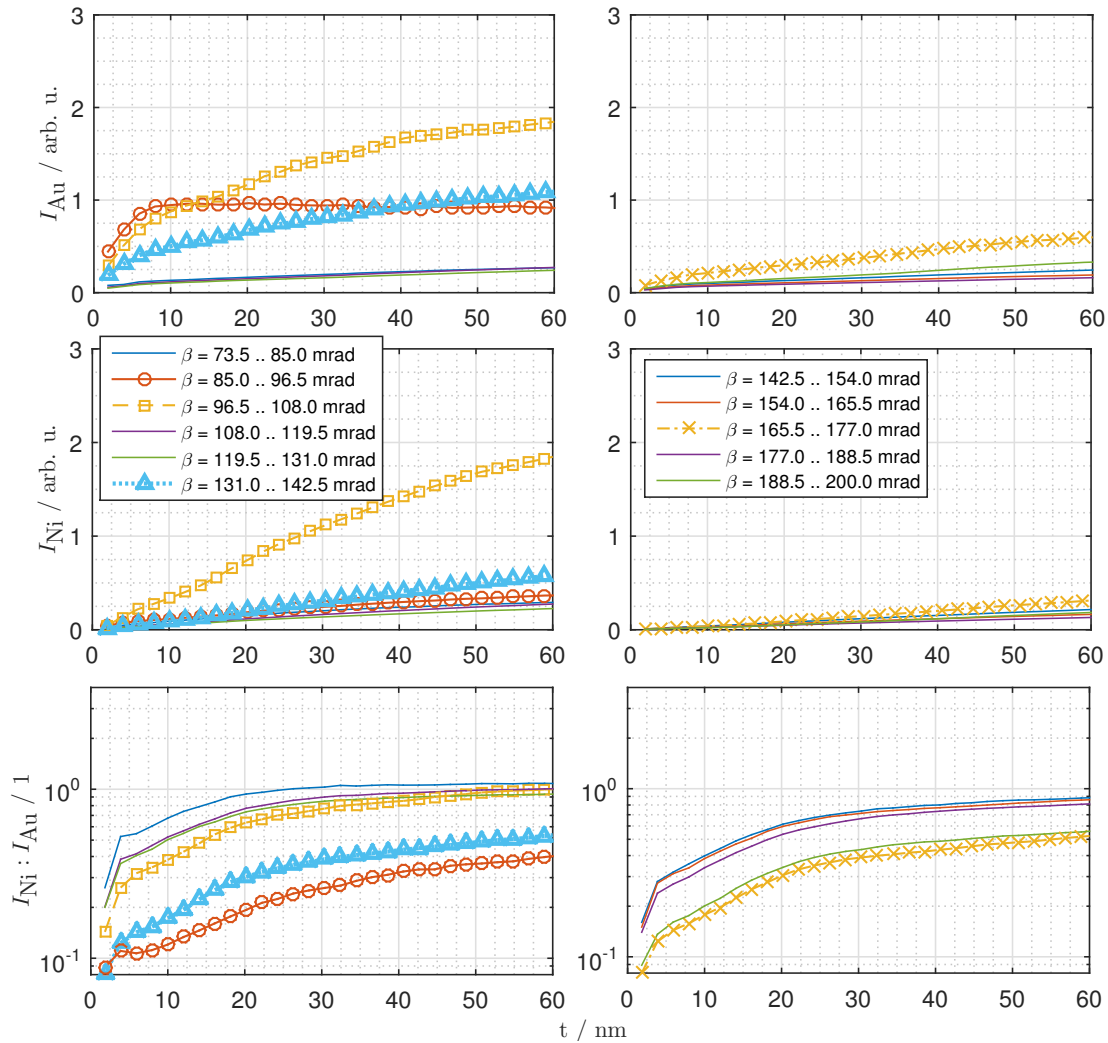


Figure 3.8.: Model 2: Average HAADF-intensity of gold and nickel vs. thickness (top and middle row) and relative nickel-to-gold intensity vs. thickness in semi-logarithmic representation (bottom row), all split by collection semi-angle

Model 3: One Ni lattice plane

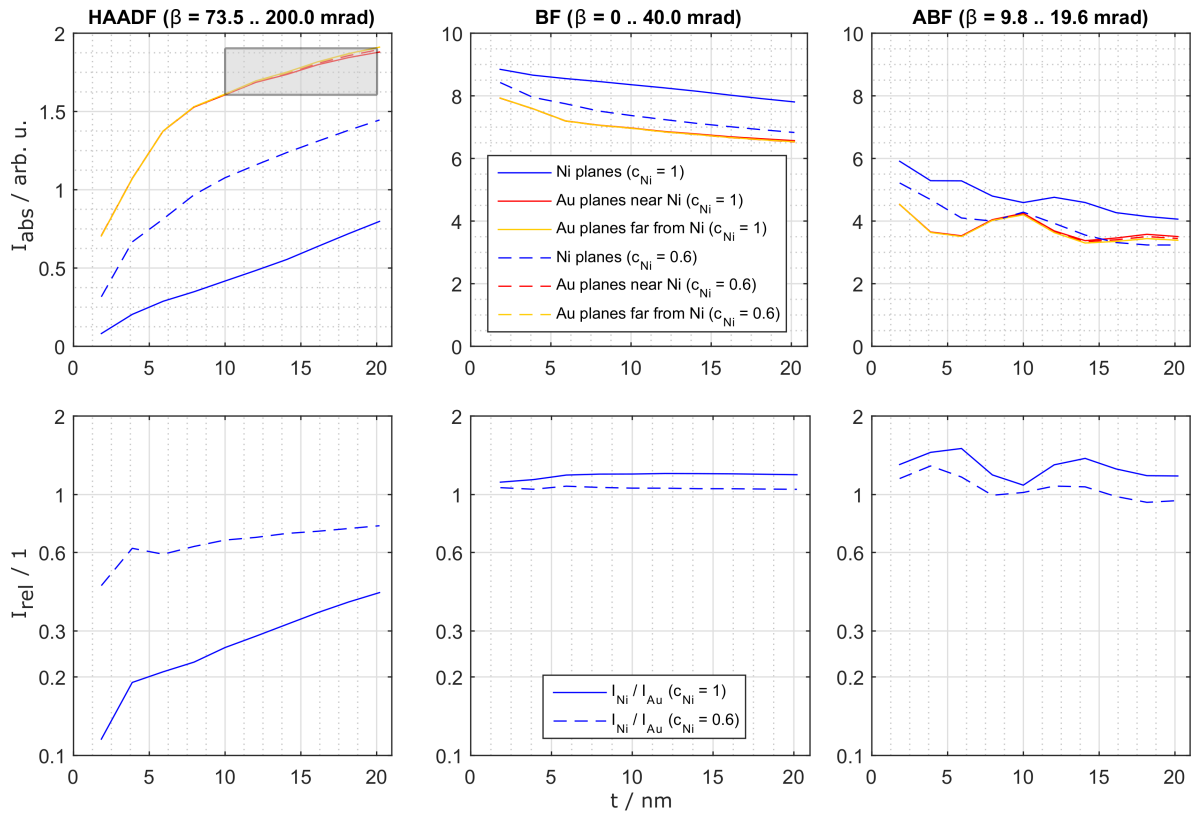
The only difference to model 2 was a (100) Ni lattice plane, instead of an atom column, through its center. The evaluation of the simulated images yielded very similar results as we obtained for model 2, so no new insights were gained. Therefore, any graphical data and further discussion is omitted.

Model 4: Parallel Ni lattice planes

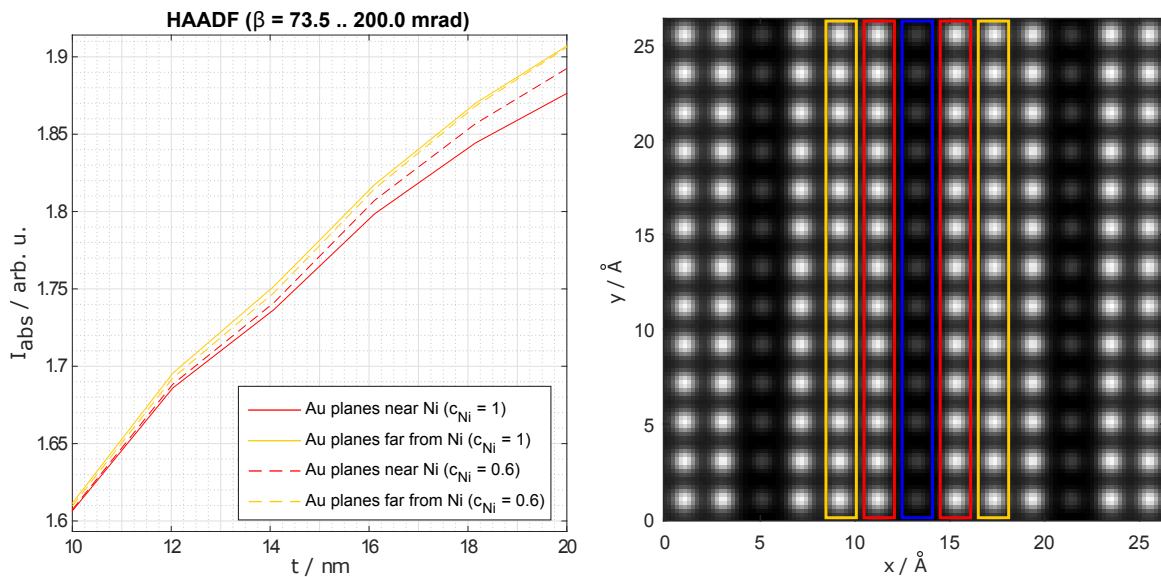
In this model, every fourth plane perpendicular to the [001]-direction was replaced by a nickel-yielding plane. Two different configurations, model 4a with $c_{\text{Ni}} = 1$ and model 4b with $c_{\text{Ni}} = 0.6$ in the nickel-yielding planes, were simulated. The electron beam was scanned across a square of $\approx 2.65 \times 2.65 \text{ nm}^2$ and covered 13×13 columns, thus 6×6 conventional unit cells. The model had a size of $4.07894 \times 4.07894 \times 20.39470 \text{ nm}^3$ ($10 \times 10 \times 50$ fcc unit cells). It is only a third of the previous models in thickness, because the computational effort would have become too large if the model had not been thinned.

In the scope of the result analysis, it is appropriate to classify the model into three regions: Nickel-rich columns, gold columns next to nickel-rich columns, and gold columns farther away from nickel-rich columns. Figure 3.9 illustrates a QSTEM HAADF image and electron intensities stemming from these different regions as a function of thickness. All solid lines belong to model 4a, all dashes ones to model 4b. We observe the same effects we have already noticed for the previous models, such as a non-linear intensity dependence on thickness, oscillating ABF-intensities, and generally weak Z-contrast for BF- and ABF-signals. Again, not only absolute intensities are visualized, but also intensity ratios of nickel(-rich) and gold planes in semi-logarithmic representation (see lower row of graphs in figure 3.9(a)). As for BF- and HAADF-intensities, the lines for the relative intensities $I_{\text{rel}}(c_{\text{Ni}} = 0.6)$ and $I_{\text{rel}}(c_{\text{Ni}} = 1)$ are farther away from each other than the line for $I_{\text{rel}}(c_{\text{Ni}} = 0.6)$ from 1, which is the intensity from pure gold columns. This means that the Weber-Fechner contrast between $c_{\text{Ni}} = 1$ and $c_{\text{Ni}} = 0.6$ is higher than between $c_{\text{Ni}} = 0.6$ and $c_{\text{Ni}} = 0$.

Even though, as stated before, the effect of atom columns on their neighboring ones is minor, a few things about it are worth noting by means of a comment on figure 3.9(b). The relative intensity difference between gold planes near and far from nickel is higher for thicker specimens. For $t \approx 20.2 \text{ nm}$ and model 4a with pure nickel planes, the HAADF-intensity stemming from gold planes next to the nickel planes (red regions/curves) is $\approx 1.6 \%$ lower compared to gold planes far from nickel (yellow regions/curves). On the other hand, the BF-intensity is $\approx 0.6 \%$ and the ABF-intensity $\approx 1.9 \%$ higher. Anyhow, the Weber contrast stays below $\pm 2 \%$ and is not perceptible for the human eye.



(a) Absolute (upper row) and relative (lower row) average HAADF-, BF-, and ABF-intensity vs. thickness; The marked region in the upper HAADF graph is enlarged in figure 3.9(b).



(b) Absolute average HAADF-intensity vs. thickness for gold planes

(c) QSTEM HAADF image of model 4a for $t \approx 14.1 \text{ nm}$

Figure 3.9.: Model 4: Analysis of different specimen regions; blue region: nickel-rich planes, red region: gold planes near nickel, yellow region: gold planes far from nickel

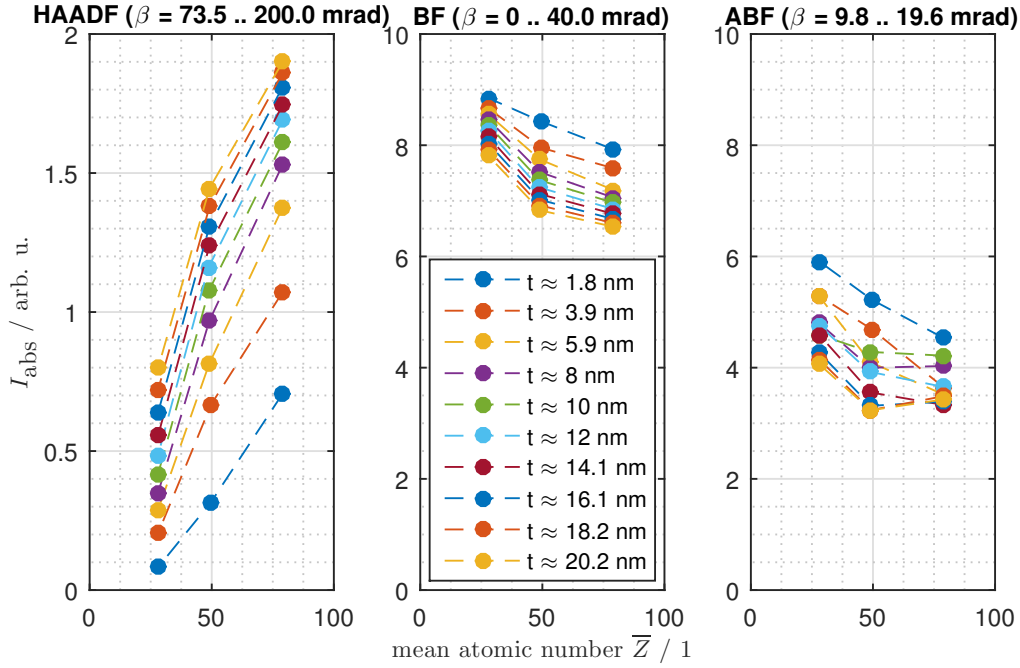


Figure 3.10.: Model 4: Average HAADF-, BF-, and ABF-intensity vs. mean atomic number for different thicknesses

In figure 3.10, absolute intensities as a function of the mean atomic number are depicted. It is basically the same data differently put into graphs, but thought has been given to the uniform distribution of the nickel atoms in the y - and the z -direction, leading to slightly fluctuating mean atomic numbers for the mixed planes in model 4b ($\bar{Z} \approx 50$). If the assumption that scattering from many atoms can be added coherently was correct, we would notice that γ_c in $I_{\text{HAADF}} - I_{\text{background}} \propto \bar{Z}^{\gamma_c}$ is distinctly lower than 2. But for the most thickness values, the slope of the HAADF-intensity gets flatter with higher mean atomic number. Theory, according to which the Z -dependence should be higher does not hold true for incoherent scattering from mixed atom columns and if the crystal is viewed in a zone axis.

**Model 5: Sine-squared-shaped modulation of the nickel concentration
(wavelength equals a multiple of the lattice parameter)**

This model had a nickel concentration modulation of $c_{\text{Ni}}(x, y, z) = \sin^2\left(\frac{x}{2a_{\text{Au}}}\pi\right) \cdot 0.6$ and was identical to model 4 at all other points. Because the wavelength has been set to two times the lattice parameter, the nickel concentration sequence in x -direction simply is $0 \rightarrow 0.3 \rightarrow 0.6 \rightarrow 0.3 \rightarrow 0 \rightarrow 0.3 \rightarrow \dots$. The electron beam was

scanned across a square of $\approx 1.63 \times 1.63 \text{ nm}^2$ and covered 8×8 columns, thus two wavelengths of the nickel concentration modulation.

Figure 3.11 depicts a QSTEM HAADF image of the model. The classification into three regions is similar to model 4. Figure 3.12 illustrates absolute and relative intensities as a function of thickness. Looking at the bottom left graph in figure 3.12, we recognize that the dashed red line intersects the dotted yellow one at several points. This means that the HAADF-contrast between $c_{\text{Ni}} = 0.6$ and $c_{\text{Ni}} = 0.3$ switches from being better than between $c_{\text{Ni}} = 0.3$ and $c_{\text{Ni}} = 0$ to being worse. As far as the pure gold planes and the planes with a nickel concentration of 0.6 are concerned, the qualitative changes compared to model 4 are negligible. The absolute intensity values in the upper row of graphs in figure 3.12 regarding model 5 are not of the same order of magnitude as the values in figure 3.9(a) belonging to model 4, because the sizes of the scanning region and the pixel dimensions do not match.

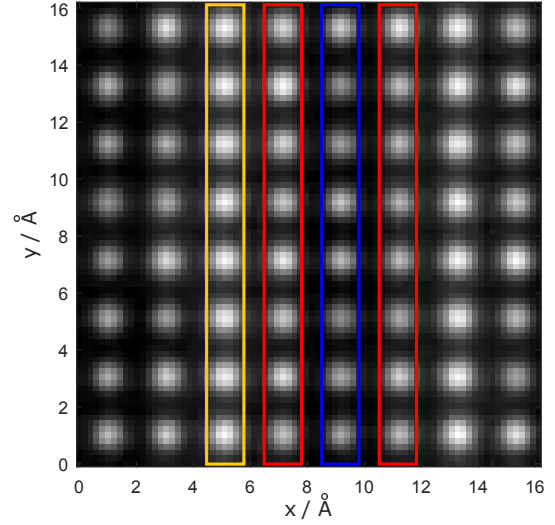


Figure 3.11.: Model 5: QSTEM HAADF image for $t \approx 18.2 \text{ nm}$; blue region: planes with $c_{\text{Ni}} = 0.6$, red region: planes with $c_{\text{Ni}} = 0.3$, yellow region: Au planes

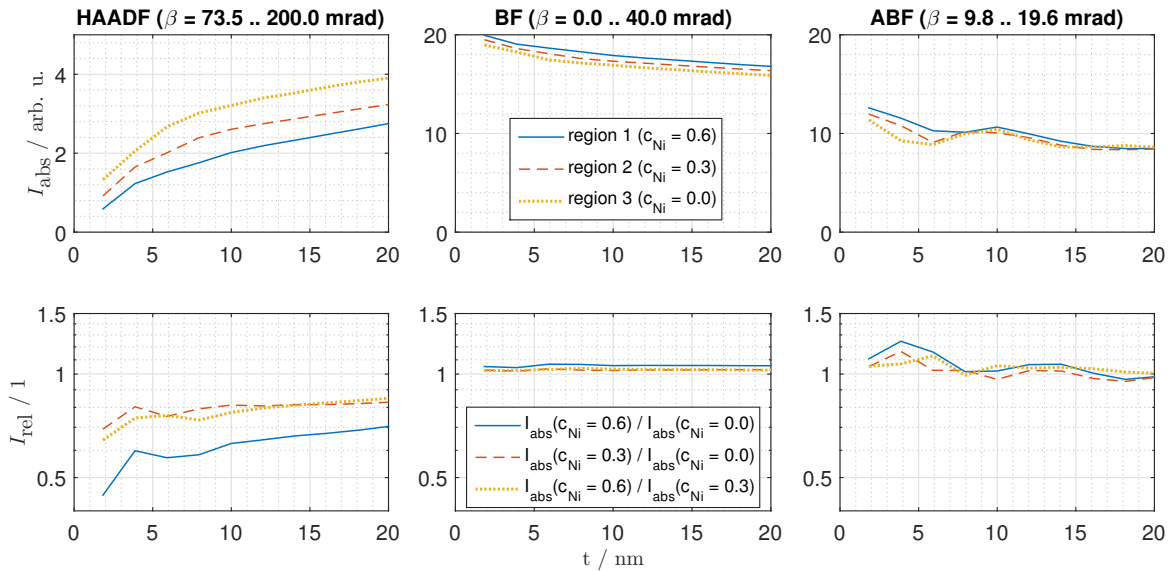


Figure 3.12.: Model 5: Absolute (upper row) and relative (lower row) average HAADF-, BF-, and ABF-intensity vs. thickness for different specimen regions

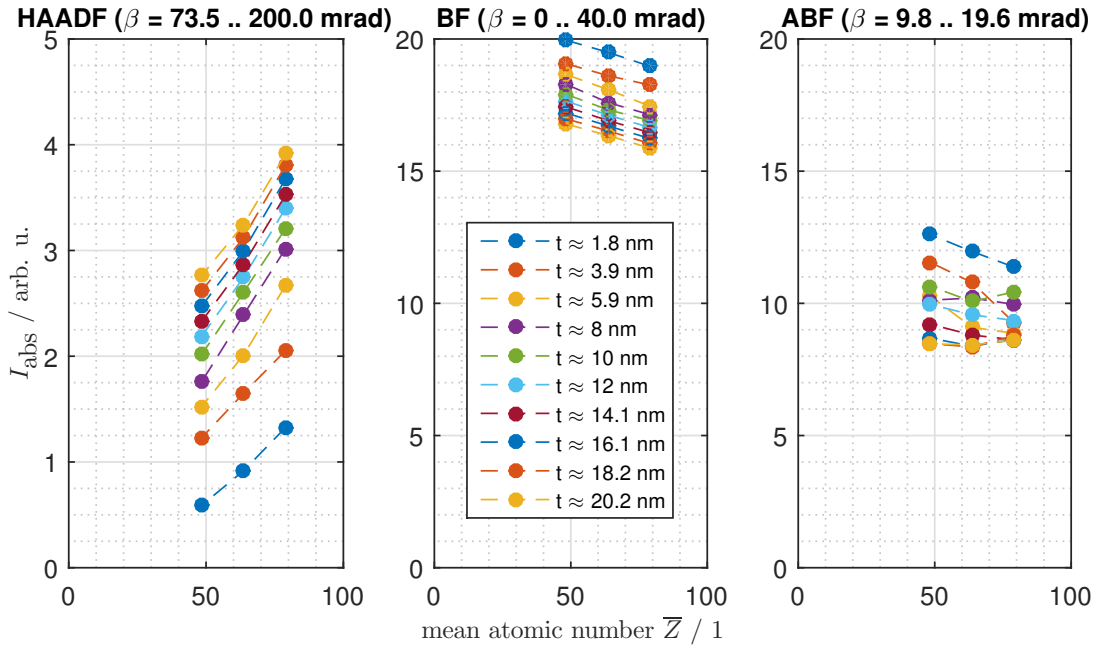


Figure 3.13.: Model 5: Average HAADF-, BF-, and ABF-intensity vs. mean atomic number for different thicknesses

Figure 3.13 shows absolute intensities as a function of the mean atomic number. By trend, the slope of the HAADF-signal grows for higher mean atomic number. We did not see this for model 4 due to a lack of nickel concentration values between 0.6 and 0. More discussion on these graphs is omitted, because the data obtained for the next model 6 is more revealing.

Model 6: Sine-squared-shaped modulation of the nickel concentration (wavelength of 0.77 nm)

This model had a size of $4.07894 \times 4.07894 \times 61.18410 \text{ nm}^3$ ($10 \times 10 \times 150$ fcc unit cells) and a nickel concentration modulation of $c_{\text{Ni}}(x, y, z) = \sin^2(\frac{x}{0.77\text{nm}}\pi)$. The total nickel concentration was $c_{\text{Ni}}^{\text{tot}} \approx 0.48$. As on model 4, the electron beam was scanned across a square of $\approx 2.65 \times 2.65 \text{ nm}^2$ and covered 13×13 columns. Because the wavelength has been offset from a multiple of the lattice parameter, the concentration sequence does not repeat within the examined scanning region. For that reason, this model allows us to investigate more individual nickel concentration values.

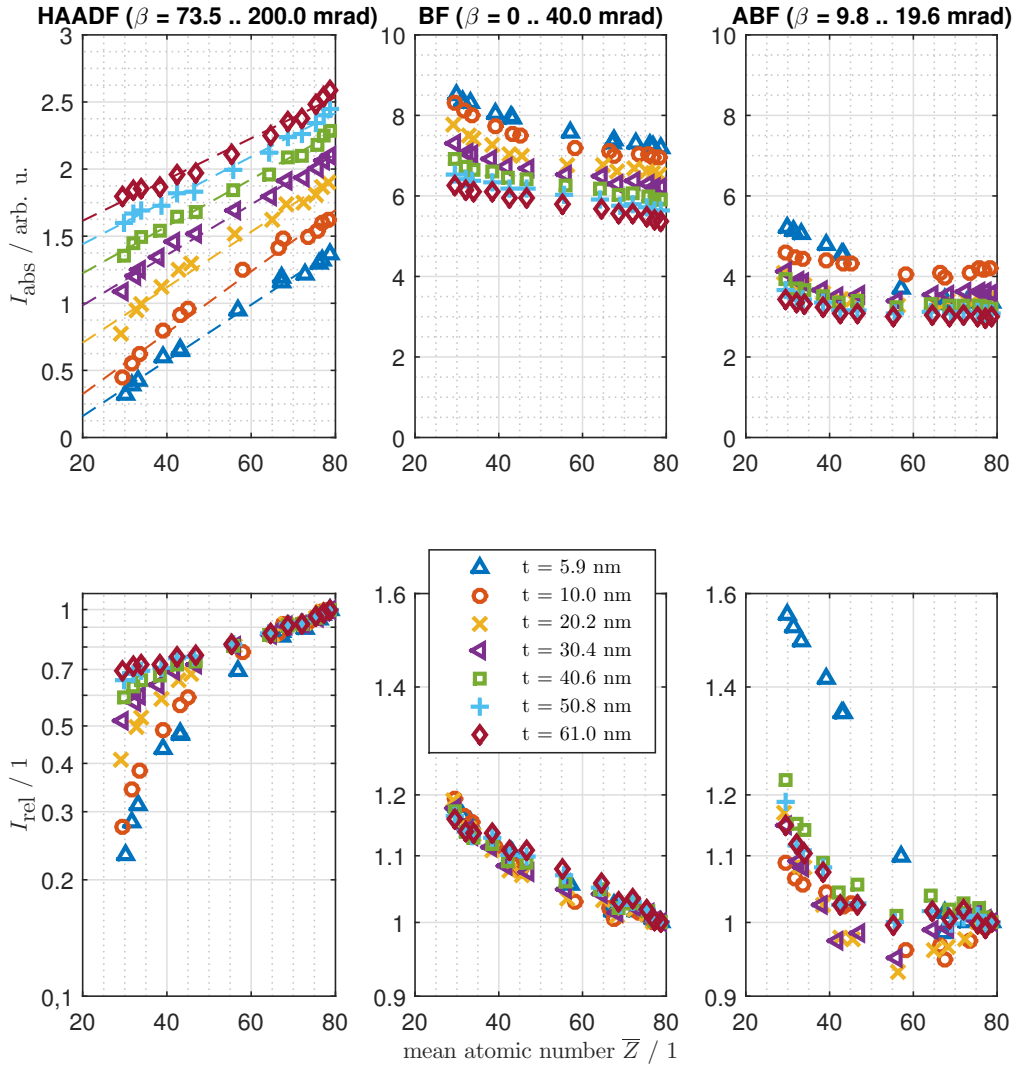


Figure 3.14.: Model 6: Absolute (upper row) and relative (lower row) average HAADF-, BF-, and ABF-intensity vs. mean atomic number for different thicknesses; The relative average intensity is $I_{\text{rel}} := \frac{I_{\text{abs}}(\bar{Z})}{I_{\text{abs}}(79)} \Big|_t$. The dashed lines in the absolute HAADF-intensity-plot (top left) are first order polynomial fits. Note that the scaling for the BF-/ABF-intensity is different to the one for the HAADF-intensity, both in the plots concerning relative as well as absolute intensities.

Figure 3.14 depicts absolute and relative intensities as a function of the mean atomic number for various thicknesses. It provides some more information about the \bar{Z} -dependence of the signals. The HAADF-background is increasing with thickness, which can be reasoned by electron channeling and beam broadening (see 2.2.2). The absolute HAADF- and BF-intensities are approximately linear functions of the mean

atomic number. As for the HAADF-intensity, this is well in accordance with theory considering incoherence of scattering events (see equation (2.3)). Fits of $I(d, k, \gamma_i, c_{\text{Ni}}) = d + k [c_{\text{Ni}} Z_{\text{Ni}}^{\gamma_i} + (1 - c_{\text{Ni}}) Z_{\text{Au}}^{\gamma_i}]$ or the equivalent model function $\tilde{I}(\tilde{d}, \tilde{k}, \bar{Z}) = \tilde{d} + \tilde{k} \bar{Z}$ with $\tilde{d} = \tilde{d}(d, k, \gamma_i)$, $\tilde{k} = \tilde{k}(k, \gamma_i)$ and $\bar{Z} = \bar{Z}(c_{\text{Ni}})$ are not expedient in order to quantify the Z-dependency, because the parameter γ_i cannot be computed independently from k . The slope of the first order polynomial fits is the highest for $t \approx 20$ nm, but this does not mean that the Z-contrast is best for this thickness value. The visual slope in the relative intensity-plots are the ones which directly correspond to logarithmic contrast C_{ln} according to equation (2.2). Concerning the HAADF, it is higher for thin specimens and gets monotonously lower with increasing thickness. Note that the HAADF-contrast is outstanding when compared to BF/ABF. Assuming a value of $\left| \frac{\Delta I}{I} \right| \geq 5\%$ is perceptible by the human eye, a nickel concentration of as low as $c_{\text{Ni}} \approx 0.06$ ($\bar{Z} \approx 76$) could be seen in between pure gold columns for specimens approximately 6 nm in thickness and at least $c_{\text{Ni}} \approx 0.08$ ($\bar{Z} \approx 75$) for thicknesses up to 60 nm. The BF-contrast is better for thicker than for thinner models by trend. As expected, it is much weaker than the HAADF-contrast. For thickness values less than roughly 20 nm, we would need $c_{\text{Ni}} \approx 0.5$ ($\bar{Z} \approx 54$) to be able to distinguish nickel-yielding columns from pure gold, for higher thicknesses we could see $c_{\text{Ni}} \approx 0.3$ ($\bar{Z} \approx 64$). The ABF-contrast exhibits an irregular behavior, the intensity for low mean atomic numbers is less than for higher ones at many points.

In figure 3.15, HAADF iso-intensity lines for the parameters thickness and nickel concentration are plotted. The higher the nickel concentration is, the more the gradient of the intensity with respect to thickness and nickel concentration points in the direction of changing nickel concentration. The thicker the model, the farther away from each other the iso-intensity lines are.

The interpretation of the contour plot regarding the logarithmic intensity in relation to the pure gold intensity at the same thickness, which is illustrated in figure 3.16, is anything but intuitive. The contrast quantity $\log \left[\frac{I_{\text{abs}}(c_{\text{Ni}}, t)}{I_{\text{abs}}(0, t)} \right]$ immediately corresponds to the logarithmic contrast C_{ln} according to equation (2.2). Iso-contrast lines close to each other indicate a good contrast regarding the nickel concentration. So, for a very thin model, only a few nanometers thick, concentration variations can be detected quite easily, because the distance between iso-contrast lines is short. On the other hand, it is difficult to assert an absolute nickel concentration because on a given iso-contrast line the concentration heavily depends on thickness. Note that irregularities from 4 to 6 nm represent the same effect as the presence of the kink

in the curve of HAADF-intensity versus thickness for gold columns in combination with its absence for nickel columns (see previous models, e.g. figures 3.3 and 3.7).

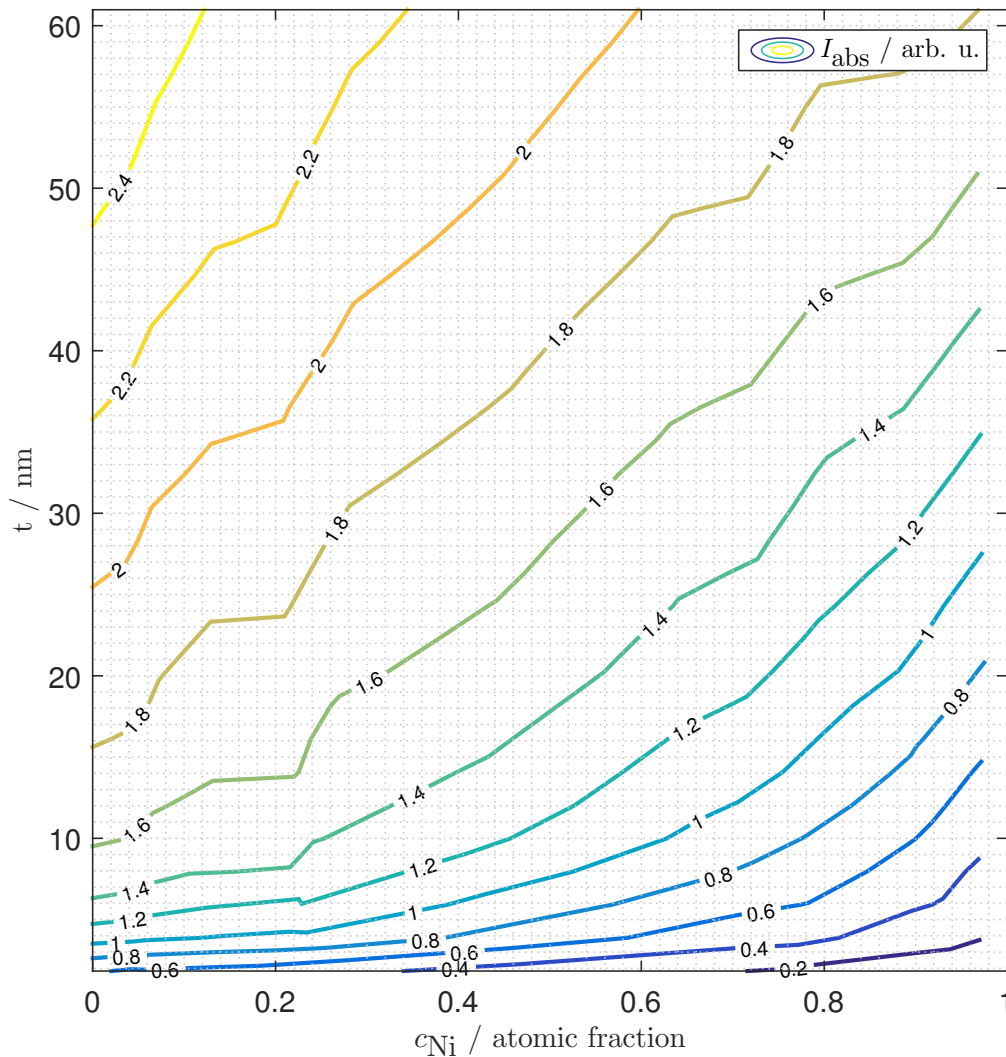


Figure 3.15.: Model 6: Iso-intensity lines for the absolute average HAADF-intensity as a function of thickness and nickel concentration; The original data points are not located on the iso-intensity lines, which are obtained by interpolation.

If we move on to higher thicknesses, the lines move farther away from each other, making concentration contrast weaker. At the latest here, if not before, it becomes clear that concentration determination of real specimens based on contrast quantification from experimental STEM images and deduction from simulation results is a really hard task. First, the iso-contrast lines are not parallel to the thickness axis,

3. Results and analysis

so the specimen thickness should be known precisely since it heavily influences the Z-contrast. Second, if we obtained a certain contrast value concerning two different atoms column or regions, we would need to know the nickel concentration in one of them in order to be able to estimate the concentration in the other, because a given value of C_{ln} (e.g. 0.2) could corresponding to any iso-contrast line pair separated by this value (e.g. -0.7 and -0.5 , -0.3 and -0.1). Therefore, approximate knowledge of the average concentration in the investigated region is mandatory if iso-contrast plots fashioned this way are used.

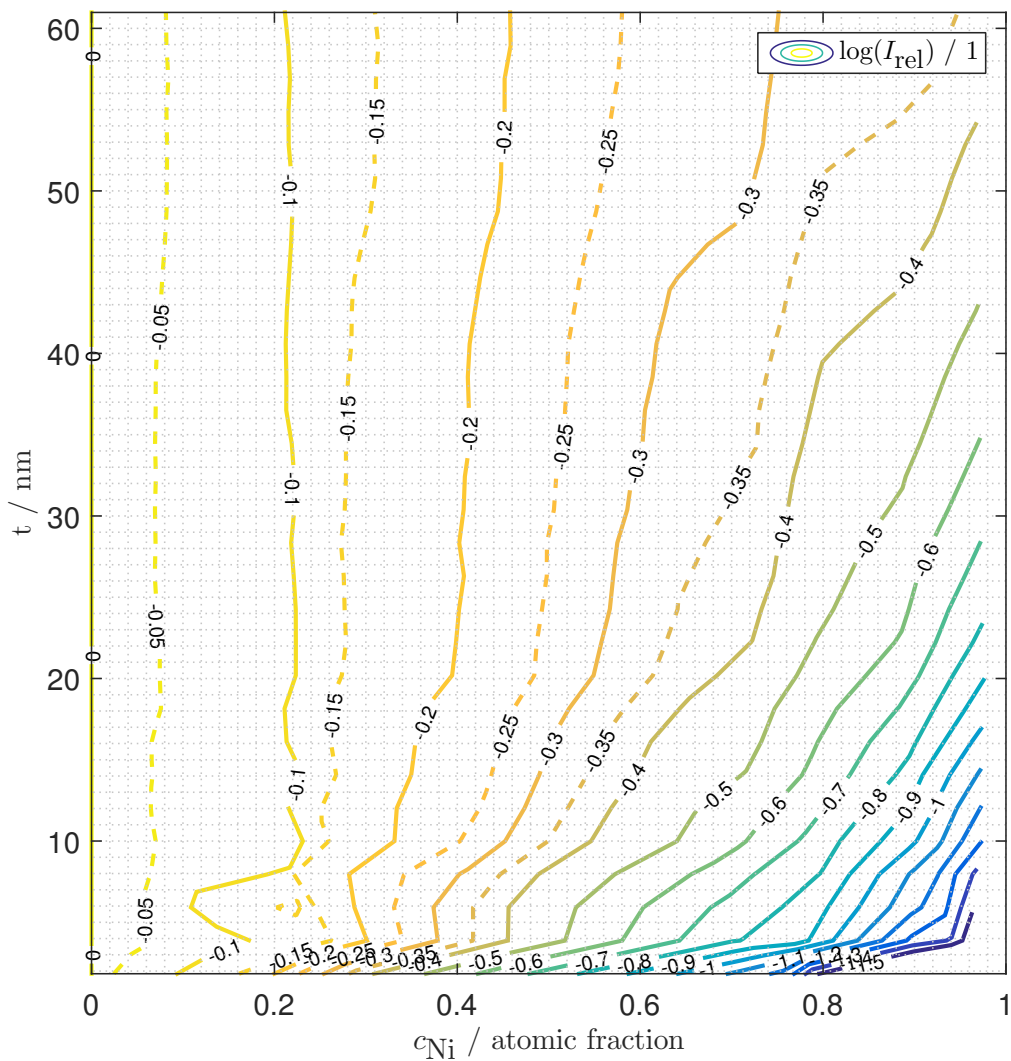


Figure 3.16.: Model 6: Iso-contrast lines for the logarithmic relative average HAADF-intensity $\log \left[\frac{I_{abs}(c_{Ni}, t)}{I_{abs}(0, t)} \right]$ as a function of thickness and nickel concentration; The lines are also obtained by interpolation of the data.

3.1.2. Lattice relaxations

The following section starts with an extensive validation of the MC relaxation program by means of a small model (256 atoms). This is necessary due to the self-made character of the code, in contrast to the MD simulation carried out with the widespread LAMMPS. Later, the results of the application to two larger models (13500 atoms) are presented.

MC method validation

In order to refine our MC binary alloy lattice relaxation code and validate its applicability, a model small enough to have the relaxation process complete thermalization within a reasonable amount of time, say half an hour at most, was used (see figure 3.17). It consisted of $4 \times 4 \times 4$ unit cells, which were arranged in a way such that p.b.c. were implementable. 81 out of 256 atoms were nickel ($c_{\text{Ni}} \approx 0.316$) and they were distributed similar to models 5 and 6: $c_{\text{Ni}}(x, y, z) = \sin^{10}\left(\frac{x}{0.907\text{nm}}\pi\right) \cdot 0.8 + 0.1$, thus we have $\max_x \left(\sum_y \sum_z c_{\text{Ni}}(x, y, z)\right) \leq 0.9$ and $\min_x \left(\sum_y \sum_z c_{\text{Ni}}(x, y, z)\right) \geq 0.1$. We were interested in the following aspects:

- Comparison of the utilized calculation of the single-atom energy E_k (see equation (2.21)) with the unabbreviated computation of the energy E (see equations (2.9) and (2.13))
- Independence of the result from the starting configuration
- Differences between RTS- and Zhou-potential

For every potential, the lattice relaxation was performed four times:

- (a) Single-atom energy computation according to equation (2.21); The starting configuration was not modified.

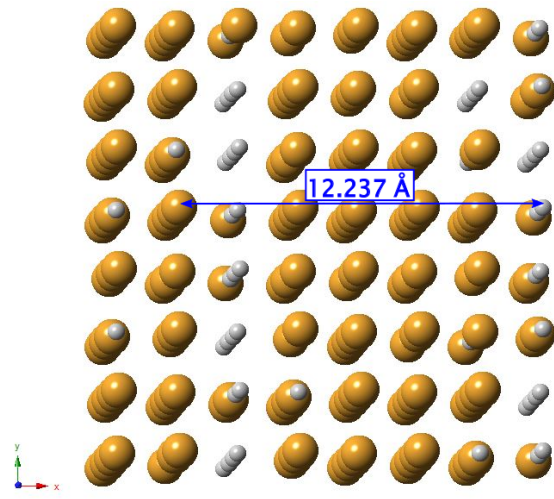
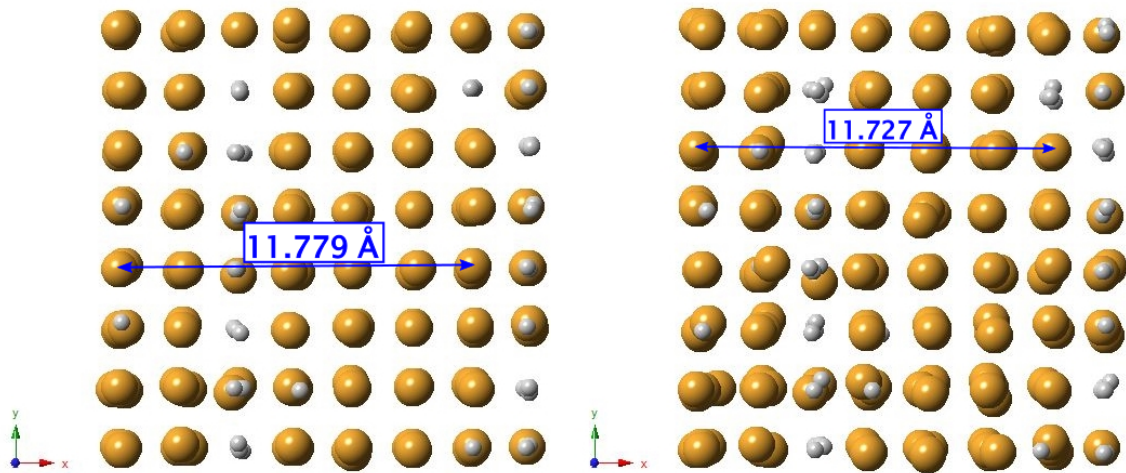


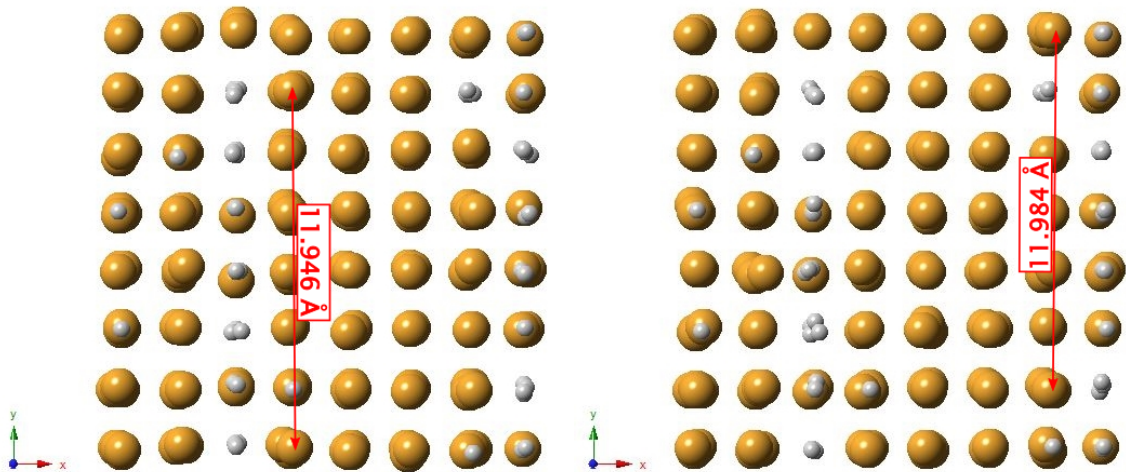
Figure 3.17.: Validation model for the MC lattice relaxation code: Inclined crack of the input with a perfect fcc lattice; The marked distance equates to three times the lattice constant.

3. Results and analysis

- (b) Total energy computation according to equation (2.9); The starting configuration was not modified.
- (c) Single-atom energy computation; The original starting coordinates were multiplied by 0.95, so the input was squeezed.
- (d) Single-atom energy computation; The original starting coordinates were randomly distorted by multiplication with a uniformly distributed factor in the range 0.975 .. 1.025.



(a) Single-atom energy calculation after $256 \cdot 10^4$ steps (b) Total energy calculation after $256 \cdot 10^4$ steps



(c) Single-atom energy calculation with squeezed input after $40 \cdot 10^4$ steps (d) Single-atom energy calculation with a randomly distorted input after $30 \cdot 10^4$ steps

Figure 3.18.: Validation model for the MC lattice relaxation code: [001] views of the outputs of the four simulation variations using the RTS-potential; The marked distances indicate the contraction in comparison to figure 3.17.

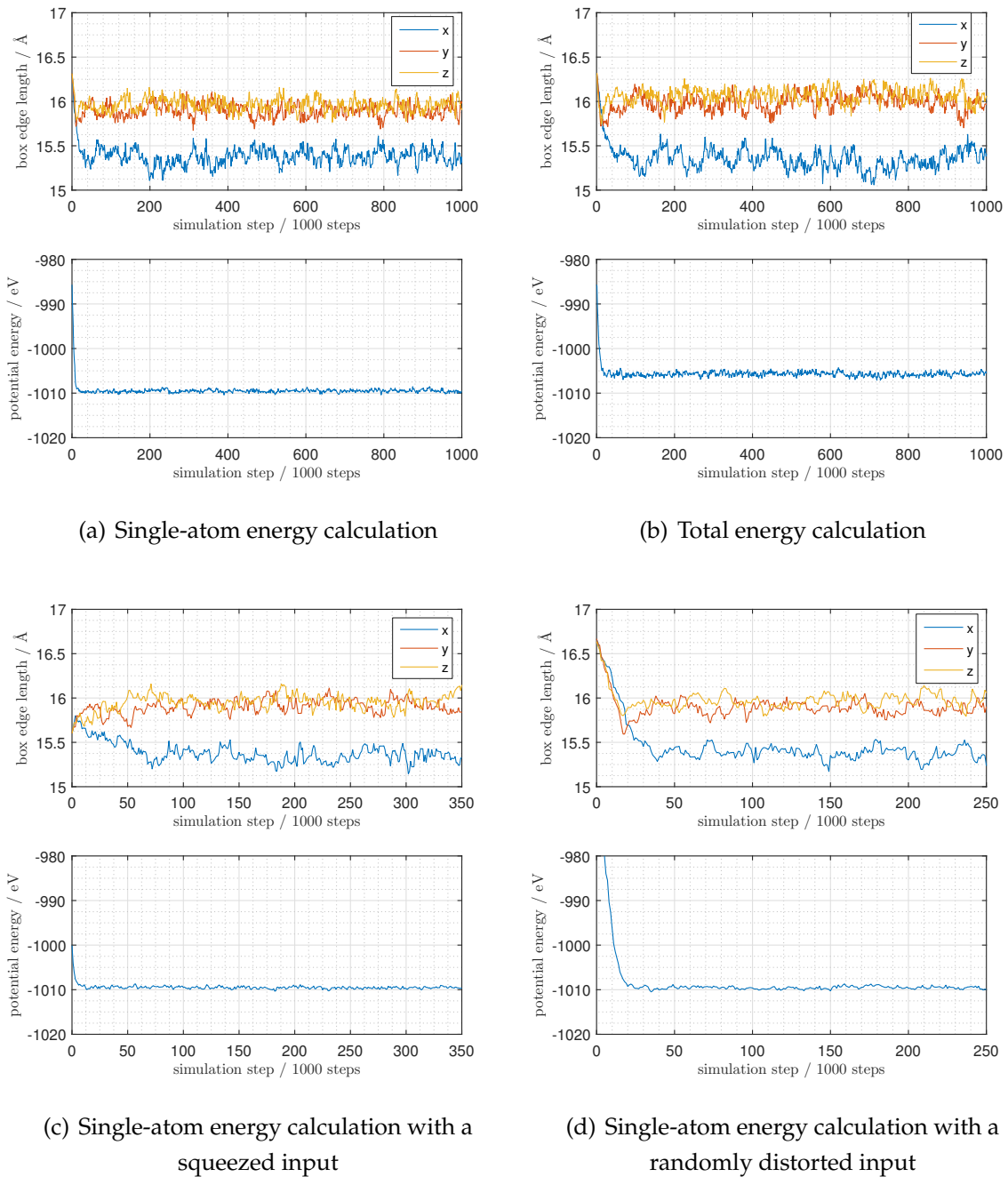


Figure 3.19.: Validation model for the MC lattice relaxation code: Time evolution of box size and total energy for the four simulation variations using the RTS-potential; Note that the individual options differ in the plotted time scale.

The results belonging to the RTS-potential are presented in detail. The applicability of the code in combination with the Zhou-potential has analogously been validated, but - in order not to overload this lateral, though very important, section - the discussion concerning it is shortened to simulation option (a). Figure 3.18, showing the

3. Results and analysis

simulation output crystals, looks very promising per se, however, the time evolution charts in figure 3.19 and table 3.2 bring some more details forward. The total energy computation yields larger box edge lengths in the y - and z -direction, leading to an average energy a few tenths of a percent higher compared to the single-atom energy computations. The reason for this result is unclear. Apart from that, the starting configuration does not affect the single-atom energy simulations as long as the crystal distortions remain within reasonable boundaries.

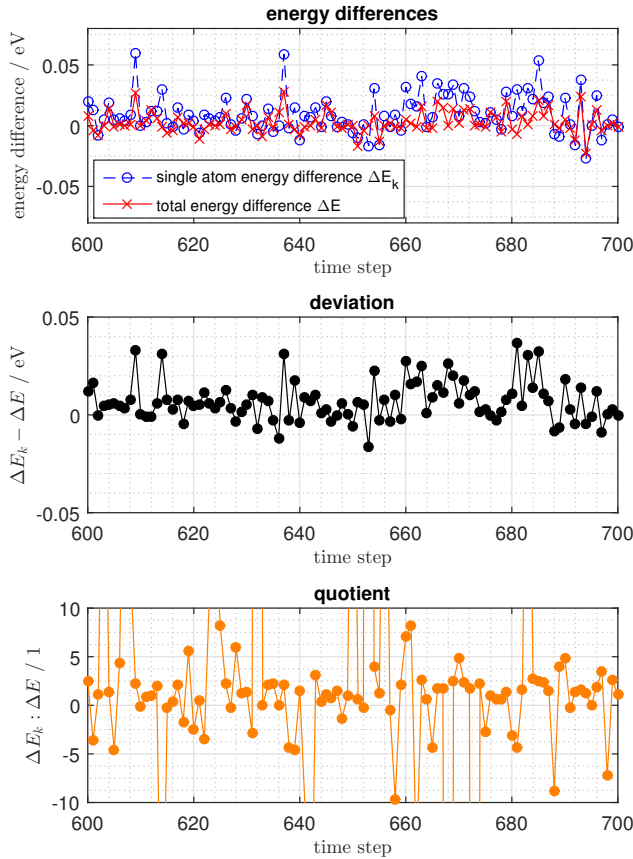


Figure 3.20.: Validation model for the MC lattice relaxation code: Analysis of the systematic error due to the usage of the single-atom energy E_k analysis yielded:

- The proportion of correct accept/reject-decisions was $\approx 81.5\%$. A correct decision is performed if both $\exp\left(\frac{-\Delta E}{k_B T}\right)$ and $\exp\left(\frac{-\Delta E_k}{k_B T}\right)$ are either (A) greater than or (B) less than or equal to a given random number r .
- The fraction of non-negative ΔE_k was $\approx 74.8\%$.

After asserting that our simplified energy calculation works at least "pretty fine", we had to further investigate the systematic error we are consciously committing. Therefore we put the thermalized result of the single-atom energy computation (case (a): unmodified starting configuration) into a slightly altered simulation in which we calculated both ΔE according to equations (2.9) and (2.20) and ΔE_k as per equations (2.21) and (2.22). The accept/reject-decision was processed with ΔE_k . Figure 3.20 shows the differences ΔE and ΔE_k as well as the deviation and the quotient of these in a 100-step-extract of the 10^5 simulation steps in total. Simple data

- The fraction of non-negative ΔE was $\approx 71.5\%$.
- ΔE and ΔE_k had the same sign in $\approx 86.9\%$ of all cases. A value that high indicates that the single-atom energy approximation correlates strongly with the total energy.
- Concerning the quantity $\delta := \Delta E_k - \Delta E$:
 - $\delta \geq 0 \Leftrightarrow \Delta E_k \geq \Delta E$ in $\approx 72.6\%$ of all cases. One effect is that the simulation can get stuck in local minima more easily.
 - $\bar{\delta} = 14.9(1)$ meV, whereby the given uncertainty corresponds to the standard error of the sample mean. This value is not low compared to $k_B T \approx 25.3$ meV for $T = 293.15$ K, which argues against the simplification.

As for the Zhou-potential, the total energy is a few percent lower than calculated from the RTS-potential. We notice that the thermal motion of the atoms is more unrestricted in comparison to the RTS-simulation, since the post-thermalization fluctuation range for box size as well as for energy is about three times larger (see time evolutions in figure 3.21 and table 3.2).

To round the inspection up, histograms of the nearest neighbor distances are plotted in figure 3.22. Au-Ni and Ni-Ni distances are significantly lower than the Au-Au distances.

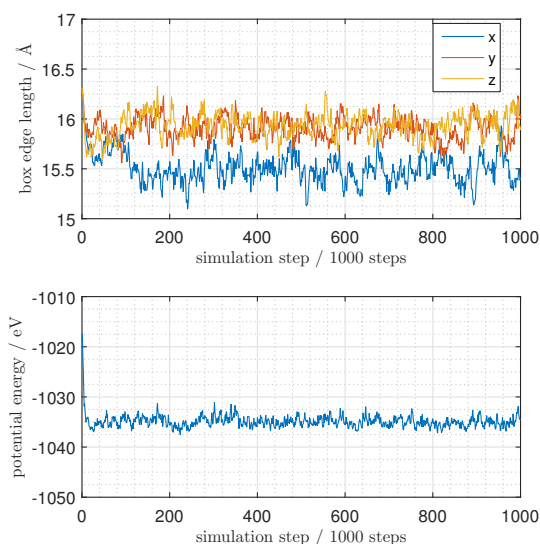


Figure 3.21.: Validation model for the MC lattice relaxation code: Time evolution of box size and total energy for single-atom energy calculation using the Zhou-potential

3. Results and analysis

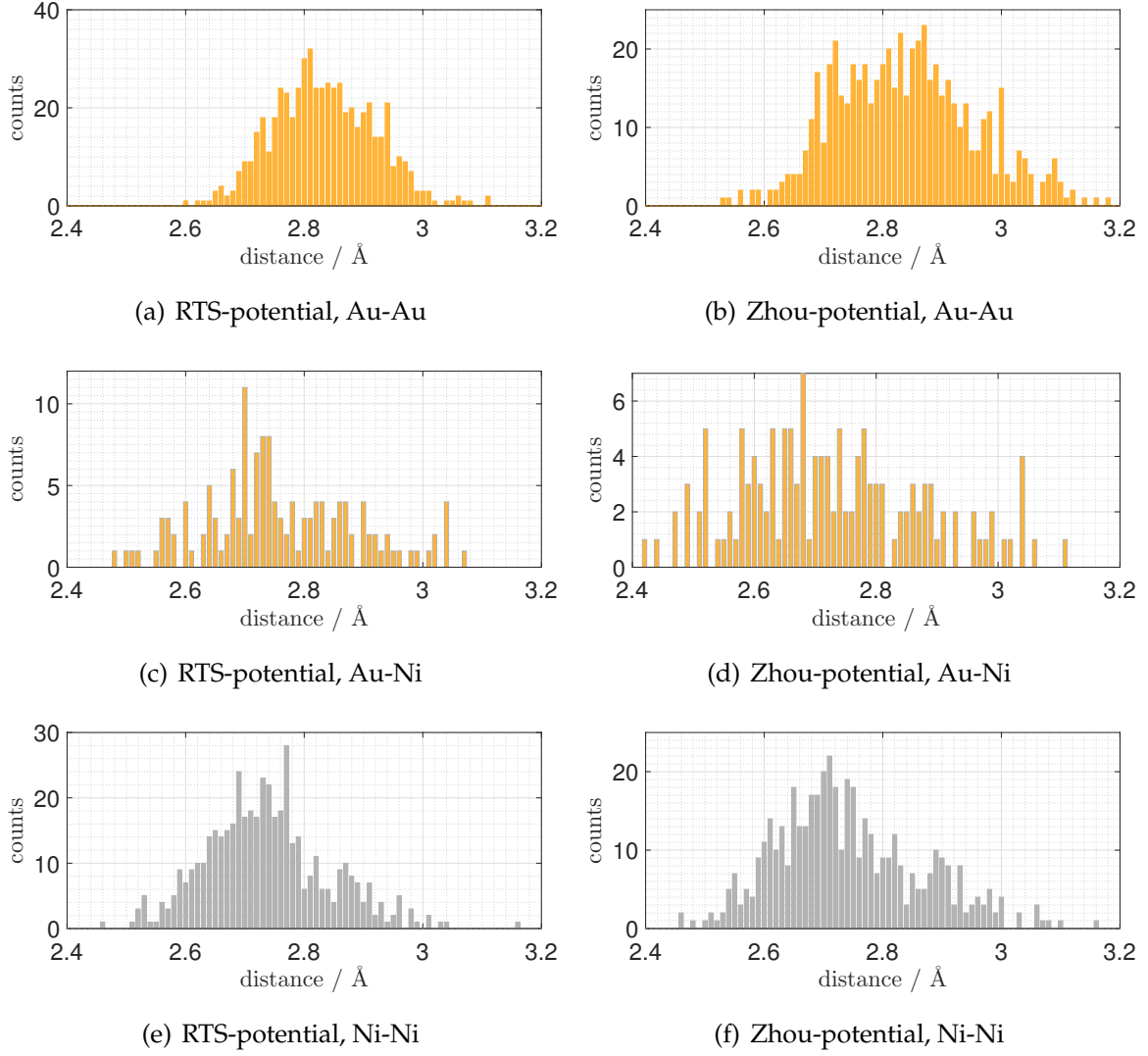


Figure 3.22.: Validation model for the MC lattice relaxation code: Histograms of nearest neighbor distances for single-atom energy calculation outputs; The equilibrium values are $a_{\text{Au}} \cdot \sqrt{2}/2 \approx 2.885 \text{ \AA}$ for gold and $a_{\text{Au}} \cdot \sqrt{2}/2 \approx 2.494 \text{ \AA}$ for nickel.

Table 3.2.: Various data values concerning the MC relaxation validation simulations

		t_{tot}	total computation time for 10000 steps per atom					
		N_{th}	thermalization length (approximated from the time series)					
		\bar{E}	average energy (after thermalization)					
		$\tau_{\text{int}}(E)$	integrated autocorrelation time regarding the energy time series					
		$\bar{x}, \bar{y}, \bar{z}$	average box length in x -, y -, z -direction					
potential	simulation option	$t_{\text{tot}} / \text{h}$	$N_{\text{th}} / \text{MC steps}$	\bar{E} / eV	$\tau_{\text{int}}(E) / \text{steps}$	$\bar{x} / \text{\AA}$	$\bar{y} / \text{\AA}$	$\bar{z} / \text{\AA}$
RTS	(a)	0.8	$1 \cdot 10^5$	-1009.5 ± 0.7	≈ 4000	15.38	15.90	15.96
RTS	(b)	44	$1 \cdot 10^5$	-1005.8 ± 1.0	≈ 4000	15.35	15.99	16.07
RTS	(c)	[n.c.*]	$1 \cdot 10^5$	$-1009.6 \pm 1.4^{**}$	$\approx 3000^{**}$	15.36	15.91	15.97
RTS	(d)	[n.c.*]	$5 \cdot 10^4$	$-1010 \pm 3^{**}$	$\approx 6000^{**}$	15.38	15.89	15.98
Zhou	(a)	1.1	$1 \cdot 10^5$	-1035 ± 3	≈ 5000	15.51	15.91	15.92

* not completed

** simulation length too short for a well-founded indication

Model 7: Sine¹⁰-shaped nickel concentration modulation (wavelength of 0.907 nm)

The model had 13500 atoms and $c_{\text{Ni}}(x, y, z) = \sin^{10}\left(\frac{x}{0.907\text{nm}}\pi\right) \cdot 0.8 + 0.1$ (see figure 3.23), with a total nickel concentration of ≈ 0.304 .

Lattice relaxation

The time evolution of energy and the model edge lengths in the MC simulations are depicted in figure 3.24.

Using the RTS-potential, the thermalization of the crystal took about 4 million Monte Carlo steps in total (see time evolution in figure 3.24(a)), which is just under 300 steps per atom. The total energy averages out at $\bar{E}/N = -3.96295(5)$ eV

per atom, the box dimensions at $x_1 \times x_2 \times x_3 = 57.45(3) \times 59.94(3) \times 59.92(2)$ Å³. As for the integrated autocorrelation time regarding the energy time series, we obtain $\tau_{\text{int}}(E) \approx 2 \cdot 10^5$. The autocorrelation time $\tau_{\text{int}}(x_i)$ is in the range of $5 \cdot 10^6$. Thus, the simulation length was too short in order to provide reliable data here.

There were about 3 million thermalization steps needed in total (≈ 225 per atom) with the Zhou-potential. The time evolution of the simulation is illustrated in figure 3.24(b). The total energy averages out at $\bar{E}/N = -4.0467(7)$ eV per atom, the box dimensions at $x_1 \times x_2 \times x_3 = 58.09(7) \times 59.82(5) \times 59.89(6)$ Å³. Furthermore, we have $\tau_{\text{int}}(E) \approx 2.5 \cdot 10^5$ for the energy time series and $\tau_{\text{int}}(x_i) \approx 5 \cdot 10^6$ regarding the box edge length again.

As for the Zhou-MD simulation, we used the output of the RTS-MC computation, averaged over the time series excluding thermalization. The potential energy averages out at $\bar{E}/N \approx -3.96$ eV per atom. The box dimension can be indicated as $x_1 \times x_2 \times x_3 \approx 56.6 \times 63.7 \times 62.8$ Å³, but these values do not specify the result well, because the model differs greatly from a cuboid.

The output crystals after all three relaxation methods are illustrated in figure 3.25. The MC-outputs are time averaged after equilibration, however, the MD-output is a snap-shot at the simulation's end, because the computation of the average has not been caught up. Looking at the MD-output (figure 3.25(c)), we recognize displacements of atoms as well as crystal bendings that are presumptively too severe to ac-

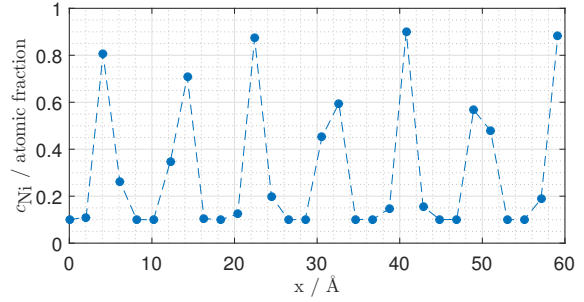


Figure 3.23.: Model 7: Nickel concentration modulation in x-direction

3. Results and analysis

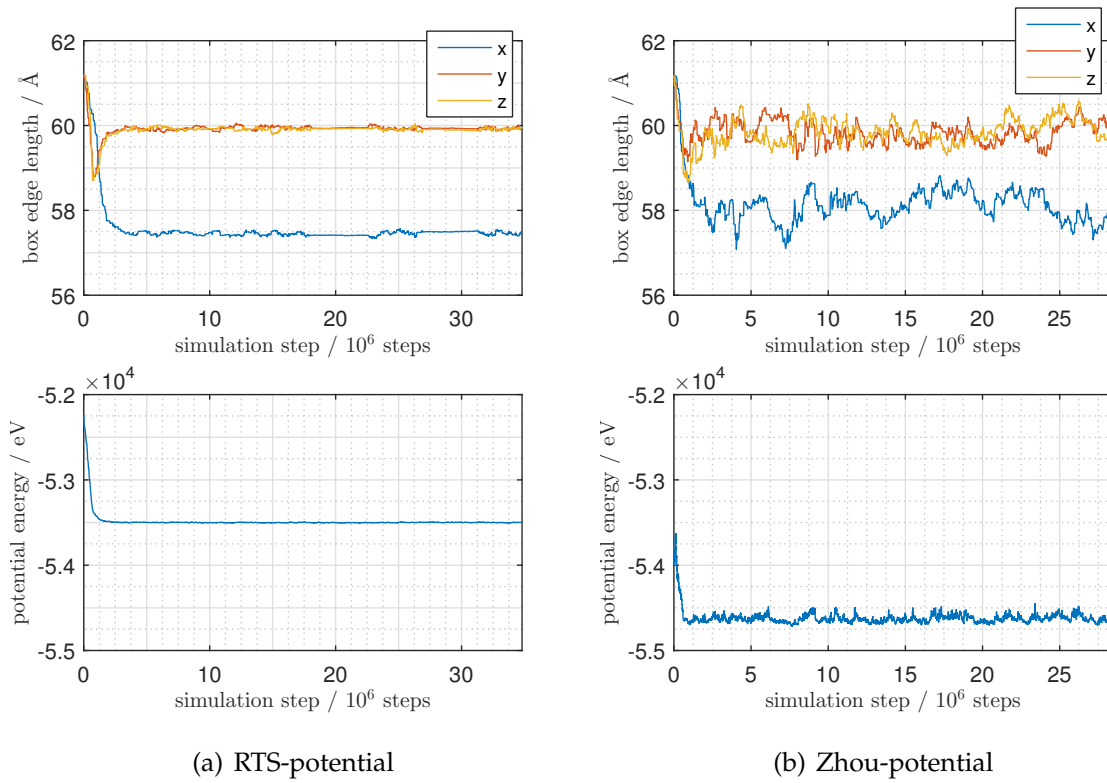
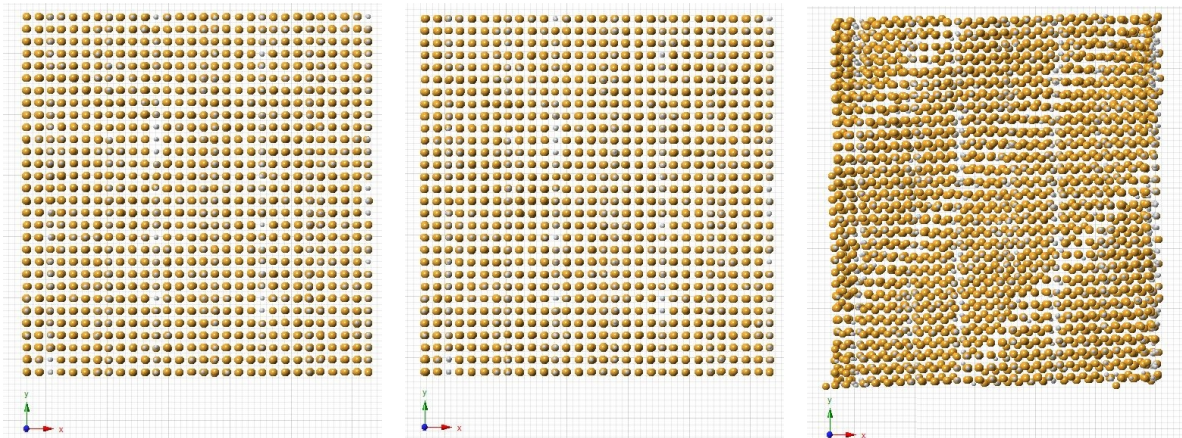


Figure 3.24.: Model 7: Monte Carlo time evolution of box size and total energy

tually appear in a real crystalline bulk material without the presence of dislocations (no proof by calculation of mechanical stresses). It seems very likely that the consideration of p.b.c. along with the cuboid-shaped box of the model cause this simulation behavior. In addition, we find irregularities in the $[1\bar{1}0]$ -direction which cannot be explained. Most likely, the feature is another computational artifact.



(a) MC-relaxed, RTS-potential (b) MC-relaxed, Zhou-potential (c) MD-relaxed, Zhou-potential

Figure 3.25.: Model 7: Views of the crystal in the $[001]$ zone axis after different relaxation simulations; The grid size is $1 \text{ \AA} \times 1 \text{ \AA}$.

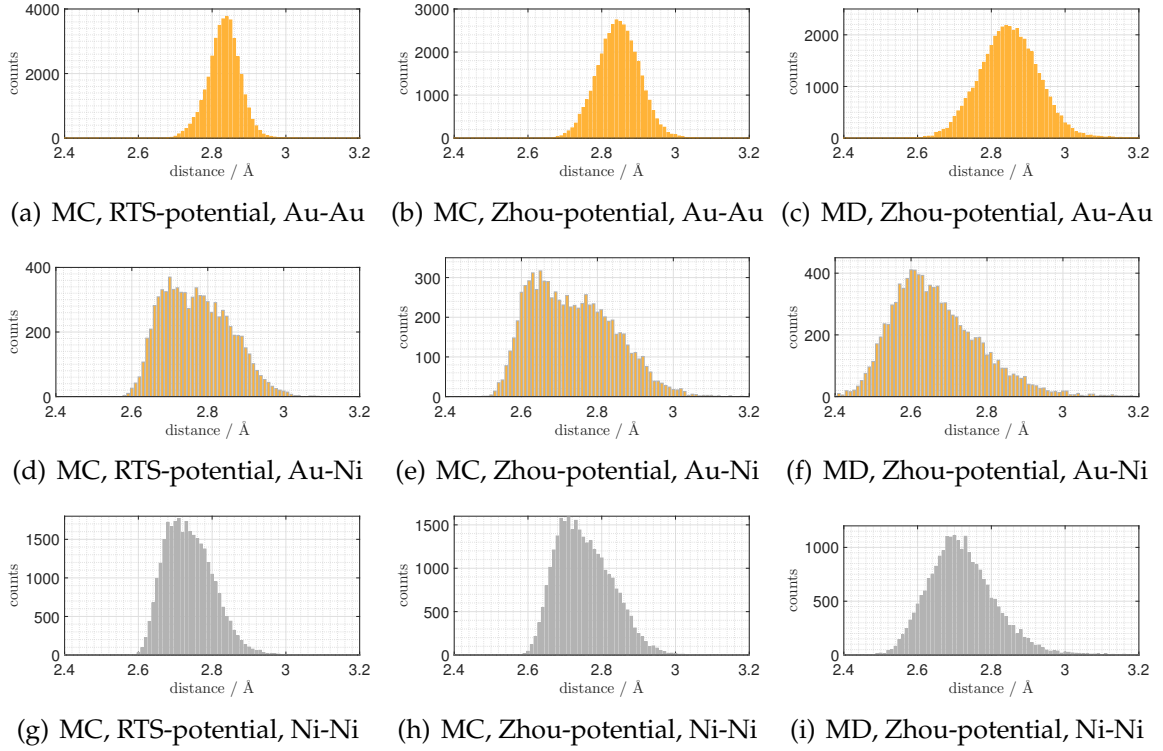


Figure 3.26.: Model 7: Histograms of nearest neighbor distances for MC and MD simulation outputs; The equilibrium values are $a_{\text{Au}} \cdot \sqrt{2}/2 \approx 2.885 \text{ \AA}$ for gold and $a_{\text{Ni}} \cdot \sqrt{2}/2 \approx 2.494 \text{ \AA}$ for nickel.

Table 3.3.: Model 7: Statistical key data of the crystal after lattice relaxation

\tilde{r}	median
\bar{r}	sample mean
s^2	sample variance
c_v	sample coefficient of variation
v	sample skewness
μ_{gf}	mean of Gaussian fit (uncertainty corresponds to the 95% confidence bounds)
σ_{gf}^2	variance of Gaussian fit (uncertainty corresponds to the 95% confidence bounds)

Relaxation method	Bonding atoms	$\tilde{r}/\text{\AA}$	$\bar{r}/\text{\AA}$	$s^2/\text{\AA}^2$	c_v	v	$\mu_{\text{gf}}/\text{\AA}$	$\sigma_{\text{gf}}^2/\text{\AA}^2$
MC (RTS-potential)	Au-Au	2.8335	2.8321	0.0019	0.0153	-0.0861	2.834(1)	0.00165(5)
	Au-Ni	2.7641	2.7706	0.0076	0.0315	0.3529	2.760(5)	0.0093(9)
	Ni-Ni	2.7321	2.7380	0.0041	0.0235	0.5263	2.729(2)	0.0044(3)
MC (Zhou-potential)	Au-Au	2.8450	2.8450	0.0032	0.0198	0.0393	2.845(1)	0.00319(3)
	Au-Ni	2.7229	2.7345	0.0118	0.0397	0.4512	2.718(7)	0.014(2)
	Ni-Ni	2.7444	2.7531	0.0055	0.0269	0.4948	2.741(3)	0.0059(5)
MD (Zhou-potential)	Au-Au	2.8446	2.8463	0.0052	0.0252	0.3891	2.843(1)	0.00452(7)
	Au-Ni	2.7163	2.7377	0.0206	0.0524	0.5221	2.710(9)	0.022(3)
	Ni-Ni	2.7260	2.7358	0.0091	0.0349	0.6669	2.722(3)	0.0083(5)

The nearest neighbor distances are graphed in figure 3.26. Some statistical key values can be found in table 3.3. For the Zhou-MC simulation, it is quite interesting that the mean distance between gold and nickel is lower than between nickel and nickel. This coheres with the nature of the nickel impurities, i.e. many atoms in a plane. Say we have a nickel-rich plane perpendicular to the x -direction and surrounded by parallel nickel-poor planes. Then the planes come closer to each other because the Au-Ni potential minima are at shorter distances than the minima for Au-Au bonds. On the other hand, the nickel atoms cannot move closer together in the y - and z -direction due to restoring forces arising from atoms in the neighboring planes and the p.b.c.

Model 8: Nickel concentration modulation in x -direction and a single (010) lattice plane

The model had 13500 atoms and it features nickel substituents as follows:

- $c_{\text{Ni}}(x, y, z) = \sin^2\left(\frac{x}{0.907\text{nm}}\pi\right) \cdot 0.4 + 0.3$ for $x \leq 13a_{\text{Au}}$ and $y \leq 0.5x + 5a_{\text{Au}}$, in which the nickel atoms are randomly distributed in y - and z -direction.
- In addition, a single (010) lattice plane with $c_{\text{Ni}} = 0.7$ at $y = 23\frac{a_{\text{Au}}}{2}$ was replaced.
- The total concentration of nickel was ≈ 0.282 .

Figure 3.27(a) clarifies how the model was designed. In terms of the nickel-yielding planes, the drawing has a nickel concentration of up to 1 and, thus, is not identical to the used model. Anyhow, the graphical representation depicts the special properties of this model clearer.

Lattice relaxation

The outputs are illustrated in the figures 3.27(b), 3.27(c) and 3.27(d).

There were about 13 million Monte Carlo steps needed for thermalization with the RTS-potential (see time evolution in figure 3.28(a)), which is ≈ 960 steps per atom.

- Total energy:
 $\bar{E}/N = -3.93081(5)$ eV per atom, $\tau_{\text{int}}(E) \approx 250$
- Box dimensions:
 $x_1 \times x_2 \times x_3 = 59.35(2) \times 58.61(3) \times 60.13(3)$ Å³, $\tau_{\text{int}}(x_i) \approx 5 \cdot 10^6$

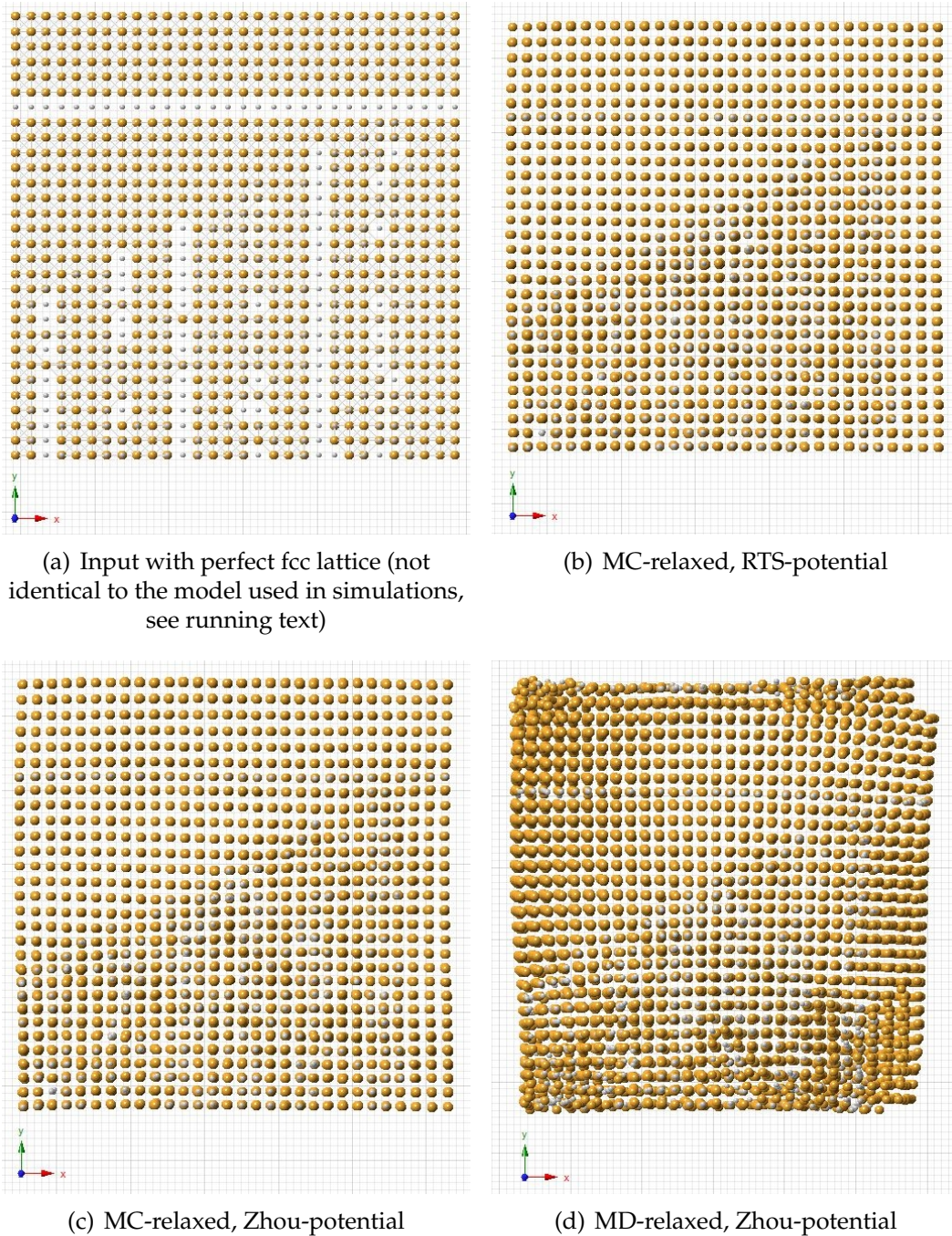


Figure 3.27.: Model 8: Views of the crystal in the [001] zone axis before and after the relaxation simulations; The grid size is $1 \text{ \AA} \times 1 \text{ \AA}$.

3. Results and analysis

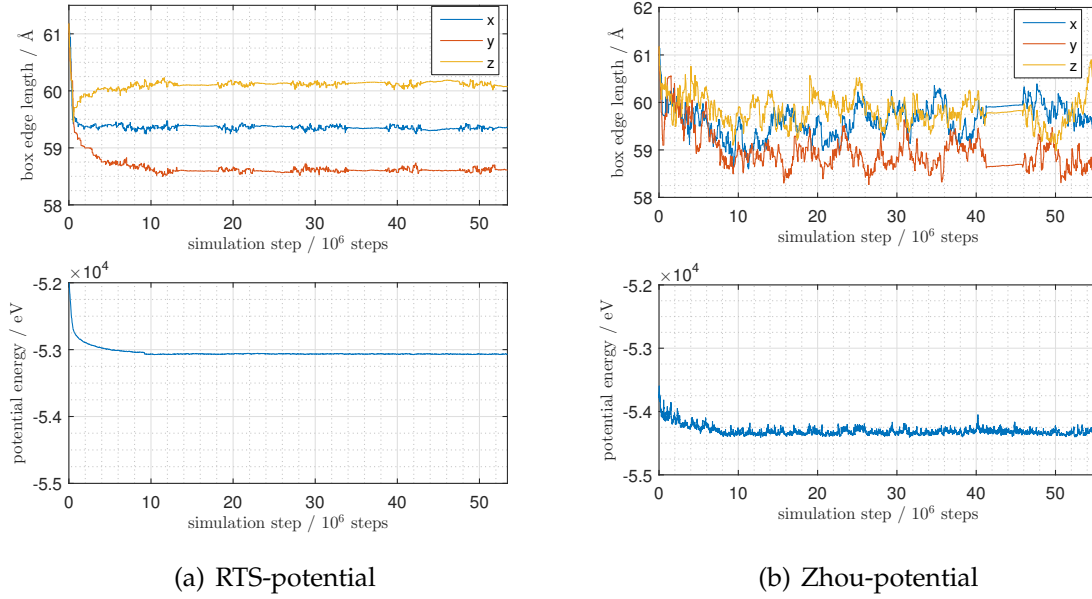


Figure 3.28.: Model 8: Monte Carlo time evolution of box size and total energy

Using the Zhou-potential, the thermalization of the crystal took about 10 million steps in total (≈ 740 per atom). The time evolution is illustrated in figure 3.28(b).

- Total energy:

$$\bar{E}/N = -4.0242(5) \text{ eV per atom}, \tau_{\text{int}}(E) \approx 200$$

- Box dimensions:

$$x_1 \times x_2 \times x_3 = 59.7(2) \times 58.8(2) \times 59.8(2) \text{ \AA}^3, \tau_{\text{int}}(x_i) \approx 5 \cdot 10^6$$

The Zhou-MD simulation yields an average potential energy after equilibration of $\bar{E}/N \approx 3.83$ eV per atom. It distorted the shape of the initial cube strongly, just as we noticed for model 7, so that the box dimension can only roughly be stated as $59..63 \times 62..64 \times 66..68 \text{ \AA}^3$.

The statistical key values for the nearest neighbor distances can be found in table 3.4. Just as we determined for the previous model, the relaxations, especially the ones using the Zhou-potential, lead to lower gold-nickel distances when compared to nickel-nickel.

Table 3.4.: Model 8: Statistical key data of the crystal after lattice relaxation

\tilde{r} median
 \bar{r} sample mean
 s^2 sample variance
 c_v sample coefficient of variation
 v sample skewness
 μ_{gf} mean of Gaussian fit (uncertainty corresponds to the 95 % confidence bounds)
 σ_{gf}^2 variance of Gaussian fit (uncertainty corresponds to the 95 % confidence bounds)

Relaxation method	Bonding atoms	$\tilde{r}/\text{\AA}$	$\bar{r}/\text{\AA}$	$s^2/\text{\AA}^2$	c_v	v	$\mu_{\text{gf}}/\text{\AA}$	$\sigma_{\text{gf}}^2/\text{\AA}^2$
MC (RTS-potential)	Au-Au	2.8422	2.8404	0.0022	0.0165	-0.0554	2.844(1)	0.00198(9)
	Au-Ni	2.7362	2.7440	0.0066	0.0296	0.5021	2.733(2)	0.0063(2)
	Ni-Ni	2.7376	2.7447	0.0042	0.0237	0.7172	2.735(1)	0.0035(2)
MC (Zhou-potential)	Au-Au	2.8621	2.8607	0.0056	0.0262	-0.0563	2.863(3)	0.0065(4)
	Au-Ni	2.6739	2.6906	0.0114	0.0397	0.8530	2.666(4)	0.0093(8)
	Ni-Ni	2.7369	2.7471	0.0070	0.0304	0.7695	2.732(2)	0.0057(3)
MD (Zhou-potential)	Au-Au	2.8475	2.8484	0.0064	0.0281	0.1272	2.848(1)	0.00620(9)
	Au-Ni	2.6490	2.6663	0.0132	0.0431	0.7846	2.641(4)	0.0109(9)
	Ni-Ni	2.7123	2.7204	0.0084	0.0336	0.6645	2.709(2)	0.0071(3)

3.1.3. QSTEM images of relaxed models

After the relaxed crystals had been obtained, the results were handed over to QSTEM and DF- as well as BF-images were produced.

It should be anticipated that in section 3.2, which deals with experimental results, we will see that the images obtained from MC relaxations are quite good matches for some regions in experimental images. The contrast patterns look qualitatively very similar. Furthermore, the applicability of this particular MD simulation on both models has to be scrutinized.

Model 7

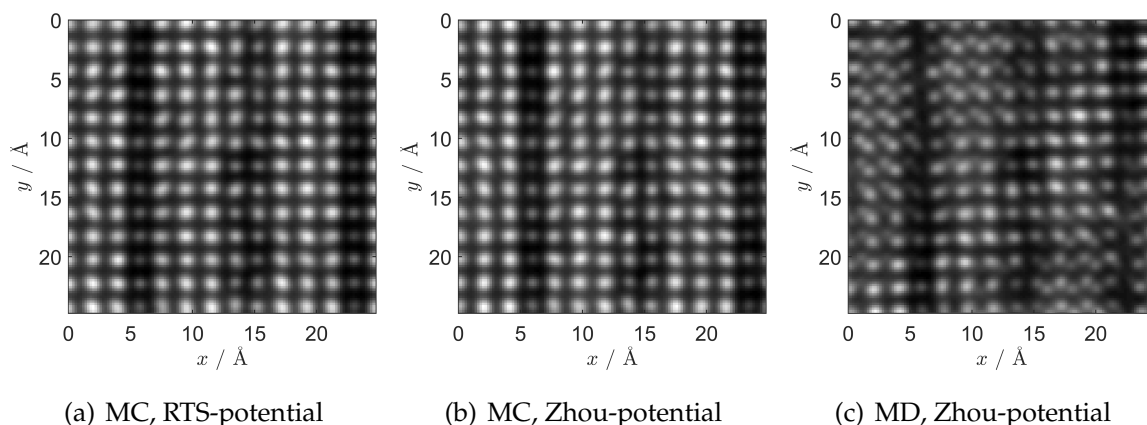


Figure 3.29.: Model 7: QSTEM HAADF images of MC- and MD-relaxed models, $t \approx 22.4 \text{ \AA}$, $\alpha = 19.6 \text{ mrad}$

Figure 3.29 shows QSTEM HAADF images of the relaxed model 7. We notice some differences between the relaxation methods, which we partially recognized while inspecting figure 3.25. Firstly, in contrast to the MC-results, the atom columns are not well aligned in the MD-outputs. The image of the MD-relaxed model exhibits a bright stripe in positive x - and negative y -direction, which is a few \AA in width. Small tilts lead to no better images, because the displacement of the atoms is random in all directions such that an exact alignment is not possible. Secondly, the MC relaxation using the Zhou-potential appears slightly more blurred when compared to the RTS-potential.

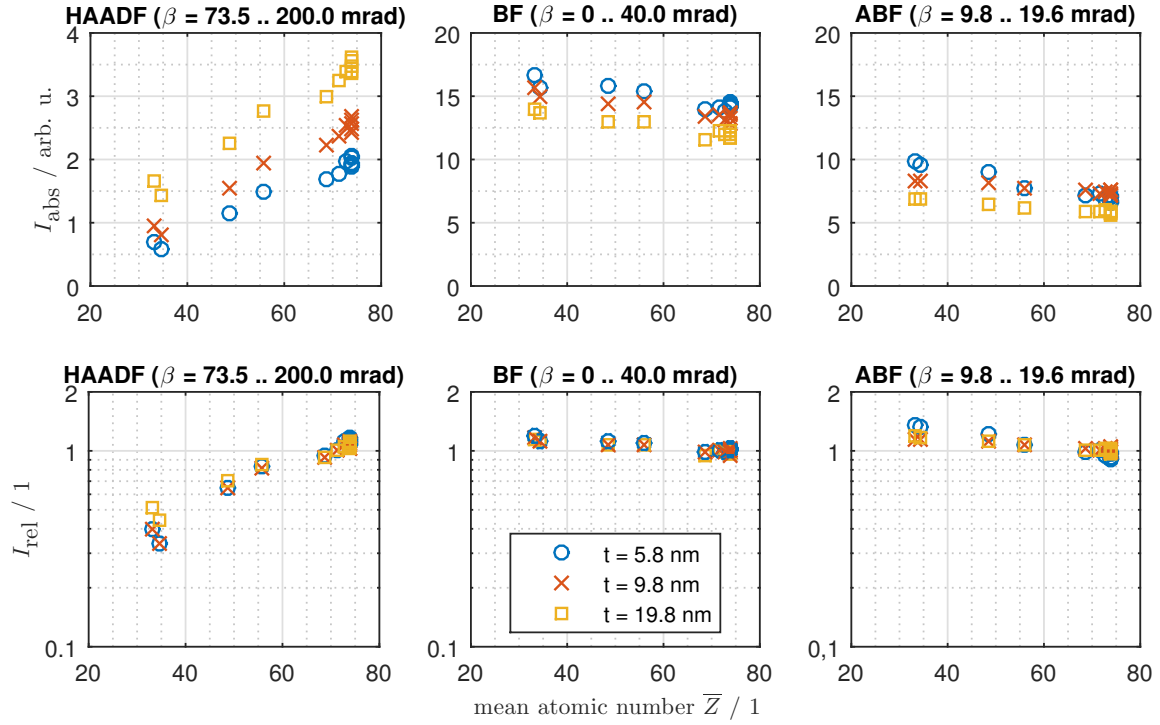


Figure 3.30.: Model 7 (MC-relaxed, RTS-potential): Absolute and relative HAADF-, BF-, and ABF-intensity vs. mean atomic number for different thicknesses; Here, the relative intensity is $I_{\text{rel}} := \frac{I_{\text{abs}}(\bar{Z})}{I_{\text{abs}}(73.9)} \Big|_t$.

Figure 3.30 contains the analysis results regarding the RTS-MC-relaxed model 7. The upper row of graphs depicts absolute HAADF-, BF-, and ABF-intensities versus mean atomic numbers for different thicknesses. In the lower row of graphs, the ratios of the absolute intensities (for varying \bar{Z}) with respect to the absolute intensity for $\bar{Z} = 73.9$ ($c_{\text{Ni}} = 0.9$) are plotted. The distribution of the nickel concentration values is not as uniform as it was in the scanning window for model 6. Similar trends as in figure 3.14 can be observed, but a detailed comparison is not possible due to the dissimilarity of the models. In addition, the systematic error of the method how the intensity values are obtained rises for blurred, rotationally non-symmetric peaks and/or double peaks, because the greyscale values within a circle around a given peak are averaged. This error leads to a non-monotonous behavior of the intensities with respect to the mean atomic number. On these grounds, the available data is not sufficient for meaningful iso-intensity/-contrast plots either. The consistency of the data gets even worse for the other relaxation methods.

Model 8

Figure 3.31 illustrates QSTEM HAADF images of the relaxed model 8. One can identify distinctive distortions in all three images. In the micrograph of the MD-relaxed model (see figure 3.31(c)), surprisingly, the atom columns in z -direction are better aligned when compared to the MD-relaxed model 7 (see figure 3.29(c)). Anyway, this fact does not approve the validity of the MD-results. We can identify distinct bending of the atom columns in the x - and y -direction, especially in the upper right part of the image. The magnitude of the bending is a few degrees per nanometer, which perhaps is unrealistically high.

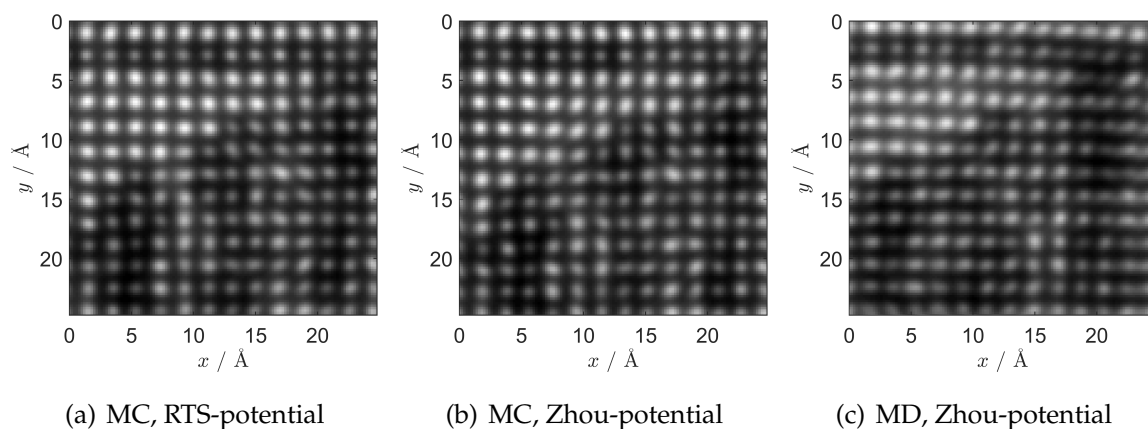


Figure 3.31.: Model 8: QSTEM HAADF images of the MC- and MD-relaxed models, $t \approx 22.4 \text{ \AA}$, $\alpha = 19.6 \text{ mrad}$

3.1.4. QSTEM CBED images with small convergence angle

To top off the simulation activity, some coherent CBED simulations in the [001] zone axis were produced. Using a very small convergence angle (0.01 mrad), the goal was to approximate SAED recordings like the ones presented before in figure 2.4 (section 2.1) or later in figure 3.49 (section 3.2.2).

It was quite tricky to find out the optimal parameters for this purpose. It turned out that in order to obtain patterns with distinct reflection spots, the model should not be thicker than a few nanometers. Furthermore, it was necessary to periodically repeat the models 7 and 8 along the x - and the y -direction, because the originals had a cross section of about $60 \times 60 \text{ \AA}^2$, which is too small to obtain feasible diffraction patterns. In the end, the following settings were used:

- Convergence angle: 0.01 mrad
- Probe array: 600 pixels x 600 pixels
- Window size: $230 \times 230 \text{ \AA}^2$, leading to a resolution in q -space of $\approx 0.0043 \text{ \AA}^{-1}$
- No TDS runs
- Any other setting was identical to the STEM simulations (see section 3.1).

By means of the chosen succession in the presentation of the CBED images the formation of the [001] diffraction pattern of a spinodally decomposed Au-Ni alloy becomes comprehensible. Just as before, when dealing with QSTEM images in real space, the models get more and more complex in terms of the nickel impurities in the gold matrix.

Figure 3.32 shows two CBED image, one of model 1, which is a pure gold crystal, and one of model 4a, in which every fourth plane perpendicular to the [100] direction is pure nickel. Looking at the pattern of model 1, we can identify the following diffraction spot "groups":

- (1) $200, 220, 020, \bar{2}20, \dots$
- (2) $110, \bar{1}10, \dots$
- (3) $310, 130, \dots$

An inspection of the reflections yielded $G_{200} = 0.491(4) \text{ \AA}^{-1}$, corresponding to $d_{200} = 2.04(2) \text{ \AA}$, which is a good approximation for the half of the model lattice constant $a_{\text{Au,model}}/2 = 2.03947 \text{ \AA}$. The pattern of the unrelaxed model 4a features

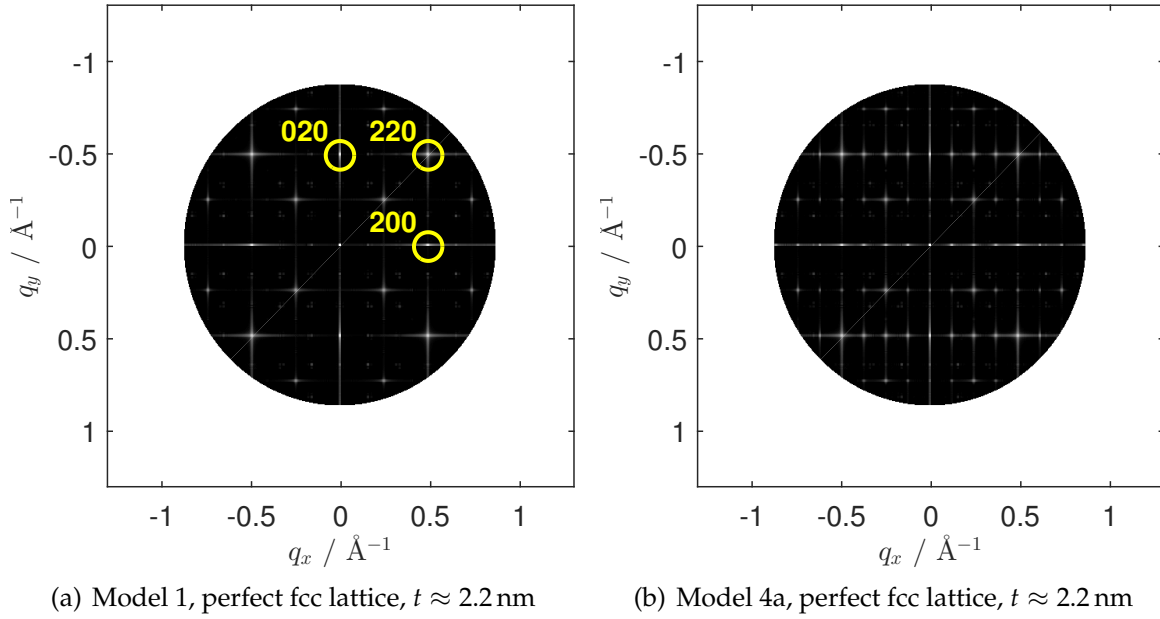


Figure 3.32.: QSTEM coherent CBED images of the unrelaxed models 1 and 4 in the [001] zone axis

distinct satellites next to all the fundamental reflections mentioned above. The distance of the satellites from the fundamental spots is $q = 0.122(4) \text{ \AA}^{-1}$, which corresponds to a nickel concentration modulation wavelength of $\lambda = 8.2(3) \text{ \AA}$. The actual value is $2 \cdot a_{\text{Au,model}} = 8.15788 \text{ \AA}$.

In figure 3.33, CBED images for the unrelaxed as well as an Zhou-MC-relaxed version of model 7, which has a sine¹⁰-modulation of the nickel concentration along the [100] direction with a wavelength of $\lambda = 9.07 \text{ \AA}$, are depicted. The fundamental spot group (1) and the associated satellites become less distinctive, because weak intensities occur almost everywhere between these spots. After relaxation, they get more diffuse. The spot groups (2) and (3) can hardly be seen in the patterns, especially spot group (2) in the one belonging to the relaxed model. This is not associated with the increase in thickness compared to models 1 and 4 (not demonstrated by additional figures here).

As for model 8 (see figure 3.34), which has a sine²-modulation along the [100] direction and one Ni plane perpendicular to [010], all the spots are more diffuse in comparison to model 7. In the CBED image of the relaxed model the spot group (2) completely disappears. The spot group (1) and their satellites become even more diffuse and are almost smelted with each other.

In anticipation of the SAED recording in the experimental section 3.2 note that the

CBED image in figure 3.34(b) is not an exact match of the experiment by any means, but it is not a bad counterpart.

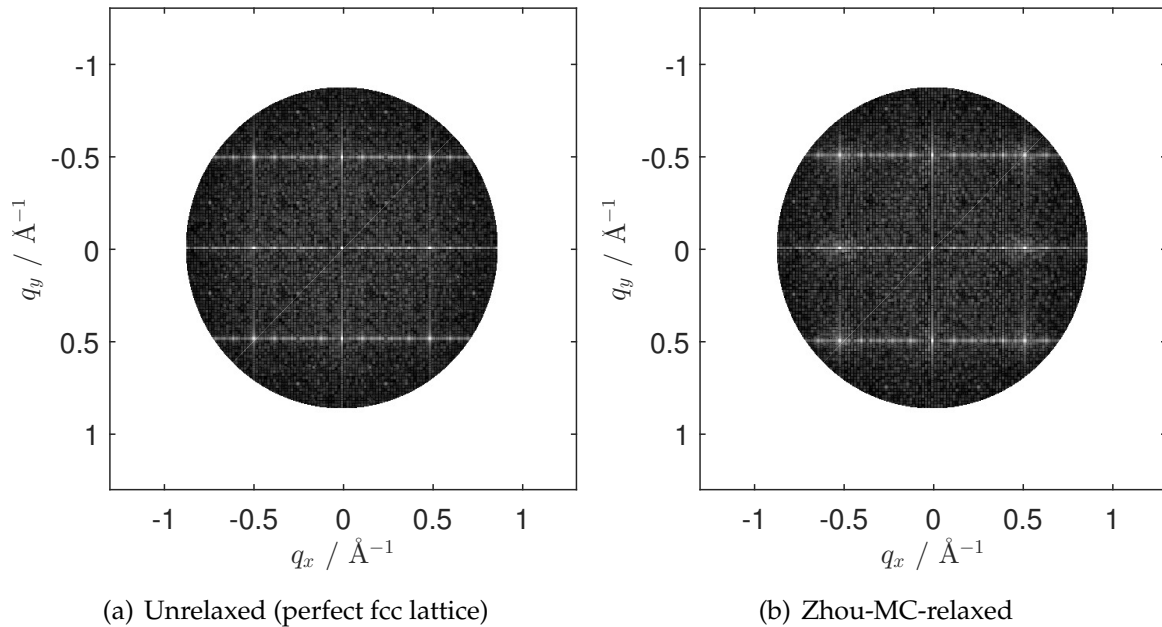


Figure 3.33.: Model 7: QSTEM coherent CBED images in the [001] zone axis before and after the MC-relaxation using the Zhou-potential, $t \approx 6.1$ nm

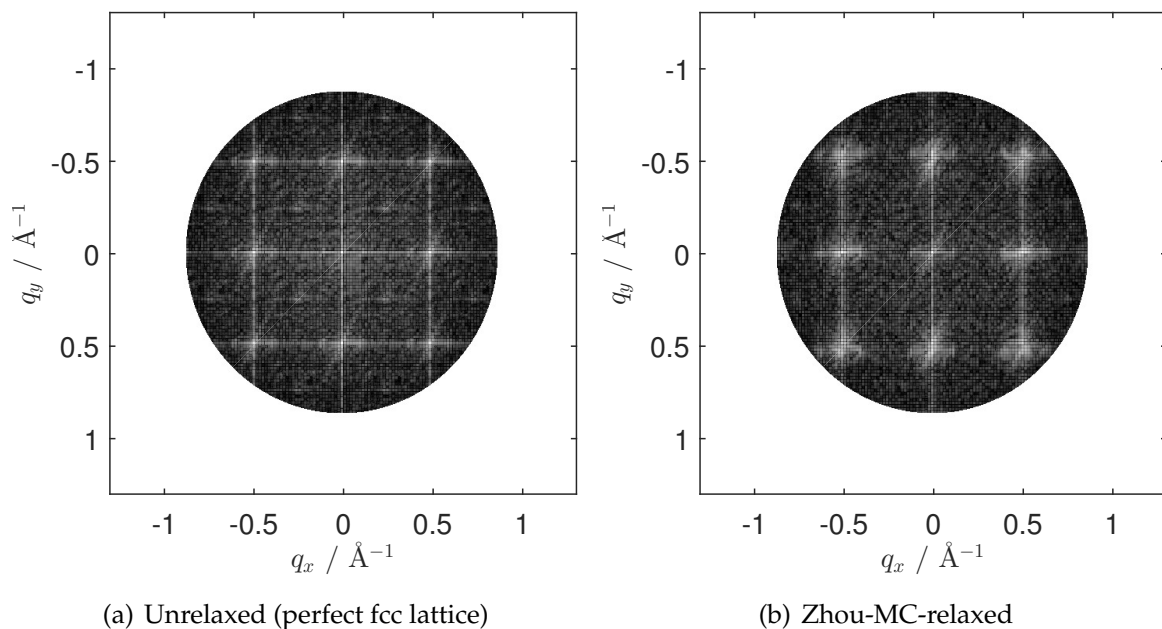


Figure 3.34.: Model 8: QSTEM coherent CBED images in the [001] zone axis before and after the MC-relaxation using the Zhou-potential, $t \approx 6.1$ nm

3.2. Experimental results

In contrast to the previous section, the figure captions in this one sometimes contain complementary evaluation which is not always repeated in the floating text. This should help the reader to find specific information where he or she would intuitively seek for it.

Two different gold-nickel specimens with $c_{\text{Ni}} = 0.291$ at% were investigated. Both had been repeatedly melted and quenched, whereupon they had been homogenized at approximately 900 °C (solid state) and quenched again. They were dissimilar in terms of aging¹⁶ and the (S)TEM preparation process:

1. aged for 10 hours at 150 °C, final thinning process via electropolishing
2. aged for 20 hours at 150 °C, final thinning process via conventional broad ion beam (BIB) milling with Argon ions

They varied greatly from each other, both in terms of preparation artifacts and contrast. The resulting image quality of the ion-thinned specimen was pretty poor when compared to the electrolytically thinned one. The high-resolution lattice images were significantly more blurred and the spinodal decomposition's effect could not be seen that distinctively, neither in STEM images nor in SAED recordings. The investigation of the electrolytically thinned specimen was by far more successful, the image quality was superior and the image analysis led to much more accurate results. Thus, images of the ion-thinned specimen and the associated analysis are omitted here.

The STEM images have been taken with a probe C_s ¹⁷ corrected FEI Titan³ G2 60-300 with a probe diameter of ≈ 0.7 Å (FWHM). An acceleration voltage of 300 kV was used. The nominal camera length for the Fischione FEI HAADF detector was set to 91 mm, which led to an HAADF collection semi-angle of $\beta = 62.2..214$ mrad. The convergence semi-angle was $\alpha = 19.6$ mrad.

As for TEM and SAED imaging, an FEI Tecnai G² FEG HRTEM has been used. The acceleration voltage was set to 200 kV.

Note that, for all presented (S)TEM images, the implementation into this document is non-loss-free due to data size issues, but the analysis of any greyscale values has been processed on the loss-free originals.

¹⁶to activate of the spinodal decomposition mechanism

¹⁷coefficient of third order spherical aberration

3.2.1. STEM micrographs

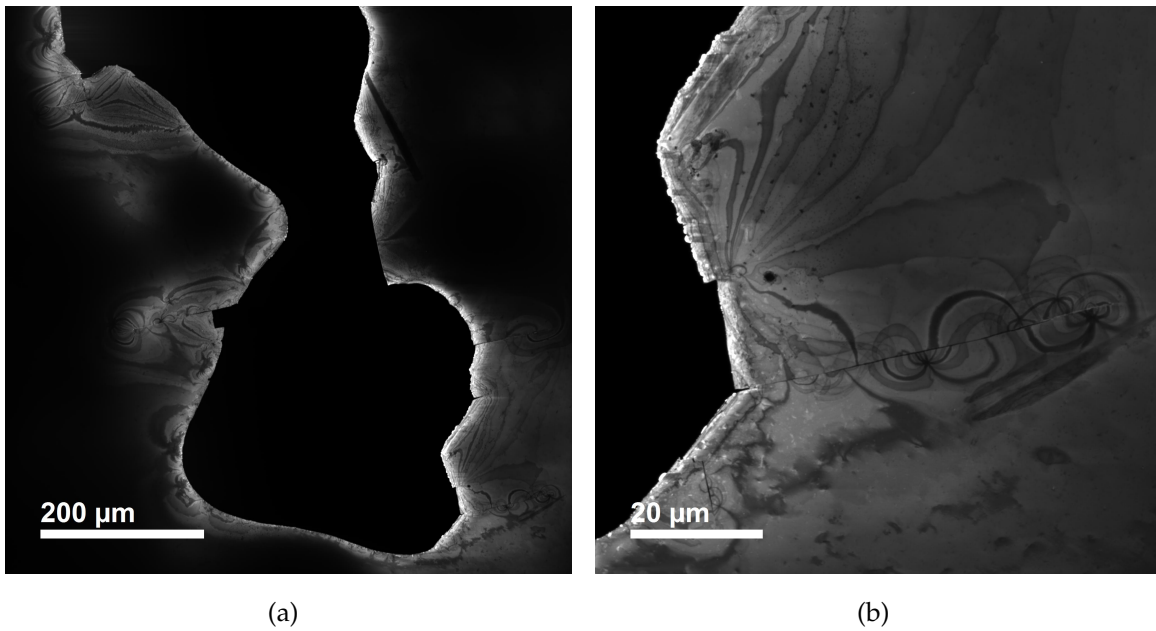


Figure 3.35.: HAADF-STEM micrographs of an electrolytically thinned Au_{70.9}Ni_{29.1} specimen at low magnifications

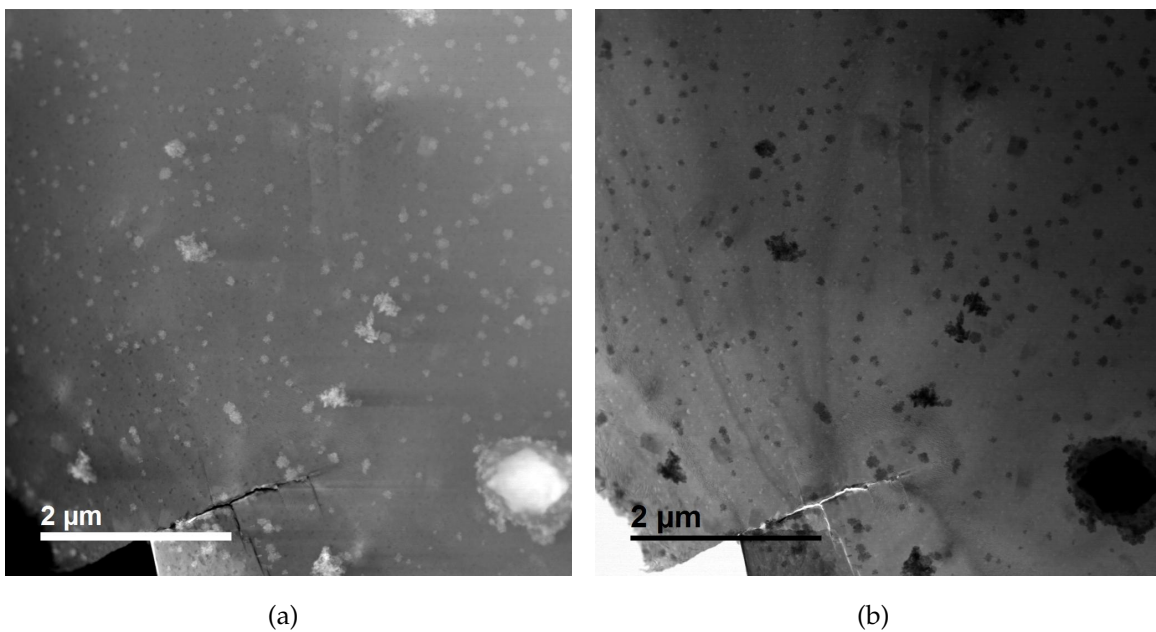


Figure 3.36.: HAADF- and BF-STEM micrograph of an electrolytically thinned Au_{70.9}Ni_{29.1} specimen at medium magnification; (a) is an HAADF image, (b) is the BF image belonging to (a).

3. Results and analysis

An HAADF-STEM image of the electrolytically thinned specimen at low magnification is illustrated in figure 3.35(a). It shows a hole stemming from the preparation process and the edge zones next to it. The region in the lower left corner is depicted in another HAADF-STEM micrograph at a bit higher magnification (see figure 3.35(b)). Figure 3.36 contains an HAADF- and the corresponding BF-STEM micrograph of the specimen at medium magnification. The individual features and the explanation of the contrast visible on these length scales were not topic of this work.

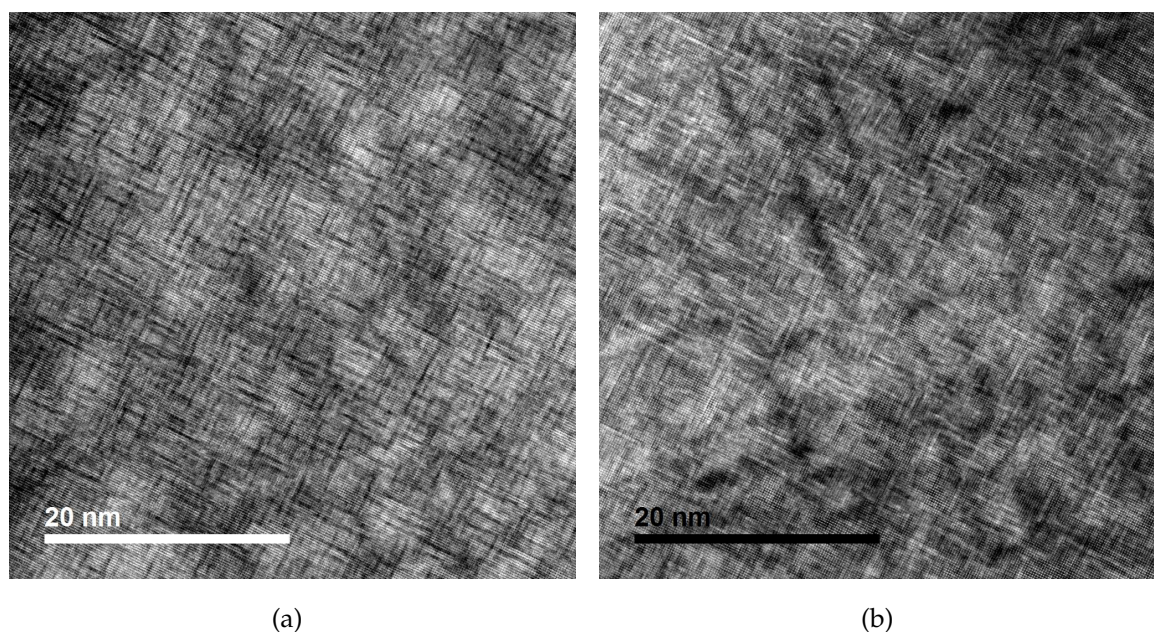


Figure 3.37.: HAADF- and BF-STEM micrographs of a $46 \times 46 \text{ nm}^2$ specimen region, zone axis [001]; (a) HAADF image, (b) BF image

In figure 3.37, an HAADF- and the corresponding BF-HRSTEM lattice image in the [001] zone axis are pictured. They show the spinodal decomposition in the crystallographic directions [100] and [010] distinctly. In the HAADF image, the dark stripes in these directions, which are about 0.2 nm in width, correspond to nickel-rich regions. They appear as bright stripes in the BF image.

The bright-dark variations on larger length scales can be split into two distinguishable phenomena. First, bright and dark stripes in the $\langle 110 \rangle$ -directions are visible, which are a few nanometers in width. They are not topic of this work. Second, there appear generally bright and dark areas on a length scale of or above 10 nanometers. This effect is even more pronounced in figure 3.38(a), which shows an HAADF-HRSTEM image of another specimen region at a bit worse resolution. The obvious

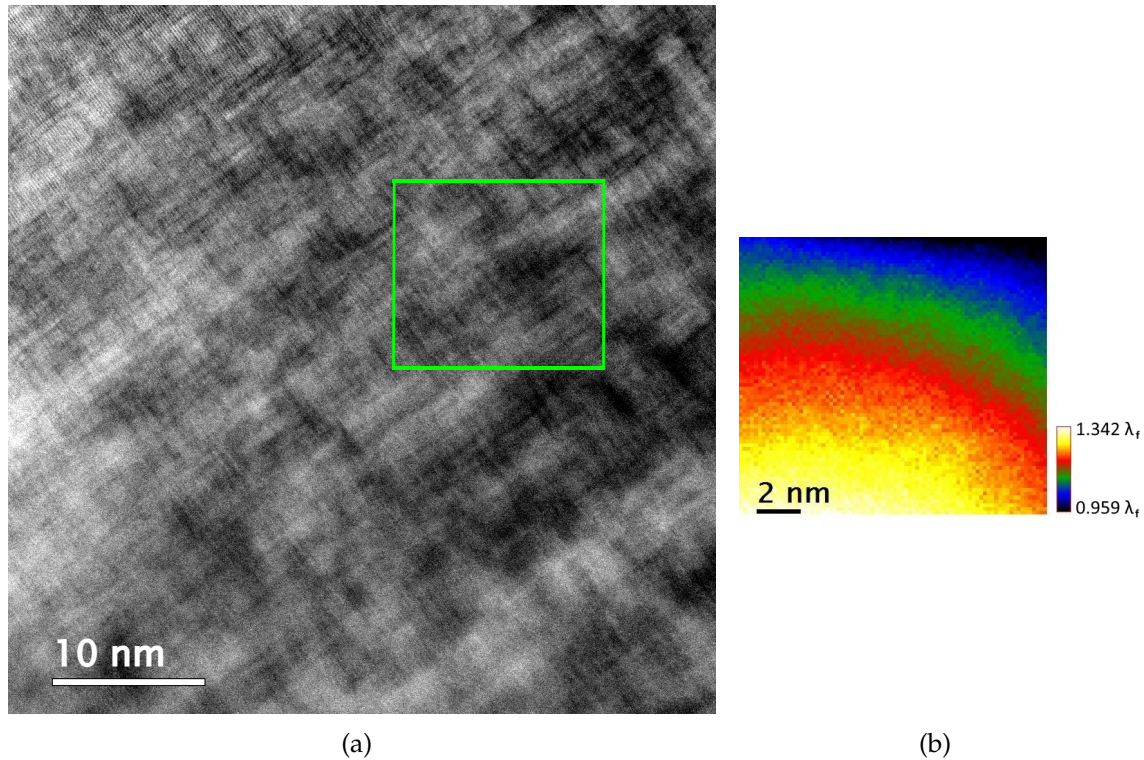


Figure 3.38.: (a) HAADF-STEM micrograph of a $46 \times 46 \text{ nm}^2$ specimen region, zone axis [001], and (b) relative thickness map of the marked section stemming from a t/λ - measurement

question is whether we see thickness contrast or not. On this account, a t/λ - measurement¹⁸ was performed. The relative thickness map of the section marked in figure 3.38(a) is shown in figure 3.38(b). It reveals that the variously bright appearing areas do not coincide with differently thick areas.

Thickness estimation

Additionally, the absolute thickness of this specimen region can approximately be determined. From the corresponding EELS spectrum (no figure) an average relative thickness of $t/\lambda_f \approx 1.17$ was calculated. The theoretical inelastic mean free path estimation is $\lambda_f = 69 \text{ nm}$ for 100 % Au, $\lambda_f = 95 \text{ nm}$ for 100 % Ni, and $\lambda_f = 74 \text{ nm}$ for a homogeneous phase of 70 % Au and 30 % Ni. Due to the spinodal decomposition mechanism the examined specimen exhibits no homogeneously mixed phase in the common sense. Knowing that, the average thickness of this specimen region can only roughly be estimated at between 80 and 110 nm.

¹⁸thickness over inelastic mean free path

FFT analysis

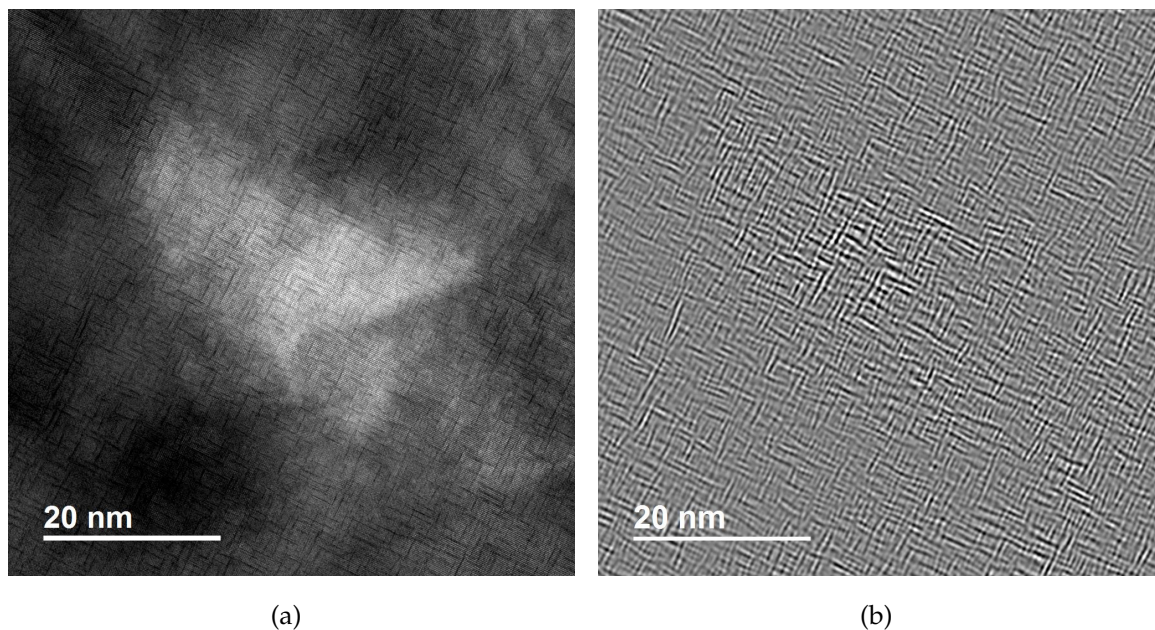


Figure 3.39.: (a) HAADF-STEM image of a $64 \times 64 \text{ nm}^2$ specimen region, zone axis [001], and (b) IFFT of the (000)-satellites in the associated FFT, which is depicted in figure 3.40.

Figure 3.39(a) shows another HAADF-HRSTEM image in the [001] zone axis. By means of the FFT of images like this one, we can derive some important things.

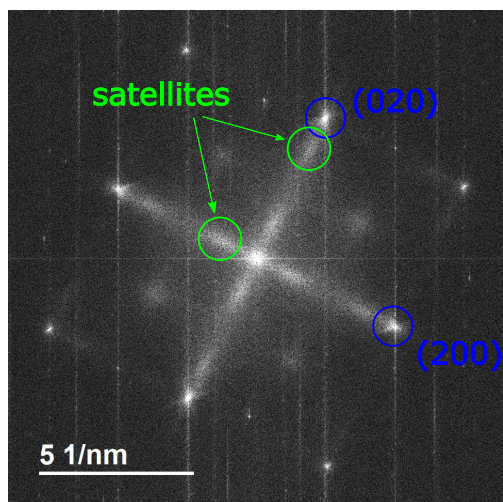


Figure 3.40.: FFT of the HAADF image in figure 3.39

The FFT image of figure 3.39(a), which is depicted in figure 3.40, exhibits satellites near the spatial frequencies corresponding to the reflections (000), (200), (020), (220), ..., in experimental diffraction patterns. They are caused by the periodic intensity variations, the concentration modulation respectively, with a wavelength in the range of 1 nm. The spots and their satellites are blurry because the wavelength varies, which has two reasons. On the one hand, the number of gold-rich planes in between two nickel-rich planes in the directions [100] and [010] fluctuates, and on the other hand, the

nickel atoms lead to lattice distortions.

Some features of the specimen can superiorly be visualized by means of the inverse transform of some spots in the FFT. Figure 3.39(b) shows the IFFT of the (000)-

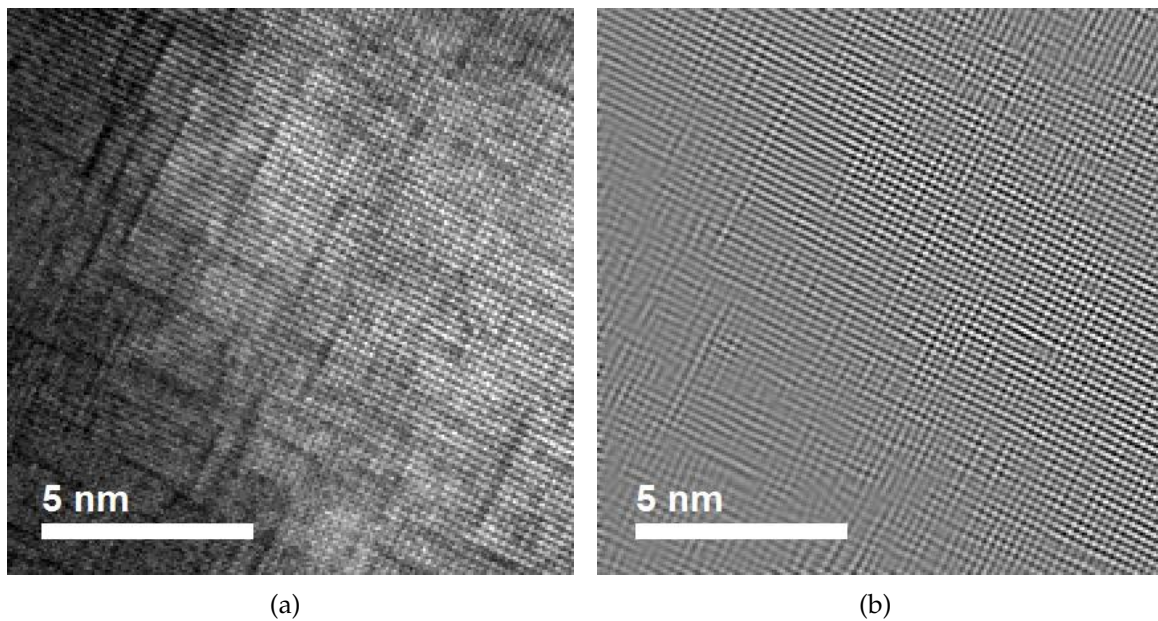


Figure 3.41.: (a) $13 \times 13 \text{ nm}^2$ section of the HAADF-STEM image of figure 3.39(a) and (b) IFFT of the fundamental spots (200) , (020) , $(\bar{2}00)$, $(0\bar{2}0)$ and their satellites in the FFT image of figure 3.40

satellites. It reduces the original image to the concentration variation pattern. Additionally, a smaller region of the image in figure 3.39(a) is enlarged in figure 3.41(a). In the IFFT of the fundamental $\{200\}$ -spots and their satellites (see figure 3.41(b)), the lattice distortions become visible more clearly.

Furthermore, there are spots in the FFT image that would in principle correspond to (110) , $(\bar{1}10)$, ..., reflections. These spatial frequencies do occur in the 2D image of an fcc structure in the $[001]$ zone axis and we will see them later in an SAED image as well. The $\{110\}$ -reflections are forbidden only for undisturbed fcc crystals without substitutional foreign atoms (see e.g. Williams & Carter (1998, ch. 16.3ff, p. 259ff)).

Gold-nickel contrast quantification

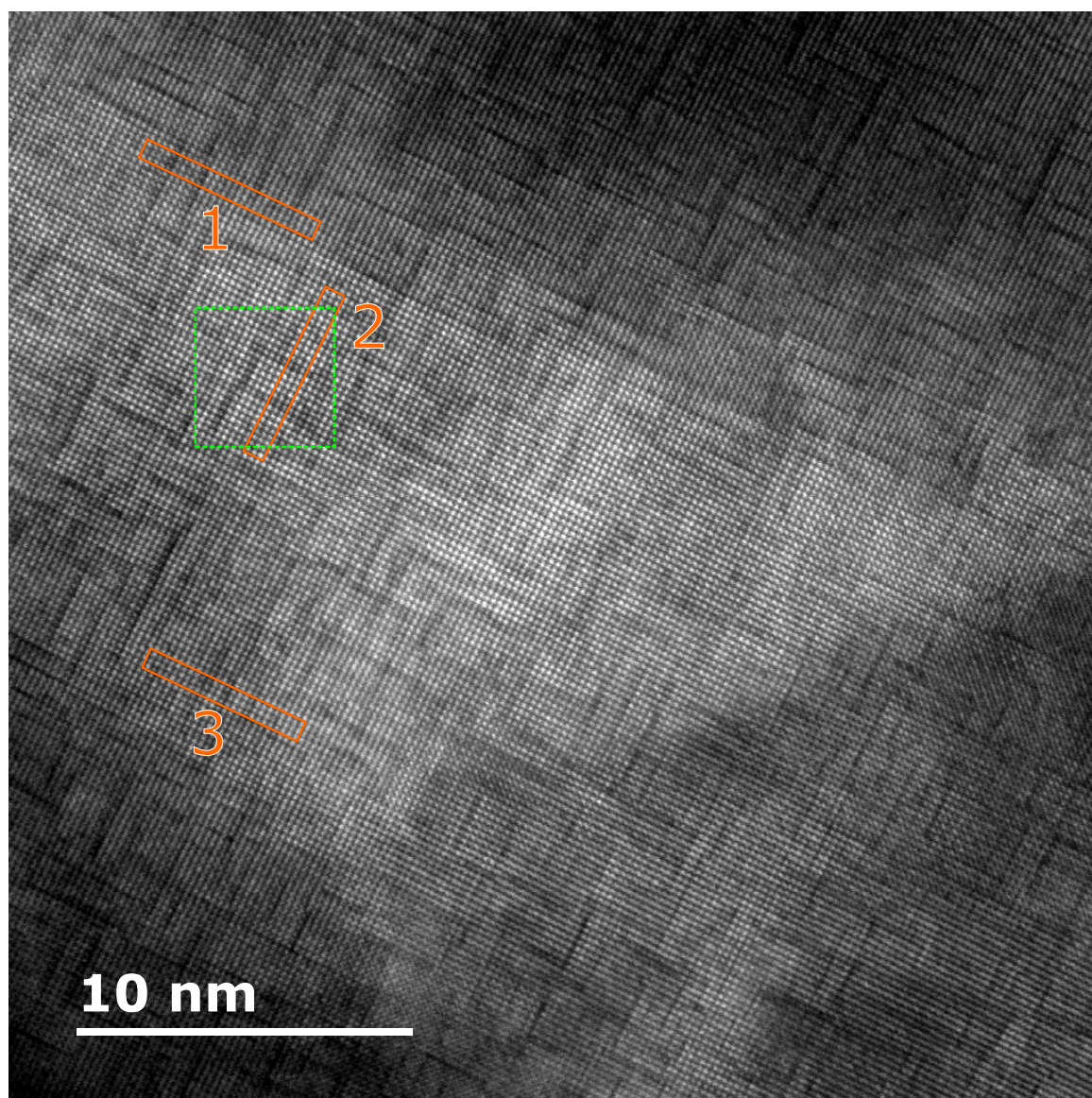
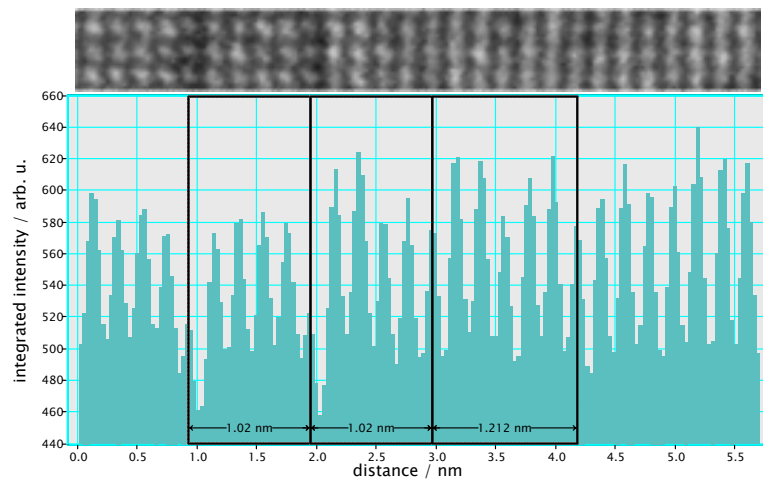


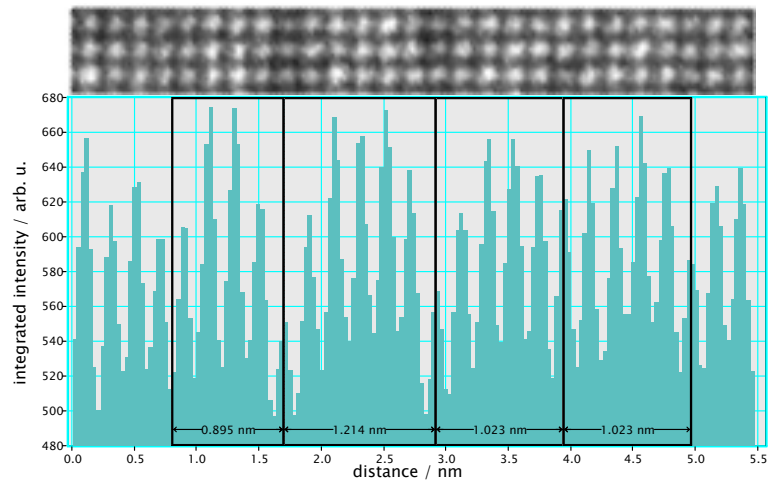
Figure 3.42.: HAADF-STEM micrograph of a $33 \times 33 \text{ nm}^2$ specimen region, zone axis [001]; Line profiles of the areas marked in orange (solid rectangles) are shown in figure 3.43, a detailed peak analysis of the section marked in green (dashed square) is illustrated in figure 3.44.

Figure 3.42 shows an HAADF-HRSTEM micrograph of another specimen region in the [001] zone axis. The image has a particularly high resolution (in the range of 1 \AA) and some regions in which the bright-dark variations on larger length scales can be neglected were carefully examined.

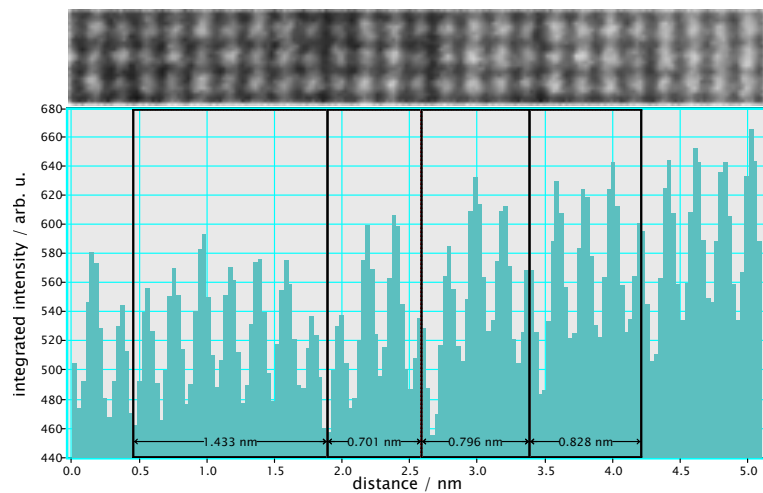
First, line profiles were created and analyzed. These are shown in figure 3.43.



(a) Line Profile 1



(b) Line Profile 2



(c) Line Profile 3

Figure 3.43.: Line profiles of the three areas marked in figure 3.42; The vacuum level was $I_{\text{vac}} = 42.0 \pm 0.5$ arb. u. on this scale.

3. Results and analysis

In agreement with former research, they affirm a wavelength in the nickel concentration modulation between 0.8 and 1.2 nm in these specimen regions. An in-depth analysis leads to mean HAADF intensity ratios of $I_{\text{low}}^*/I_{\text{high}}^* = 0.91(4), 0.90(3),$ and $0.92(3)$ for the lines profiles 1, 2, and 3, where $I^* = I - I_{\text{vac}}$. This corresponds to $C_{\text{In}} = \ln \frac{I_{\text{low}}^*}{I_{\text{high}}^*} = -0.10(4), -0.11(3),$ and $-0.09(3)$ according to equation (2.2). A t/λ - analysis has not been carried out for this specimen region, anyway, the average thickness should be in the range between 50 and 90 nm. If we assumed a thickness of about 60 nm, we would be able to directly compare these results to the iso-contrast plot in figure 3.16. We could state that the concentration difference between the columns should be roughly

$$\Delta c_{\text{Ni}} = c_{\text{high}} - c_{\text{low}} = 0.25(10). \quad (3.1)$$

Assuming this specimen region's composition is representative in terms of the total nickel concentration ($c_{\text{Ni}}^{\text{tot}} = 0.291$), since the average wavelength of the modulation is approximately 5 times the distance between (200) planes, we would find

$$\frac{4c_{\text{low}} + c_{\text{high}}}{5} = 0.291. \quad (3.2)$$

Combining these equations and solely taking uncertainties into account that propagate from wavelength and concentration difference, we could state $c_{\text{Ni}}^{\text{high}} = 0.49(13)$ and $c_{\text{Ni}}^{\text{low}} = 0.24(13)$.

Second, the peak detection and quantification code described in section 2.4 was applied to a $4 \times 4 \text{ nm}^2$ section of the micrograph in figure 3.42. The sequential conditioning of the image data is illustrated in figure 3.44. To begin with, the mean vacuum level was subtracted, which leads to the image displayed in figure 3.44(a). Then, a Patch-PCA noise filter was applied, which resulted in a better distinguishability of the peaks (see figure 3.44(b)). After that, the Voronoi segmentation was performed and the peaks were quantified. As we recognize by means of the Voronoi diagram (see figure 3.44(c)), the peak detection works fantastically for images in which the peaks are that well separated from each other. The blue and turquoise circles correspond to supposedly nickel-rich columns, the orange and red ones to gold-rich columns. A rough contrast analysis can be made on the basis of Voronoi diagram and histogram (see figure 3.44(d)). Nickel-rich atom columns feature an intensity of $I_{\text{Ni-rich}} \approx 4.1 \dots 4.7$, whereas gold-rich columns have an intensity of $I_{\text{Au-rich}} \approx 5.3 \dots 5.9$. Thus, we obtain an intensity ratio range of $0.7 \dots 0.9$ and $C_{\text{In}} = -0.36 \dots -0.10$. Cross-

checking these results with the iso-contrast plot in figure 3.16, we could suppose that the nickel concentration should be above 0.9 in the darkest and below 0.1 in the brightest atom columns.

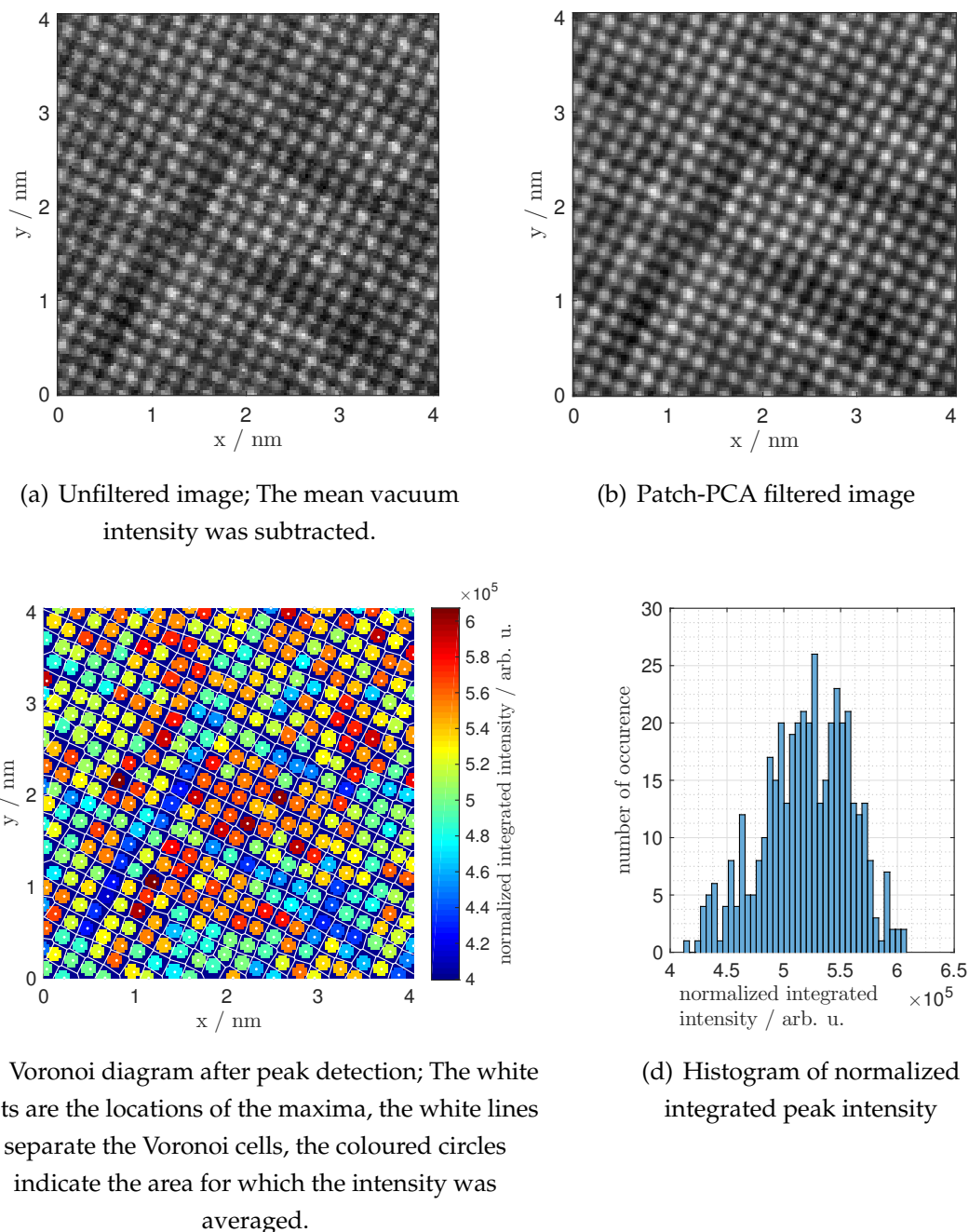


Figure 3.44.: Peak detection and quantification of the $4 \times 4 \text{ nm}^2$ image section marked in figure 3.42; The normalized integrated intensity in (c) and (d) is the average intensity value within a circle around a given peak. This is more meaningful than the sum of all intensities within a circle, because, to some extent, the normalization compensates for the systematic error that occurs if the cell boundaries are closer to a given peak than the maximum summation radius, especially important for peaks next to the image margins.

The values obtained by the different methods do not match exactly, but, in principle, their ranges are astoundingly plausible. Nevertheless, the subjunctive was used in order to pronounce the possible lack of correctness. The denoted values have to be regarded with suspicion, because the contrast in experimental images may be influenced by diverse non-eliminated parameters. This circumstance is carved out in section 4.2.

Influence of the signal-processing parameters ‘Contrast’ and ‘Brightness’

In order to verify the relationship $I_{ADC}(C, B) = I_{DET} \cdot k_C \cdot C + k_B \cdot B - \Delta I_0$ according to equation (2.4), the same region of the electrolytically thinned specimen was recorded multiple times, each time with an individual pair of the parameters ‘Brightness’ B and ‘Contrast’ C . After applying a specimen drift correction to the image stack, the grey scale values were evaluated. The maximum, the minimum and the average grey scale values in dependence of the parameters B and C are depicted in figure 3.45. They are all not monotonously increasing as a function of C for constant B , and they grow for a step in ‘Brightness’ from $B = 0.35 \rightarrow 0.3$ and an unchanged ‘Contrast’ value $C = 0.55$. Thence, neither an offset in compliance with $k_B \cdot B$ nor a multiplier as per $k_C \cdot C$ could be ascertained.

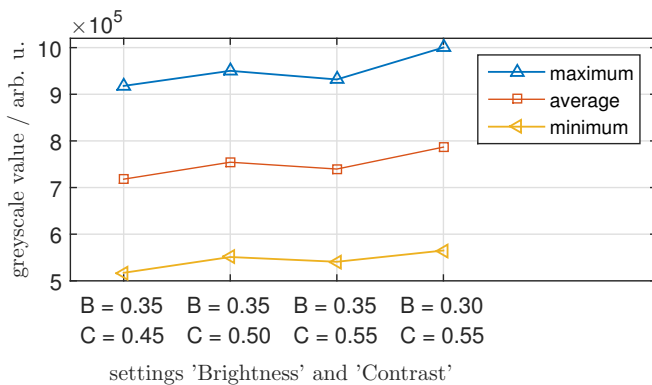


Figure 3.45.: Maximum, minimum and average grey scale value for the image series regarding the signal-processing parameters contrast and brightness

This result does not allow us to affirm or contradict the linear relation between I_{ADC} and I_{DET} by means of the obtained data. Regardless of the unsuccessful confirmation, note here that, in the contrast quantification presented before, it was presumed that equation (2.4) would hold true if both the detector signal as well as the ADC input were

neither over- nor undersaturated. There was no better way of eliminating the effects of the ‘Brightness’ B and the zero-point offset ΔI_0 on intensity ratios in images than the subtraction of the mean vacuum intensity for the same values B and C .

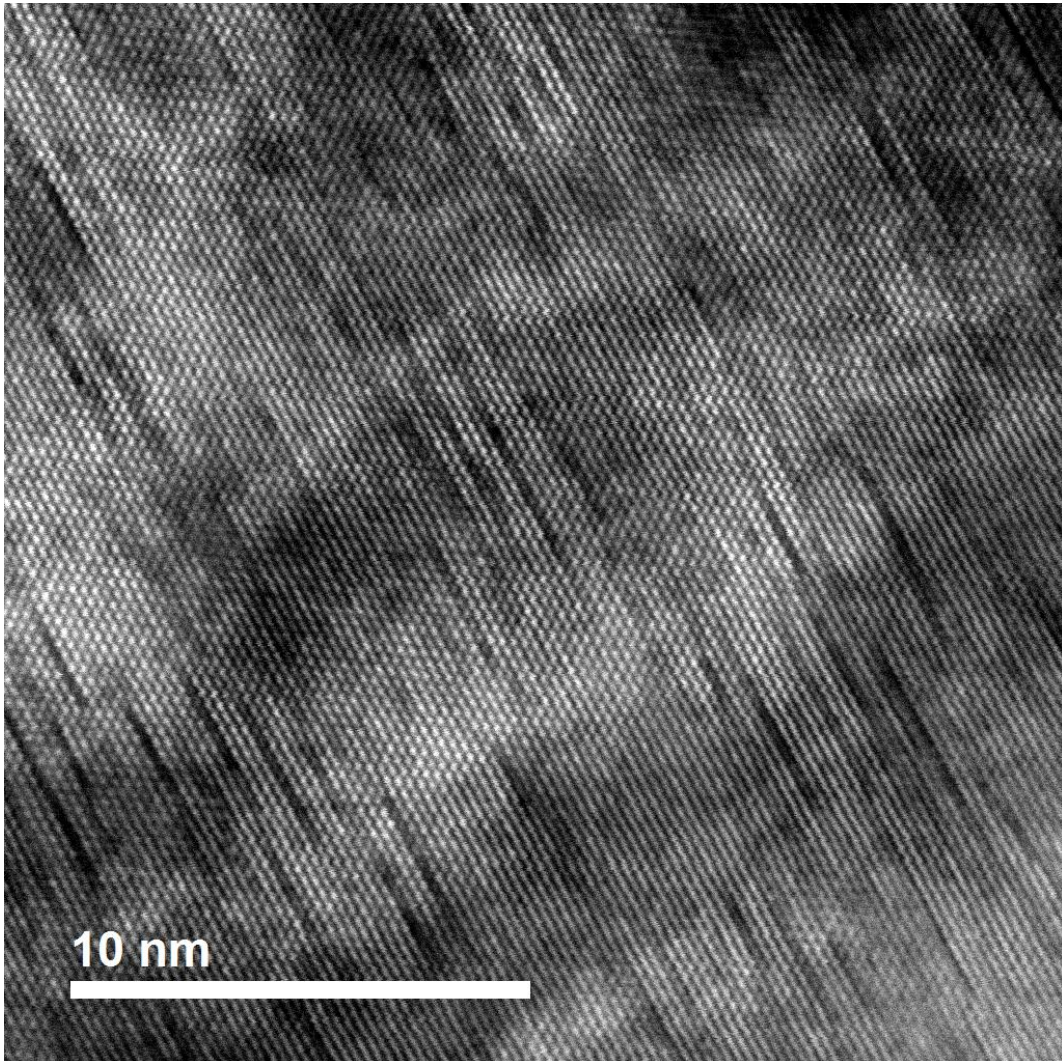
[011] zone axis

Figure 3.46.: HAADF-STEM micrograph of a $23 \times 23 \text{ nm}^2$ specimen region, zone axis [011]; The associated FFT is depicted in figure 3.47(a).

To round the HAADF-STEM imaging of this specimen up, figure 3.46 shows an HAADF-HRSTEM lattice images in the [011] zone axis and the spinodal decomposition in the crystallographic direction [100], which becomes evident by means of the FFT depicted in figure 3.47(a) and the theoretical diffraction pattern in figure 3.47(b). For 300 keV - electrons and this lattice constant, the theoretical distance to the Laue circle center is 4.90323 nm^{-1} for the spots (200) and $(\bar{2}00)$, and 4.24633 nm^{-1} for the spots $(11\bar{1})$, $(\bar{1}1\bar{1})$, $(\bar{1}\bar{1}\bar{1})$, and $(1\bar{1}\bar{1})$.

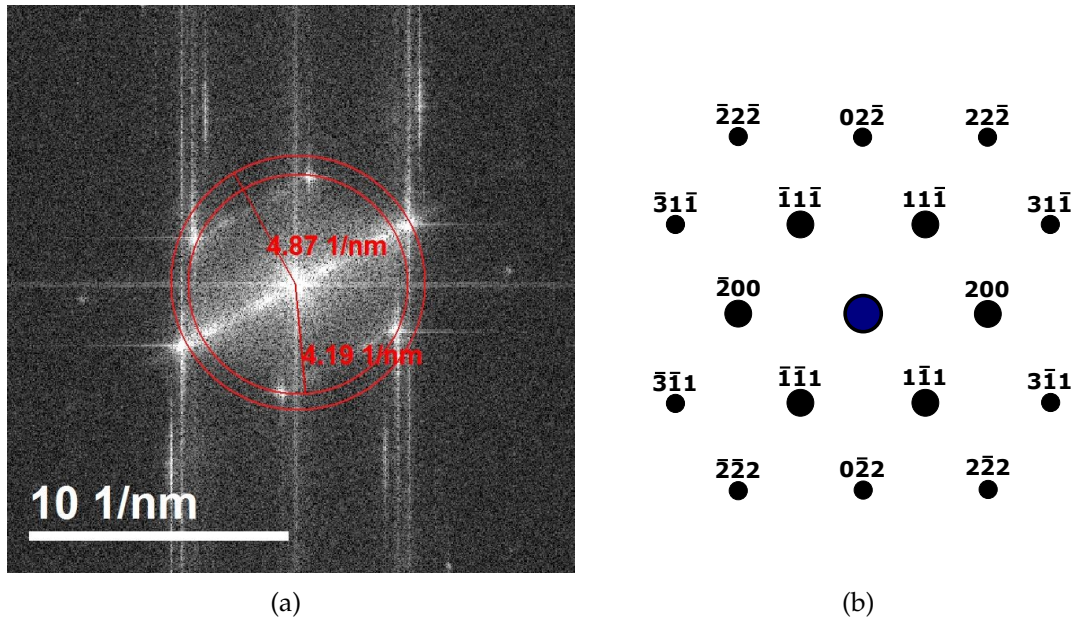


Figure 3.47.: (a) FFT of the HAADF-STEM image in figure 3.46 and (b) the corresponding computed diffraction pattern of an fcc lattice with a parameter of 0.407894 nm in the zone axis [011]

3.2.2. TEM and SAED images

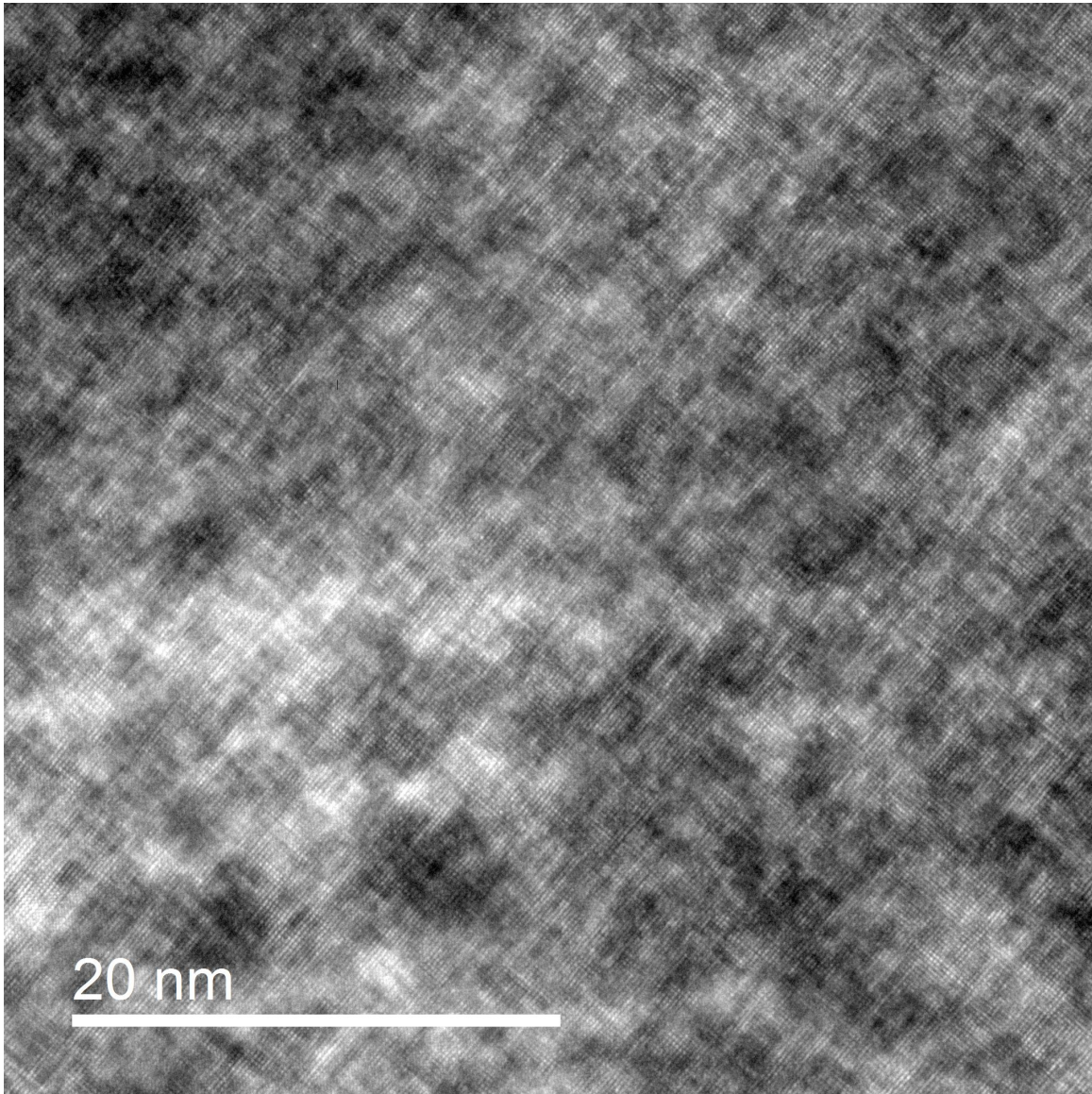


Figure 3.48.: ZL energy-filtered BF-TEM image of a $45 \times 45 \text{ nm}^2$ specimen region in the zone axis [001]

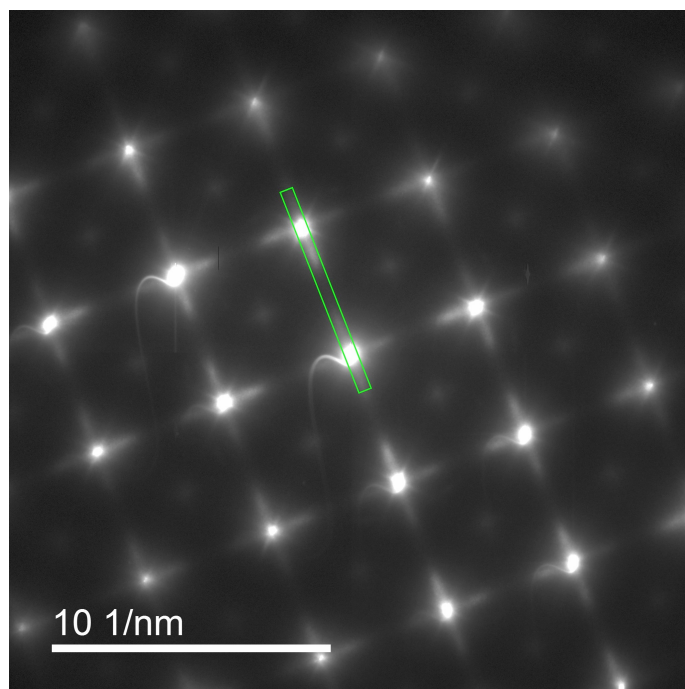
The contrast pattern stemming from the spinodal decomposition mechanism is also perceivable in the ZL filtered BF-HRTEM image of the electrolytically thinned specimen (see figure 3.48). An SAED image and an associated line profile including Gaussian fits are illustrated figure 3.49. The evaluation yielded the following:

- The distance between the main reflections (000), (200), (020), (220), ..., is $q_{13} = G_{200} = 4.9(2) \text{ nm}^{-1}$, which corresponds to $d_{200} = 0.204(8) \text{ nm}$. Since the nickel

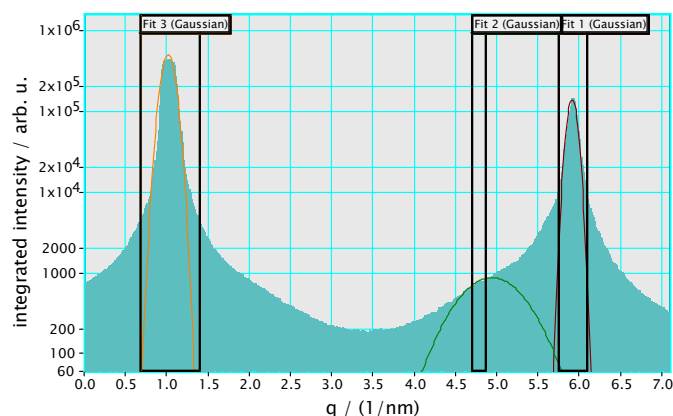
3. Results and analysis

impurities lead to lattice distortions, this result including the uncertainty is excellently consonant with our expectations.

- Taking into account mean values and standard deviations of the Gaussian fits and their large uncertainties, the distance of the main reflections and their diffuse satellites is $q_{12} = 0.4 \dots 1.1 \text{ nm}^{-1}$, which leads to a wavelength in the nickel concentration modulation of $\lambda = 0.9 \dots 2.5 \text{ nm}$.



(a) SAED recording, gamma-corrected with $\gamma = 1.5$ in order to make the $\{110\}$ -reflections visible to the naked eye; The line profile in (b) corresponds to the uncorrected image.



(b) Line profile between the reflections marked in green (solid rectangle) in (a) and Gaussian fits

Figure 3.49.: SAED recording in the zone axis $[001]$ and line profile

4. Conclusion

4.1. Summary

Various models with differently arranged substitutional nickel atoms in the gold matrix were created and multislice simulations for imaging in the [001] zone axis were carried out via QSTEM. The changes in the simulated HAADF-, BF-, and ABF-STEM images caused by variations of model thickness, nickel impurity, and convergence angle of the incident electron beam were analyzed. The used total collection angle range of the HAADF detector was split into smaller sectors, for which the detected intensities were separately investigated.

The multislice simulation results show a non-linear behavior of the BF/HAADF signal as a function of thickness. They indicate that the thinner the specimen, the better the obtained relative BF/HAADF thickness contrast. Vividly explained, this means that the intensity ratio between specimen regions that are 25 and 20 nm thick is higher than for regions 50 and 40 nm in thickness. ABF signals feature oscillating behavior as a function of thickness.

The angular distribution of the electrons scattered by gold atom columns and hitting the HAADF detectors is concentrated in the semi-angle of collection ranges from 85.0 to 108.0, from 131.0 to 142.5, and from 165.5 to 177.0 mrad. As for nickel atom columns, distinct peaks were detected for the ranges from 96.5 to 108.0 and from 131.0 to 142.5 mrad.

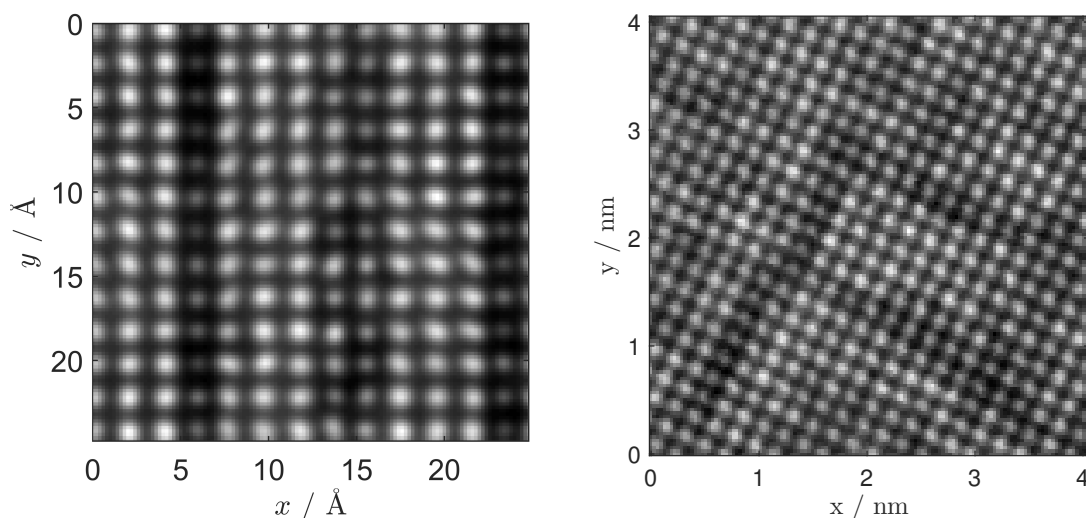
The semi-angle of convergence has a strong influence on absolute intensities for all investigated detectors, whereas the contrast between gold and nickel remains extensively unaffected.

The gold-nickel contrast heavily depends on the model's thickness. It is best for thin models and monotonously gets worse with increasing thickness. An approximate thickness value for which any contrast between pure gold and pure nickel disappears cannot be ascertained from the simulation data, because the time consumption

4. Conclusion

of simulations would have been too large for thicknesses above 60 nm. The absolute HAADF-intensity as a function of the mean atomic number is largely linear, so the Z-contrast obtained from the performed QSTEM simulations is well in accordance with theory concerning incoherent scattering from inhomogeneous atom columns. The effects of a given atom column on its neighboring ones are negligible in the investigated thickness range (up to 60 nm).

The applied alloy relaxation methods reduce the elongation of the gold-nickel models especially perpendicular to nickel-rich planes, which conforms to expectations. The exact amount of distortion has not been cross-checked with appropriate (S)TEM images or dilatation experiments in the scope of this work. The results stemming from Monte Carlo simulations using the embedded atom model potential according to Zhou *et al.* (2001) lead to QSTEM HAADF images that visually appear quite similar to some sections in experimental HAADF micrographs (see figure 4.1).



(a) Simulated QSTEM HAADF ($\beta = 73.5 \dots 200$ mrad) image of an MC-relaxed Au-Ni model in the [001] zone axis. The model had a sine-squared-shaped nickel concentration modulation in [100]-direction ($c_{\text{Ni}}^{\text{tot}} = 0.48$ at%) and a thickness of 57.6(1) nm.

(b) Experimental HAADF-STEM ($\beta = 62.2 \dots 214$ mrad) image of a Au-Ni specimen in the [001] zone axis. The specimen had a total nickel concentration of 0.291 at% and a thickness of 70(20) nm. It had been fabricated in such a way that spinodal decomposition occurs.

Figure 4.1.: Juxtaposition of a simulated and an experimental HAADF-STEM image

Experimentally, BF-STEM, HAADF-STEM, BF-TEM, and SAED images of a spin-

odally decomposed Au-Ni specimen were taken. The spinodal decomposition mechanism was made visible in the crystallographic $\langle 100 \rangle$ -directions, by means of all mentioned methods. The spatial resolution of the obtained HAADF-STEM lattice images in combination with the superior specimen quality were sufficient to perform a computer-aided analysis of the contrast between individual atom columns.

4.2. Uncertainties regarding the comparability of simulation and experiment

A direct contrast comparison between simulated and experimental images can be made with the applied, partially newly developed methods, but a well-assured composition determination of the atom columns is not achievable for a variety of reasons. There are a few main causes to be emphasized:

First, there is a lack of simulation data because extensive simulation series for models greater than 50 nm in thickness and scanning regions larger than a few square nanometers with pixel sizes in the sub-angstrom range take several months to be acquired with the hardware available for this work and the used software. A trade-off between the quoted quantities had to be made in order to stay within a reasonable computational effort.

Second, the reliability of multislice simulation results has not been experimentally evaluated and validated to the full extent. Therefore, inductive conclusions based on imprecise individual results can mislead to potentially wrong general laws.

Third, there are major discrepancies between the idealized model and simulation conditions and their physical counterparts. In an experimental STEM setup, many factors are present that prevent the construction of a situation that is similar to the idealized simulation configuration. Regarding the specimen, the influences of preparation and/or beam damage, irregular thickness variations, and contamination layers – just to name a few properties not matching the used models – make a dependable comparison very difficult. Regarding the microscope, it is not self-evident that beam current fluctuations and/or specimen drift do not get too high during a measurement. In order to make quantitative statements reliable, requirements that currently are hardly satisfiable have to be met.

Fourth, the acquisition of precise thickness maps for experimentally captured specimen regions could not be realized. The obtained thickness estimations are tainted

with large uncertainties. In addition, the signal-processing parameters 'Brightness' and 'Contrast', which can arbitrarily be adjusted by the microscope operator before capturing a micrograph on the used STEM, change intensity ratios. While in theory it is possible to get rid of the parameter 'Brightness' by subtracting the mean vacuum level for the same settings, which improves the signal-to-noise ratio and makes intensity ratios independent of 'Contrast', the influences of both parameters could not be decrypted accurately in practice.

Nevertheless, based upon the acquired simulation data, the concept of an iso-contrast plot (see figure 3.16) has been demonstrated, which may become particularly useful if further improved and reviewed with care. The comparison with experimentally observed contrast values, which have been deliberately conditioned, looks very promising.

4.3. Outlook

Overall, the simulation activity produced roughly 35.000 images of various gold-nickel alloy models, of which about 20.000 were analyzed. A big part of this work's output are the developed approaches to create and analyze lattice imaging simulations.

The sequential approach of simulations to the experiment was more or less successful. The developed code to perform lattice relaxations of inhomogeneously mixed alloys using a Monte Carlo algorithm delivers reasonable results, however, in order to reliably verify the method, dilatation experiments of similar physical specimens are definitely required. Another issue is the computational effort of the code. Several improvements need to be done to make extensive usage in the future expedient.

Although very challenging, simulation concepts that include more non-ideal specimen and microscope properties could bring us one step closer to concentration quantification via STEM imaging. To broaden a well-grounded quantitative contrast comparability between simulated and experimental images, further elaborate improvements both on the experimental as well as on the simulation side are needed. A small step towards and on the road to quantitative composition determination on the basis of HAADF-STEM contrast has been taken, but there is still a long way to go.

Bibliography

- Anderson, S. C., Birkeland, C. R., Anstis, G. R., & Cockayne, D. J. H. 1997. An approach to quantitative compositional profiling at near-atomic resolution using high-angle annular dark field imaging. *Ultramicroscopy*, **69**(2), 83 – 103.
- Bezanson, J., Karpinski, S., Shah, V. B., & Edelman, A. 2012. Julia: A Fast Dynamic Language for Technical Computing. *CoRR*, **abs/1209.5145**.
- Binder, K., & Heermann, D. W. 1988. *Monte Carlo Simulation in Statistical Physics*. Springer-Verlag.
- Brown, I. D., & McMahon, B. 2002. CIF: the computer language of crystallography. *Acta Crystallographica Section B*, **58**(3 Part 1), 317–324.
- Brydson, R. 2011. *Aberration-corrected analytical transmission electron microscopy*. John Wiley & Sons.
- Cahn, J. W. 1961. On spinodal decomposition. *Acta metallurgica*, **9**(9), 795–801.
- Carter, C. B., Williams, D. B., *et al.* . 2016. *Transmission electron microscopy*. Springer International Publishing.
- Dunn, P. F. 2010. *Measurement and data analysis for engineering and science*. 2nd edn. CRC press.
- Fechner, G. T. 1860. *Elemente der Psychophysik, Zweiter Theil*. Leipzig: Breitkopf & Härtel.
- Finnis, M. W., & Sinclair, J. E. 1984. A simple empirical N-body potential for transition metals. *Philosophical Magazine A*, **50**(1), 45–55.
- FIZ Karlsruhe - Leibniz Institute for Information Infrastructure. 2016. *Inorganic Crystal Structure Database (ICSD)*. icsd.fiz-karlsruhe.de. [online, retrieved on 10-October-2016].

- Frenkel, D., & Smit, B. 2002. *Understanding Molecular Simulations: from Algorithms to Applications*. San Diego: Academic Press.
- Fukano, Y. 1961. Study on Precipitation Phenomena in Thin Films of Supersaturated Gold-Nickel Alloy. *Journal of the Physical Society of Japan*, **16**(6), 1195–1204.
- Gottstein, G. 2014. *Materialwissenschaft und Werkstofftechnik: Physikalische Grundlagen*. 4th edn. Springer-Verlag.
- Gust, W., Predel, B., & Nguyen-Tat, T. 1976. Investigation of the Discontinuous Precipitation in Polycrystalline Au-Ni Alloys. *Zeitschrift für Metallkunde*, **67**(2), 110–117.
- Hall, S. R., Allen, F. H., & Brown, I. D. 1991. The crystallographic information file (CIF): a new standard archive file for crystallography. *Acta Crystallographica Section A*, **47**(6), 655–685.
- Harada, J., & Ohshima, K. 1981. X-ray diffraction study of fine gold particles prepared by gas evaporation technique. *Surface Science*, **106**(1), 51 – 57.
- Hastings, W. K. 1970. Monte Carlo sampling methods using Markov chains and their applications. *Biometrika*, **57**(1), 97–109.
- Hawkes, P., & Spence, J. C. H. 2008. *Science of microscopy*. Springer Science & Business Media.
- Hofer, F. 1982. *Thermodynamische Untersuchungen am System Gold-Nickel*. Ph.D. thesis, Graz University of Technology.
- Hofer, F., & Warbichler, P. 1984. An Electron Microscopy Study of Spinodal Decomposition of Au–Ni Alloys. *Electron Microscopy 1984.*, **2**, 887–888.
- Hofer, F., & Warbichler, P. 1985. Spinodal Decomposition in the Gold-Nickel System. *Zeitschrift für Metallkunde*, **76**(1), 11–15.
- In-Kook Suh, Ohta, H., & Waseda, Y. 1988. High-temperature thermal expansion of six metallic elements measured by dilatation method and X-ray diffraction. *Journal of Materials Science*, **23**(2), 757–760.
- Johnson, R. A. 1989. Alloy models with the embedded-atom method. *Phys. Rev. B*, **39**(Jun), 12554–12559.
- Kirkland, E. J. 2010. *Advanced computing in electron microscopy*. Springer Science & Business Media.

- Knez, D. 2017. *Scanning Transmission Electron Microscopy of Metallic Clusters and Nanoalloys*. Ph.D. thesis, Graz University of Technology.
- Koch, C. T. 2002. *Determination of core structure periodicity and point defect density along dislocations*. Ph.D. thesis.
- Koch, C. T. 2016. *QSTEM 2.40 software package*. www.qstem.org. [online, retrieved on 07-October-2016].
- Köster, W., & Dannöhl, W. 1936. *Zeitschrift für Metallkunde*, **28**, 248.
- LeBeau, J. M., & Stemmer, S. 2008. Experimental quantification of annular dark-field images in scanning transmission electron microscopy. *Ultramicroscopy*, **108**(12), 1653 – 1658.
- LeBeau, J. M., Findlay, S. D., Allen, L. J., & Stemmer, S. 2008. Quantitative atomic resolution scanning transmission electron microscopy. *Physical Review Letters*, **100**(20), 206101.
- Martinez, G. T., Rosenauer, A., De Backer, A., Verbeeck, J., & Van Aert, S. 2014. Quantitative composition determination at the atomic level using model-based high-angle annular dark field scanning transmission electron microscopy. *Ultramicroscopy*, **137**(Supplement C), 12 – 19.
- Metropolis, N., Rosenbluth, A. W., Rosenbluth, M. N., Teller, A. H., & Teller, E. 1953. Equation of state calculations by fast computing machines. *The journal of chemical physics*, **21**(6), 1087–1092.
- Moss, S. C. 1966. Local Order in Solid Alloys-1, Local Atomic Arrangements Studied by X-Ray Diffraction, Aime Metal. *Pages 95–122 of: Soc. Conf., Gordon et Breach Science Publishers, New York*, vol. 36.
- National Institute of Standards and Technology. 2017. *The NIST Reference on Constants, Units, and Uncertainty*. physics.nist.gov/cuu. [online, retrieved on 16-February-2017].
- Nellist, P. D., & Pennycook, S. J. 2000. The principles and interpretation of annular dark-field Z-contrast imaging. *Advances in Imaging and Electron Physics*, **113**, 147 – 203.
- Palmer, D., Conley, M., Parsonson, L., Rimmer, L., & Stenson, I. 2016. *CrystalMaker*

- for Windows 9.2.8 (664), CrystalMaker Software Ltd. www.crystallmaker.com. [online, retrieved on 07-October-2016].
- Pearson, K. 1901. LIII. On lines and planes of closest fit to systems of points in space. *The London, Edinburgh, and Dublin Philosophical Magazine and Journal of Science*, **2**(11), 559–572.
- Plimpton, S., Thompson, A., Moore, S., Kohlmeyer, A., Crozier, P., Stevens, M., & Shan, R. 2017. LAMMPS. *Large-scale Atomic/Molecular Massively Parallel Simulator*. lammmps.sandia.gov. [online, retrieved on 02-February-2017].
- Predel, B. 1982. *Heterogene Gleichgewichte: Grundlagen und Anwendungen*. Darmstadt: Steinkopff.
- Rafii-Tabar, H., & Sutton, A. P. 1991. Long-range Finnis-Sinclair potentials for fcc metallic alloys. *Philosophical Magazine Letters*, **63**(4), 217–224.
- Straumanis, M. E. 1971. Redetermination of lattice parameters, densities and thermal expansion coefficients of silver and gold, and the perfection of their structures. *Monatshefte für Chemie / Chemical Monthly*, **102**(5), 1377–1386.
- Sutton, A. P., & Chen, J. 1990. Long-range Finnis-Sinclair potentials. *Philosophical Magazine Letters*, **61**(3), 139–146.
- Swope, W. C., Andersen, H. C., Berens, P. H., & Wilson, K. R. 1982. A computer simulation method for the calculation of equilibrium constants for the formation of physical clusters of molecules: Application to small water clusters. *The Journal of Chemical Physics*, **76**(1), 637–649.
- Underwood, E. E. 1954. *Precipitation in gold-nickel alloys*. Ph.D. thesis, Massachusetts Institute of Technology.
- Verlet, L. 1967. Computer "experiments" on classical fluids. I. Thermodynamical properties of Lennard-Jones molecules. *Physical review*, **159**(1), 98.
- Voronoi, G. 1908. Nouvelles applications des paramètres continus à la théorie des formes quadratiques. Deuxième mémoire. Recherches sur les paralléloèdres primitifs. *Journal für die reine und angewandte Mathematik*, **134**, 198–287.
- Wadley, H. N. G., Zhou, X., Johnson, R. A., & Neurock, M. 2001. Mechanisms, models and methods of vapor deposition. *Progress in Materials Science*, **46**(3-4), 329–377.

- Wang, J., Lu, X. G., Sundman, B., & Su, X. 2005. Thermodynamic assessment of the Au-Ni system. *Calphad*, **29**(4), 263–268.
- Williams, D. B., & Carter, C. B. 1998. *Transmission electron microscopy: a textbook for materials science*. 2nd edn. Springer.
- Woodilla, J. E., & Averbach, B. L. 1968. Modulated structures in Au-Ni alloys. *Acta Metallurgica*, **16**(2), 255 – 263.
- Wu, C. K. 1978. *High-resolution electron microscopy studies of Au-Ni spinodal alloys*. Ph.D. thesis, University of California.
- Zhou, X. W., Wadley, H. N. G., Johnson, R. A., Larson, D. J., Tabat, N., Cerezo, A., Petford-Long, A. K., Smith, G. D. W., Clifton, P. H., Martens, R. L., & Kelly, T. F. 2001. Atomic scale structure of sputtered metal multilayers. *Acta Materialia*, **49**(19), 4005 – 4015.
- Zhou, X. W., Johnson, R. A., & Wadley, H. N. G. 2004. Misfit-energy-increasing dislocations in vapor-deposited CoFe/NiFe multilayers. *Phys. Rev. B*, **69**(Apr), 144113.

List of Figures

2.1. Phase diagram of Au-Ni alloys between 400 K and 1800 K including chemical spinodal line; Source: Wang <i>et al.</i> (2005)	3
2.2. Schematic illustration of the phase diagram and the Gibbs free energy of a mixed phase with miscibility gap; Source: Gottstein (2014)	4
2.3. Phase diagram of solid Au-Ni alloys between 200 K and 1100 K including coherent spinodal lines according to various research studies; Source: Hofer & Warbichler (1985)	5
2.4. Transmission electron micrographs and electron diffraction images of a Au-Ni specimen with $c_{Ni} = 0.291$ for different aging durations, [001] zone axis; Source: Hofer (1982)	5
2.5. Schematic of the detector setup for STEM imaging	7
2.6. Illustration of the effects of the signal-processing parameters ‘Contrast’ and ‘Brightness’	13
2.7. Two-atom energies vs. interatomic separation for the used potentials .	20
3.1. Inclined crack of simulation model 1 and views of models 2 to 6 along the [001] direction	30
3.2. Model 1: QSTEM HAADF-, BF-, and ABF-images for different thicknesses	31
3.3. Model 1: Average HAADF-, BF-, and ABF-intensity of gold atom columns vs. thickness	32
3.4. Model 1: Log-log plot of average HAADF- and BF-intensity vs. thickness	33
3.5. Model 1: Average HAADF-intensity of gold atom columns vs. thickness and average HAADF-intensity vs. mean collection semi-angle . .	34
3.6. Model 2: QSTEM HAADF-, BF-, and ABF-image	35
3.7. Model 2: Average HAADF-, BF-, and ABF-intensity vs. thickness . . .	36
3.8. Model 2: Average HAADF-intensity of gold and nickel vs. thickness split by collection semi-angle	37

3.9. Model 4: Analysis of different specimen regions	39
3.10. Model 4: Average HAADF-, BF-, and ABF-intensity vs. mean atomic number	40
3.11. Model 5: QSTEM HAADF image	41
3.12. Model 5: Absolute and relative average HAADF-, BF-, and ABF-intensity vs. thickness	41
3.13. Model 5: Average HAADF-, BF-, and ABF-intensity vs. mean atomic number	42
3.14. Model 6: Absolute and relative average HAADF-, BF-, and ABF-intensity vs. mean atomic number for different thicknesses	43
3.15. Model 6: Iso-intensity lines for the absolute average HAADF-intensity as a function of thickness and nickel concentration	45
3.16. Model 6: Iso-contrast lines for the logarithmic relative average HAADF- intensity as a function of thickness and nickel concentration	46
3.17. MC relaxation validation model: Inclined crack of the input with a perfect fcc lattice	47
3.18. MC relaxation validation model: [001] views of the outputs of the four simulation variations using the RTS-potential	48
3.19. MC relaxation validation model: Time evolution of box size and total energy for the four simulation variations using the RTS-potential	49
3.20. MC relaxation validation model: Analysis of the systematic error due to the usage of the single-atom energy	50
3.21. MC relaxation validation model: Time evolution of box size and total energy for single-atom energy calculation using the Zhou-potential . . .	51
3.22. MC relaxation validation model: Histograms of nearest neighbor dis- tances for single-atom energy calculation outputs	52
3.23. Model 7: Nickel concentration modulation in x -direction	53
3.24. Model 7: Monte Carlo time evolution of box size and total energy . . .	54
3.25. Model 7: Views of the crystal in the [001] zone axis after different re- laxation simulations	54
3.26. Model 7: Histograms of nearest neighbor distances for MC and MD simulation outputs	55
3.27. Model 8: Views of the crystal in the [001] zone axis before and after the relaxation simulations	57
3.28. Model 8: Monte Carlo time evolution of box size and total energy . . .	58
3.29. Model 7: QSTEM HAADF images of the relaxed models	60

3.30. Model 7 (MC-relaxed, RTS-potential): Absolute and relative average HAADF-, BF-, and ABF-intensity vs. mean atomic number for different thicknesses	61
3.31. Model 8: QSTEM HAADF images of the relaxed models	62
3.32. QSTEM coherent CBED images of the unrelaxed models 1 and 4 in the [001] zone axis	64
3.33. Model 7: QSTEM coherent CBED images in the [001] zone axis before and after the MC-relaxation using the Zhou-potential	65
3.34. Model 8: QSTEM coherent CBED images in the [001] zone axis before and after the MC-relaxation using the Zhou-potential	65
3.35. HAADF-STEM micrographs of an electrolytically thinned Au _{70.9} Ni _{29.1} specimen at low magnifications	67
3.36. STEM micrographs of an electrolytically thinned Au _{70.9} Ni _{29.1} specimen at medium magnification	67
3.37. HAADF- and BF-STEM micrograph of a 46 x 46 nm ² specimen region, zone axis [001]	68
3.38. HAADF-STEM micrograph of a 46 x 46 nm ² specimen region, zone axis [001], and relative thickness map	69
3.39. HAADF-STEM image of a 64 x 64 nm ² specimen region, zone axis [001], and IFFT of the (000)-satellites in the FFT	70
3.40. FFT of the HAADF image in figure 3.39	70
3.41. 13 x 13 nm ² section of the HAADF-STEM image of figure 3.39(a) and IFFT of the fundamental spots (200), (020), ($\bar{2}$ 00), (0 $\bar{2}$ 0) and their satellites in the FFT image of figure 3.40	71
3.42. HAADF-STEM micrograph of a 33 x 33 nm ² specimen region, zone axis [001]	72
3.43. Line profiles of the three areas marked in figure 3.42	73
3.44. Peak detection and quantification of the 4 x 4 nm ² image section marked in figure 3.42	75
3.45. Maximum, minimum and average grey scale value for the image series regarding the signal-processing parameters contrast and brightness	76
3.46. HAADF-STEM micrograph of a 23 x 23 nm ² specimen region, zone axis [011]	77
3.47. FFT of the HAADF-STEM image in figure 3.46 and the corresponding computed diffraction pattern of an fcc lattice with a parameter of 0.407894 nm in the zone axis [011]	78

List of Figures

3.48. BF-TEM image of a 45 x 45 nm ² specimen region, zone axis [001]	79
3.49. SAED recording in the zone axis [001] and line profile	80
4.1. Juxtaposition of a simulated and an experimental HAADF-STEM image	82
B.2. Simulation demo: Acquire a CIF	118
B.3. Simulation demo: Enlarge model	119
B.4. Simulation demo: Insert impurities 1	120
B.5. Simulation demo: Insert impurities 2	120
B.6. Simulation demo: Screenshot of the QSTEM GUI	121

List of Tables

2.1. Juxtaposition of collection semi-angle ranges for FEI Titan ³ G2 60-300 and QSTEM simulations	8
2.2. Finnis and Sinclair potential: Fcc metal parameters computed for a cut-off radius of 2 lattice constants; Source: Rafii-Tabar & Sutton (1991)	17
2.3. EAM potential: Parameters for gold and nickel; Source: Zhou <i>et al.</i> (2004)	18
3.1. Overview of the nickel impurities in the models used without lattice relaxation	29
3.2. Various data values concerning the MC relaxation validation simulations	52
3.3. Model 7: Statistical key data of the crystal after lattice relaxation	55
3.4. Model 8: Statistical key data of the crystal after lattice relaxation	59

Appendix

A. Code snippets

A.1. Julia

Listing A.1: Code segment: Predefinition of constants

```
1  #= Constants =#
2  kB = 1.38064852E-23; # in J/K; Boltzmann constant (NIST)
3  eC = 1.6021766208E-19; # in C; Elementary charge
4  kBeV = kB/eC; # in eV
5  P = 101325; # in Pa; Average value of virial pressure, which is equal
   to normal pressure (NIST).
6  PeVperA3 = P*1E-30 / eC; # in eV/A^3
7  Temp = 293.15; # in K; Normal temperature (NIST)
8  beta = 1/(kBeV*Temp);
```

Please note that following script will not run as it is. Some variables have to be declared and set beforehand. Furthermore, the input arguments to the energy calculation functions are truncated.

Listing A.2: Code segment: Single Monte Carlo step

```
1  #= Randomly choose an atom or go for a box size adjustment.
2    With ideas from the book by Frenkel and Smit (2002, p.121ff) =#
3  # Set a probability for a box size modification
4  pMCvol = 3/nPart; # Decide whether probability is appropriate
5  if FixateEdgeLengthRatio
6      pMCvol /= 3;
7  end
8  # Choose a random atom
9  N = nPart / (1-pMCvol);
10 atom = round(Integer, floor(rand()*N)+1);
11
```

```

12  #= Single MC step (put this into a loop to perform more steps) =#
13  if atom > nPart
14      ## Box size modification is proposed
15      # Total energy calculation of old coordinates
16      if potential == "RTS"
17          E1 = EPOT_RTS(coords, ...);
18      elseif potential == "Zhou"
19          E1 = EPOT_Zhou(coords, ...);
20      end
21
22      # Random walk in logarithmic volume space,
23      #     either for a single direction or for all 3 directions
24      #     at the same time
25      V0 = L[1]*L[2]*L[3];
26      lnV0 = log(V0);
27      if FixateEdgeLengthRatio
28          dlnV = log(dVrelmax);
29      else
30          dlnV = log(dVrelmax^(1/3));
31      end
32      lnVn = lnV0 + (rand()-0.5) * 2 * dlnV;
33      Vn = exp(lnVn);
34      ratio_1D = Vn/V0;
35      if FixateEdgeLengthRatio
36          ratio_1D ^= 1/3;
37          L *= ratio_1D;
38          coords *= ratio_1D;
39      else
40          direction = rand(1:3);
41          L[direction] *= ratio_1D;
42          coords[direction,:] *= ratio_1D;
43      end
44
45      # Total energy calculation of new coordinates
46      if potential == "RTS"
47          E2 = EPOT_RTS(coords, ...);
48      elseif potential == "Zhou"
49          E2 = EPOT_Zhou(coords, ...);
50      end
51      arg = E2-E1 + PeVperA3*(Vn-V0) - (nPart+1)*log(Vn/V0)/beta;
52
53      # Metropolis decision
54      if exp(-beta*arg) < rand()

```

```

54         # rejected
55         if FixateEdgeLengthRatio
56             coords /= ratio_1D;
57             L /= ratio_1D;
58         else
59             coords[direction,:] /= ratio_1D;
60             L[direction] /= ratio_1D;
61         end
62         NskippedV += 1;
63     else
64         NacceptedV += 1;
65         println(string("Box size changed to ",Vn, " A^3"));
66     end
67 else
68     ## Displacement of a single atom is proposed
69     # "Single atom" energy calculation of old coordinates
70     if potential == "RTS"
71         E1 = EPOT_RTS_sgl(atom, coords, ...);
72     elseif potential == "Zhou"
73         E1 = EPOT_Zhou_sgl(atom, coords, ...);
74     end
75     rnew = 2*drmax.*(rand(nDim)-0.5);
76     coords[:,atom] = coords[:,atom] + rnew;
77
78     # "Single atom" energy calculation of new coordinates
79     if potential == "RTS"
80         E2 = EPOT_RTS_sgl(atom, coords, ...);
81     elseif potential == "Zhou"
82         E2 = EPOT_Zhou_sgl(atom, coords, ...);
83     end
84     arg = E2-E1;
85
86     # Metropolis decision
87     if arg < 0
88         Naccepted += 1;
89     elseif exp(-arg*beta) > rand()
90         Naccepted += 1;
91     else
92         coords[:,atom] = coords[:,atom] - rnew;
93         Nskipped += 1;
94     end
95 end

```

Listing A.3: Function: Total energy calculation using the RTS-potential

```

1  function EPOT_RTS(coords, AtomTypes, cutoff_rel, a, eps, m, n, c, d, L,
    pbcFlag)
2      # init
3      nPart = size(coords,2);
4      V = 0;
5      rho = zeros(nPart);
6      F = 0;
7
8      # Calculate RHO and PHI with cutoff
9      for partA = 1:nPart-1
10         typeA = AtomTypes[partA];           # 1 or 2
11         typeA = Integer(typeA);
12         for partB = (partA+1):nPart
13             typeB = AtomTypes[partB];       # 1 or 2
14             typeB = Integer(typeB);
15             r = coords[:,partA] - coords[:,partB];
16             if pbcFlag == true
17                 # Fix according to periodic boundary
                    conditions
18                 r = distPBC3D(r,L);
19             end
20             norm_r = sqrt(dot(r,r));
21
22             if typeA != typeB
23                 indx = 3;
24             else
25                 indx = typeA;
26             end
27             cutoff = cutoff_rel * a[indx];
28
29             if norm_r < cutoff
30                 aux1 = a[indx]/norm_r; # auxiliary
                    variable 1
31                 aux2 = aux1^(m[indx]);
32                 rho[partB] += aux2;
33                 rho[partA] += aux2;
34                 V += eps[indx] * aux1^n[indx];
35             end
36         end
37     F -= eps[typeA]*c[typeA]*sqrt(rho[partA]);
38 end

```

```

39 E = F + V;
40 return E, V, F
41 end

```

Listing A.4: Function: "Single atom energy" calculation using the RTS-potential

```

1 function EPOT_RTS_sgl(indx_part, coords, AtomTypes, cutoff_rel, a, eps,
    m, n, c, d, L, pbcFlag)
2     typeA = AtomTypes[indx_part];
3     typeA = Integer(typeA);
4     # init
5     nPart = size(coords,2);
6     V = 0;
7     rho = 0;
8     F = 0;
9
10    # Calculate RHO and PHI with cutoff
11    for partB = 1:nPart
12        if partB == indx_part
13            continue;
14        end
15        typeB = AtomTypes[partB]; # 1 or 2
16        typeB = Integer(typeB);
17        r = coords[:,partB] - coords[:, indx_part];
18        if pbcFlag == true
19            # Fix according to periodic boundary conditions
20            r = distPBC3D(r,L);
21        end
22        norm_r = sqrt(dot(r,r));
23
24        if typeA != typeB
25            indx = 3;
26        else
27            indx = typeA;
28        end
29        cutoff = cutoff_rel * a[indx];
30
31        if norm_r < cutoff
32            aux1 = a[indx]/norm_r; # auxiliary variable 1
33            rho += aux1^m[indx];
34            V += eps[indx] * aux1^n[indx];
35        end
36    end
37    F -= eps[typeA]*c[typeA]*sqrt(rho);

```

```

38 E = F + V;
39 return E, V, F
40 end

```

Listing A.5: Function: Total energy calculation using the Zhou-potential

```

1 function EPOT_Zhou(coords, AtomTypes, cutoff_rel, r_e, f_e, rho_e,
  rho_s, alpha, beta, A, B, kappa, lambda, G_n, G, eta, G_e, L,
  pbcFlag)
2     # init
3     nPart = size(coords,2);
4     rho = zeros(nPart);
5     phi = 0;
6     F = 0;
7
8     # Calculate RHO and PHI with cutoff
9     for partA = 1:nPart-1
10        typeA = AtomTypes[partA];          # 1 or 2
11        typeA = Integer(typeA);
12        for partB = (partA+1):nPart
13            typeB = AtomTypes[partB];      # 1 or 2
14            typeB = Integer(typeB);
15            r = coords[:,partA] - coords[:,partB];
16            if pbcFlag == true
17                # Fix according to periodic boundary
18                # conditions
19                r = distPBC3D(r,L);
20            end
21            norm_r = sqrt(dot(r,r));
22
23            if typeA != typeB
24                PseudoLatticePar = sqrt( r_e[typeA] *
25                r_e[typeB] );
26            else
27                PseudoLatticePar = r_e[typeA];
28            end
29            cutoff = cutoff_rel * PseudoLatticePar / sqrt
30                (2) * 2;
31
32            if norm_r < cutoff
33                aux1 = norm_r/r_e[typeA]; # auxiliary
34                # variable 1
35                h_alpha_A = exp( -alpha[typeA] * (aux1
36                -1) );

```

```

32     h_beta_A = exp( -beta[typeA] * (aux1-1)
33         );
34     D_lambda_A = 1 + (aux1 - lambda[typeA])
35         ^20;
36     D_kappa_A = 1 + (aux1 - kappa[typeA])
37         ^20;
38
39     f_A = f_e[typeA] * h_beta_A /
40         D_lambda_A;
41     phi_A = A[typeA] * h_alpha_A /
42         D_kappa_A - B[typeA] * h_beta_A /
43         D_lambda_A;
44
45     rho[partB] = rho[partB] + f_A;
46
47     if typeA != typeB
48         aux1 = norm_r/r_e[typeB]; #
49         auxiliary variable 1
50         h_alpha_B = exp( -alpha[typeB]
51             * (aux1-1) );
52         h_beta_B = exp( -beta[typeB] *
53             (aux1-1) );
54         D_lambda_B = 1 + (aux1 - lambda
55             [typeB])^20;
56         D_kappa_B = 1 + (aux1 - kappa[
57             typeB])^20;
58
59         f_B = f_e[typeB] * h_beta_B /
60             D_lambda_B;
61         phi_B = A[typeB] * h_alpha_B /
62             D_kappa_B - B[typeB] *
63             h_beta_B / D_lambda_B;
64
65         rho[partA] = rho[partA] + f_B;
66         phi = phi + (f_B/f_A * phi_A +
67             f_A/f_B * phi_B)/2;
68     else
69         rho[partA] = rho[partA] + f_A;
70         phi = phi + phi_A;
71     end
72 end
73
74 if rho[partA] >= 1.15*rho_e[typeA]

```

```

60         x = rho[partA]/rho_s[typeA]; # auxiliary
61         F = F + G_e[typeA] * (1 - log(x)^eta[typeA]) *
           x^eta[typeA];
62     else
63         if rho[partA] < 0.85*rho_e[typeA]
64             x = G_n[:,typeA]; # auxiliary
65             y = (rho[typeA]/0.85/rho_e[typeA]-1)
               .^[0; 1; 2; 3]; # auxiliary
66         else
67             x = G[:,typeA]; # auxiliary
68             y = (rho[typeA]/rho_e[typeA]-1).^[0; 1;
               2; 3]; # auxiliary
69         end
70         F = F + sum(x.*y);
71     end
72 end
73 E = F + phi;
74 return E, phi, F
75 end

```

Listing A.6: Function: "Single atom energy" calculation using the Zhou-potential

```

1 function EPOT_Zhou_sgl(indx_part, coords, AtomTypes, cutoff_rel, r_e,
2   f_e, rho_e, rho_s, alpha, beta, A, B, kappa, lambda, G_n, G, eta,
3   G_e, L, pbcFlag)
4     typeA = AtomTypes[indx_part];
5     typeA = Integer(typeA);
6     # init
7     nPart = size(coords,2);
8     rho = 0;
9     phi = 0;
10    F = 0;
11
12    # Calculate RHO and PHI with cutoff
13    for partB = 1:nPart
14        if partB == indx_part
15            continue;
16        end
17        typeB = AtomTypes[partB]; # 1 or 2
18        typeB = Integer(typeB);
19        r = coords[:,partB] - coords[:,indx_part];
20        if pbcFlag == true
21            # Fix according to periodic boundary conditions
22            r = distPBC3D(r,L);

```

```

21         end
22         norm_r = sqrt(dot(r,r));
23
24         if typeA != typeB
25             PseudoLatticePar = sqrt( r_e[typeA] * r_e[typeB
26                                     ] );
27         else
28             PseudoLatticePar = r_e[typeA];
29         end
30         cutoff = cutoff_rel * PseudoLatticePar / sqrt(2) * 2;
31
32         if norm_r < cutoff
33             aux1 = norm_r/r_e[typeA]; # auxiliary variable
34             1
35             h_alpha_A = exp( -alpha[typeA] * (aux1-1) );
36             h_beta_A = exp( -beta[typeA] * (aux1-1) );
37             D_lambda_A = 1 + (aux1 - lambda[typeA])^20;
38             D_kappa_A = 1 + (aux1 - kappa[typeA])^20;
39
40             f_A = f_e[typeA] * h_beta_A / D_lambda_A;
41             phi_A = A[typeA] * h_alpha_A / D_kappa_A - B[
42                 typeA] * h_beta_A / D_lambda_A;
43
44             rho = rho + f_A;
45
46         if typeA != typeB
47             aux1 = norm_r/r_e[typeB]; # auxiliary
48             variable 1
49             h_alpha_B = exp( -alpha[typeB] * (aux1
50                 -1) );
51             h_beta_B = exp( -beta[typeB] * (aux1-1)
52                 );
53             D_lambda_B = 1 + (aux1 - lambda[typeB])
54                 ^20;
55             D_kappa_B = 1 + (aux1 - kappa[typeB])
56                 ^20;
57
58             f_B = f_e[typeB] * h_beta_B /
59                 D_lambda_B;
60             phi_B = A[typeB] * h_alpha_B /
61                 D_kappa_B - B[typeB] * h_beta_B /
62                 D_lambda_B;
63
64         end
65     end
66 }

```

```

53             phi = phi + (f_B/f_A * phi_A + f_A/f_B
                    * phi_B)/2;
54             else
55                 phi = phi + phi_A;
56             end
57         end
58     end
59     if rho >= 1.15*rho_e[typeA]
60         x = rho/rho_s[typeA]; # auxiliary
61         F = F + G_e[typeA] * (1 - log(x)^eta[typeA]) * x^eta[
            typeA];
62     else
63         if rho < 0.85*rho_e[typeA]
64             x = G_n[:,typeA]; # auxiliary
65             y = (rho/0.85/rho_e[typeA]-1).^[0; 1; 2; 3]; #
                auxiliary
66         else
67             x = G[:,typeA]; # auxiliary
68             y = (rho/rho_e[typeA]-1).^[0; 1; 2; 3]; #
                auxiliary
69         end
70         F = F + sum(x.*y);
71     end
72     E_atom = F + phi;
73     return E_atom, phi, F
74 end

```

A.2. MATLAB

The following script was used to generate the models 7 and 8 in XYZ-format. The functions that create fcc supercells and write XYZ-files are appended afterwards.

Listing A.7: Script: Creation of models 7 and 8

```

1 %% Initialization
2 % Material parameters
3 Z1 = 79; % gold: atomic number
4 Z2 = 28; % nickel: atomic number
5 a = 4.07894; % gold: lattice constant, in Angstroems
6
7 % Call CreateFCCSupercell
8 Nx = 15;
9 Ny = 15;

```

```

10 Nz = 15;
11 pbcFlag = true;
12 Crystal = CreateFCCSupercell(a, Nx, Ny, Nz, pbcFlag);
13 NAtoms = size(Crystal, 1);
14
15 % Parameters for later manipulation
16 XMax = max(Crystal(:, 1));
17 CoordsSetX = 0: a/2 : XMax;
18 PosTolerance = 1e-2; % Numerical position tolerance
19
20 %% Model 7
21 period = 9.07;
22 M = 10;
23 cmax = 0.9; % maximum concentration regarding a 100-plane
24 cmin = 0.1; % minimum concentration regarding a 100-plane
25 cNi = ( sin( pi / period * CoordsSetX) ).^M * (cmax-cmin) + cmin;
26
27 % Write char array containing element labels
28 Elements = repmat('Au ', NAtoms, 1);
29 for k = 1:numel(CoordsSetX)
30     % logical array corresponding to a 100-plane
31     L = ( abs(Crystal(:, 1)-CoordsSetX(k)) < PosTolerance );
32     rows = find(L);
33     Nrows = numel(rows);
34     % auxiliary variable for later selection
35     ToExchange = randperm(Nrows, round(Nrows*cNi(k)) );
36     rows = rows(ToExchange);
37     for l = 1:numel(rows)
38         Elements(rows(l), :) = 'Ni ';
39     end
40 end
41 cNi_tot = sum( Elements(:,1) == 'N' ) / size(Elements, 1);
42 disp(['Model 7: Total concentration of Ni = ', num2str(cNi_tot)]);
43
44 % Plot nickel concentration as a function of x
45 figure;
46 p = plot(CoordsSetX, cNi, 'o--');
47 set(p, 'MarkerFaceColor', get(p, 'Color'));
48 xlabel('x / \AA', 'interpreter', 'latex');
49 ylabel('$c_{\text{Ni}}$ / atomic fraction', 'interpreter', 'latex');
50 ylim([0 1]); grid on; grid minor;
51
52 % Write to File

```

```

53 if pbcFlag == true, pbcStr = 'open'; else pbcStr = 'closed'; end
54 comment = ['Au-matrix (fcc, ', num2str(Nx), 'x', num2str(Ny), 'x', num2str(
    Nz), ' unit cells, ', ...
55     pbcStr, '), Ni concentration: ', num2str(cNi_tot), '; sine^', num2str(M
    ), '-shaped, c_min = ', ...
56     num2str(cmin), ', c_max = ', num2str(cmax), ' regarding a 100-plane,
    period = ', ...
57     num2str(period), ' Angstroems'];
58 filename = ['AuNi_', num2str(Nx), 'x', num2str(Ny), 'x', num2str(Nz), ...
59     '_Sine', num2str(M), 'Modulation_cNitot=', num2str(cNi_tot), '_Period='
    , num2str(period), '.xyz'];
60 writeXYZ(filename, Elements, Crystal, comment)
61
62 %% Model 8
63 period = 9.07;
64 cmax = 0.7;
65 cmin = 0.3;
66 cNi = ( sin( pi / period * CoordsSetX) ) .^2 * (cmax-cmin) + cmin;
67
68 % Write char array containing element labels
69 Elements = repmat('Au ', NAtoms, 1);
70 % First, insert the modulation in [100]-direction
71 DyDx = 0.5;
72 D = Ny/3 * a;
73 SecX = 7/10;
74 Xsel = 27;
75 Ysel = 24;
76 for k = 1:numel(CoordsSetX)
77     L = ( abs(Crystal(:,1)-CoordsSetX(k)) < PosTolerance ) & ...
78         ( Crystal(:,2) - DyDx*Crystal(:,1) - D < PosTolerance ) & ...
79         ( Crystal(:,1) - CoordsSetX(Xsel) < PosTolerance );
80     rows = find(L);
81     if ~isempty(rows)
82         Nrows = numel(rows);
83         ToExchange = randperm(Nrows, round(Nrows*cNi(k)) );
84         rows = rows(ToExchange);
85         for l = 1:numel(rows)
86             Elements(rows(l), :) = 'Ni ';
87         end
88     end
89 end
90 % Afterwards, insert the 010-plane
91 L = ( abs(Crystal(:,2)- CoordsSetX(Ysel)) < PosTolerance );

```

```

92 rows = find(L);
93 if ~isempty(rows)
94     Nrows = numel(rows);
95     ToExchange = randperm(Nrows, round(Nrows*cmax) );
96     rows = rows(ToExchange);
97     for l = 1:numel(rows)
98         Elements(rows(l),:) = 'Ni ';
99     end
100 end
101 cNi_tot = sum( Elements(:,1) == 'N' ) / size(Elements, 1);
102 disp(['Model 8: Total concentration of Ni = ', num2str(cNi_tot)]);
103
104 % Write to file
105 if pbcFlag == true, pbcStr = 'open'; else pbcStr = 'closed'; end
106 comment = ['Au-matrix (fcc, ', num2str(Nx), 'x', num2str(Ny), 'x', num2str(
107     Nz), ' unit cells, ', ...
108     pbcStr, '), Ni concentration: ', cNi_tot, '; sine-squared-shaped + xz-
109     plane for high x, c_min = ', ...
110     num2str(cmin), ', c_max = ', num2str(cmax), ' regarding a 100-plane,
111     period = ', ...
112     num2str(period), ' Angstroms'];
113 filename = ['AuNi_', num2str(Nx), 'x', num2str(Ny), 'x', num2str(Nz), ...
114     '_Model8_cNitot=', num2str(cNi_tot), '_Period=', num2str(period), '.xyz
115     '];
116 writeXYZ(filename, Elements, Crystal, comment)

```

Listing A.8: Function: Create fcc supercells / crystals

```

1 function [ Crystal, BoxSize ] = CreateFCCSupercell(a, Nx, Ny, Nz,
2     pbcFlag, origin)
3 %CreateFCCSupercell - This function creates an fcc super cell and
4     returns it in an array.
5 %
6 % [ Crystal, BoxSize ] = CreateFCCSupercell(a, Nx, Ny, Nz, pbcFlag,
7     origin)
8 %
9 % a          1x1 double      lattice constant (the unit of length is a
10     user choice)
11 % Nx        1x1 double      number of unit cells in x-direction
12 % Ny        1x1 double      number of unit cells in y-direction
13 % Nz        1x1 double      number of unit cells in z-direction
14 % pbcFlag*  1x1 logical      periodic boundary conditions (default:
15     false)
16 %
17 %          If pbcFlag is true, the created super cell is a repeatable

```

```

    unit.
12 %           If pbcFlag is false, the super cell is concluded at all
    sides
13 %           and has inversion symmetry regarding the center.
14 % origin*   1x3 double       starting coordinates for replication (
    default: [0 0 0])
15 %           The replication is performed in positive x-, y-, and z-
    direction.
16 %
17 % * optional input argument
18 %
19 % Crystal   ( )x3 double     locations of the atoms
20 %           e.g. [x1 y1 z1
21 %                x2 y2 z2
22 %                ...      ]
23 % BoxSize   1x3 double     (only if pbcFlag is true)
24 %           size of the repeatable unit
25 if nargin < 6
26     origin = [0 0 0];
27 end
28 if nargin < 5
29     pbcFlag = false;
30 end
31
32 %% fcc: atom positions of the basis
33 a0 = [0 0 0];
34 a1 = [0 1 1] * a/2;
35 a2 = [1 0 1] * a/2;
36 a3 = [1 1 0] * a/2;
37
38 %% build repeatable unit cell
39 UnitCell = [origin + a0; origin + a1; origin + a2; origin + a3];
40 N_AtomsUC = size(UnitCell, 1);
41
42 %% build super cell
43 % build cubic lattice
44 if pbcFlag == true
45     Nx = Nx-1; Ny = Ny-1; Nz = Nz-1;
46 end
47 [XX, YY, ZZ] = ndgrid(0:Nx, 0:Ny, 0:Nz);
48 CubicLattice = a * [XX(:), YY(:), ZZ(:)];
49 N_UC = size(CubicLattice, 1);
50 % replicate variables

```

```

51 Crystal = repmat(UnitCell, N_UC, 1);
52 CubicLattice = repelem(CubicLattice, N_AtomsUC, 1);
53 % build crystal
54 Crystal = Crystal + CubicLattice;
55 % with PBC: return size of the repeatable unit
56 % without PBC: delete atoms outside of super cell boundaries
57 if pbcFlag == true
58     BoxSize = a * [Nx Ny Nz];
59 else
60     L = ( Crystal(:,1)==max(Crystal(:,1)) ) | ...
61         ( Crystal(:,2)==max(Crystal(:,2)) ) | ...
62         ( Crystal(:,3)==max(Crystal(:,3)) );
63     Crystal = Crystal(~L, :);
64     BoxSize = nan(1, 3);
65 end
66 NAtoms = size(Crystal, 1); % obsolete

```

Listing A.9: Function: Write crystal data to XYZ-file

```

1 function [] = writeXYZ( filename, Elements, Crystal, comment )
2 %writeXYZ - Write crystal data to XYZ-file
3 %
4 % [] = writeXYZ( filename, Elements, Crystal, comment )
5 %
6 % filename ... full or relative path including the filename; if
7 % extension is not xyz, '.xyz' will be appended
8 % Elements ... N x 2 - char array containing one element symbol per
9 % row
10 % Crystal ... N x 3 - array (numerical) containing one set of
11 % coordinates per row
12 % comment ... comment line to be written to the file's second line
13 tic
14 if nargin < 4
15     comment = '';
16 end
17 NAtoms = size(Elements, 1);
18 if NAtoms ~= size(Crystal, 1)
19     error('Number of element symbols and number of coordinate sets have
20         to be the same!')
21 end
22 if ~isequal( filename(end-3:end), '.xyz' )
23     filename = [filename, '.xyz'];
24 end
25

```

```

22 fileID = fopen(filename, 'w');
23 fprintf(fileID, '%u\r\n', NAtoms);
24 fprintf(fileID, '%s\r\n', comment);
25 for k = 1:NAtoms
26     fprintf(fileID, '%s %12.5f %11.5f %11.5f\r\n', Elements(k,:),
                Crystal(k,:));
27 end
28 fclose(fileID);
29 time = round(toc,1);
30 str = ['Writing to ', num2str(filename), ' lasted ', num2str(time), '
        seconds.'];
31 disp(str)
32 end

```

The following functions can be used to find peaks/valleys in QSTEM output files (*.img). In order to read the files, the unquoted function `binread2D`¹⁹ is used.

Listing A.10: Function: Determine peaks/valleys in QSTEM DF/BF images

```

1 function [intensities, t, dx, dy] = img_peaks(path_img, num_peaks,
        detector_type, ss_fwhm, maxradius)
2 %IMG_PEAKEs - QSTEM image peaks/valleys (for .img)
3 %
4 % num_extrema (1x2 array): e.g.: [5 5]
5 % detector_type (string): 'HAADF', 'BF', 'ABF'
6 %
7 % finding maxima or minima depending on detector type
8
9 if ~isempty(findstr('BF', detector_type))
10     find_min = true;
11 else
12     find_min = false;
13 end
14
15 [intensities, t, dx, dy] = img_peakquant(path_img, num_peaks, find_min,
        ss_fwhm, maxradius);

```

Listing A.11: Function: Quantify peaks/valleys in QSTEM DF/BF images

```

1 function [values_max, t, dx, dy] = img_peakquant(file, num_sectors,
        find_min, ss_fwhm, maxradius)
2 %IMG_PEAQQUANT - QSTEM image peak/valley quantifier (for .img)
3

```

¹⁹part of the QSTEM source code

```
4 %% user prompts
5 % get image path via image dialog box
6 if nargin<1
7     [file, path] = uigetfile({'*.img'}, 'Select File to Open');
8     file = [path, file];
9 end
10 % get image specifications
11 if nargin<2
12     num_sectors = prompt_num_sectors;
13 end
14 % find minimum?
15 if nargin<3
16     find_min = false;
17 end
18 % source size
19 if nargin<4
20     ss_fwhm = prompt_source_size;
21 end
22 % maximum radius for summation
23 if nargin<5
24     maxradius = 2.3;
25 end
26
27 %% investigation of image
28 % read
29 [img_grey, t, dx, dy] = binread2D(file);
30 img_height = size(img_grey, 1);
31 img_width = size(img_grey, 2);
32 % source size correction
33 if ss_fwhm > 0
34     img_grey = img_sscorr(img_grey, dx, dy, ss_fwhm, 1);
35 end
36 % split image
37 [secs_heights, secs_widths] = GetSectionHW(img_height, img_width,
38     num_sectors);
39 sections = mat2cell(img_grey, secs_heights, secs_widths);
40 % find and quantify peaks/valleys
41 method = 1;
42 switch method
43     case 0
44         % pick absolute maximum
45         if find_min == false
46             func = @(x) max(x(:));
```

```

46     else
47         func = @(x) min(x(:));
48     end
49     values_max = cellfun(func, sections);
50 case 1
51     % sum up within a certain radius
52     for k = 1:numel(sections)
53         sec = sections{k};
54         if find_min == false
55             [peaky, peakx] = find(sec == max(sec(:)));
56         else
57             [peaky, peakx] = find(sec == min(sec(:)));
58         end
59         [ly, lx] = size(sec);
60         [xx, yy] = meshgrid(1:lx, 1:ly);
61         MaskCircular = logical( (xx-peakx).^2+(yy-peaky).^2 <=
            maxradius^2 );
62         values_max(k) = sum(sec(MaskCircular));
63     end
64 end

```

The next two functions are used by `img_peakquant`. The first one (`img_sscorr`) performs a correction of simulated QSTEM images accounting for the shape of the intensity distribution in the probe. The used option applies a convolution of the input image with a Gaussian distribution. The second one (`GetSectionHW`) returns partial section heights and widths resulting from splitting a matrix, or image respectively, into smaller rectangular sections.

Listing A.12: Function: Source size correction on image data

```

1  function [ img_out ] = img_sscorr( img, dx, dy, ss_fwhm, option )
2  %IMG_SSCORR - Source size correction for *.img
3  %
4  %   img_out = img_sscorr( img_in, dx, dy, ss_fwhm, option )
5  %
6  %   img ... image data (pre-correction)
7  %   dx, dy ... pixel distance (in Angstroem)
8  %   ss_fwhm ... full width at half maximum of source size (in Angstroem
9  %   option = 1, (default) ... correction copied from QSTEM/showimage
10 %   option = 2 ... correction via imgaussfilt
11 if nargin < 4
12     ss_fwhm = 0.7; % in Angstroem

```

```

13 end
14 if nargin < 5
15     option = 1;
16 end
17
18 if option == 2
19     sigma = ss_fwhm / (2*sqrt(2*log(2)));
20     img_out = imgaussfilt(img, sigma/dx*1.005);
21 else
22     % ---- BEGIN ---- source-size-correction
23     % Code taken from QSTEM/showimage,
24     % Source available from https://github.com/QSTEM/QSTEM/blob/master/
25     % GUI_Matlab/showimage.m, retrieved on 19th of December, 2016
26
27     ss = ss_fwhm/(sqrt(-log(0.5))*2); % = ss/1.66510922231540;
28
29     [Ny,Nx] = size(img);
30
31     NxMid = floor(Nx/2)+1;
32     NyMid = floor(Ny/2)+1;
33     [qx,qy] = meshgrid((-NxMid+[1:Nx])/(Nx*dx), (-NyMid+[1:Ny])/(Ny*dy))
34     ;
35     img_out = real(ifft2( fft2(img) .* ifftshift(exp(-((pi*ss)^2*(qx
36     .^2+qy.^2)))) ));
37     % ---- END ---- source-size-correction
38 end
39 end

```

Listing A.13: Function: Get height and width of rectangular image sections

```

1 function [ secs_heights, secs_widths ] = GetSectionHW( N, M,
2     num_sectors )
3 %GetSectionHW
4 % This function calculates integer height and width of rectangular
5 % sections of an image / generic matrix which arise from splitting it
6 % into a given number of sectors.
7 %
8 % N ... Image height
9 % M ... Image width
10 % num_sectors ... 2 x 1 - or 1 x 2 - array (numeric)
11 secs_limits1 = round( img_height/num_sectors(1) * (1:num_sectors(1)) );
12 secs_limits2 = round( img_width/num_sectors(2) * (1:num_sectors(2)) );
13 secs_heights = secs_limits1 - [0, secs_limits1(1:end-1)];
14 secs_widths = secs_limits2 - [0, secs_limits2(1:end-1)];

```

14 **end**

The successional script reproduces the representation of QSTEM/showimage

Listing A.14: Script: Plot a QSTEM image

```

1 [file, path] = uigetfile('Z:\sims\*.*.');
2 [I, t, dx, dy] = binread2D([path, file]);
3
4 IsRealImage = false;
5 if IsRealImage
6     ss_fwhm = 0.7;
7     I = img_sscorr( I, dx, dy, ss_fwhm );
8     xlab = '$x$ / \AA';
9     ylab = '$y$ / \AA';
10    I = flipud(I);
11 else
12    % CBED images: no source size correction, but log scale
13    I = log(I+1-min(I(:)));
14    xlab = '$q_x$ / \AA$^{-1}$';
15    ylab = '$q_y$ / \AA$^{-1}$';
16    maxI = max(I(:));
17    I(I==0) = maxI;
18    % dkx and dky are not correct in QSTEM *.img files or not correctly
19    % read
20    % by binread2D. Thus, request user input.
21    dx = eval( cell2mat(inputdlg('Set dkx and dky (1/A): ', '', 1, {'
22    1/230'})) );
23    dy = dx;
24 end
25 [Ny_I, Nx_I] = size(I);
26 x = 0:(Nx_I-1);
27 x = x.*dx;
28 y = 0:(Ny_I-1);
29 y = y.*dy;
30 if ~IsRealImage
31    % CBED images: centering regarding the undeflected beam
32    x = x - x(floor(Nx_I/2+1));
33    y = y - y(floor(Ny_I/2+1));
34 end
35 figure
36 imagesc(x, y, I)
37 axis equal

```

```

37 colormap(gray)
38 xlabel(xlab, 'interpreter', 'latex')
39 ylabel(ylab, 'interpreter', 'latex')
40 xlim([x(1) x(end)])
41 ylim([y(1) y(end)])

```

Last, the function quoted below calculates the empirical autocorrelation function of a time series according to equation (2.27).

Listing A.15: Function: Empirical autocorrelation function

```

1 function [rhoE, t] = rhoE(x, tmax)
2 %rhoE - Empirical autocorrelation function of a time series
3 %
4 % [rhoE, t] = rhoE(x,tmax)
5 %
6 % x ... time series of a scalar
7 % tmax ... maximum time difference used in the calculation
8 %
9 % rhoE ... empirical autocorrelation function
10 % t ... corresponding time differences
11 N = numel(x);
12 if size(x,2) == 1
13     x = x.';
14 end
15 if tmax > N
16     error('tmax must not exceed N!')
17 end
18 t = 0:tmax-1;
19 xsq = x.^2;
20
21 sum_xj = fliplr(cumsum(x));
22 sum_yj = fliplr(cumsum(fliplr(x)));
23 sum_xjsq = fliplr(cumsum(xsq));
24 sum_yjsq = fliplr(cumsum(fliplr(xsq)));
25 %% FFT for the correlation function sum_{j=1}^{N-t} (xj*yj)
26 L = N + tmax;
27 ft_x = fft(x,L);
28 sum_xjyj = ifft(abs(ft_x).^2);
29
30 %% Cutting away indices higher than tmax
31 sum_xj = sum_xj(1:tmax);
32 sum_yj = sum_yj(1:tmax);
33 sum_xjsq = sum_xjsq(1:tmax);

```

```

34 sum_yjsq = sum_yjsq(1:tmax);
35 sum_xjyj = sum_xjyj(1:tmax);
36 xbar = 1 ./ (N-t) .* sum_xj;
37 ybar = 1 ./ (N-t) .* sum_yj;
38
39 rhoE = ( sum_xjyj - ybar.*sum_xj - xbar.*sum_yj + (N-t).*xbar.*ybar )
    ./ ...
40 ( (sum_xjsq - (N-t).*xbar.^2) .* (sum_yjsq - (N-t).*ybar.^2) )
    .^(1/2);

```

B. How to get QSTEM simulations done (* .cif to * .img)

In this section, I present a detailed explanation of the preliminary work necessary in order to start simulating STEM images with QSTEM. Furthermore, a step-by-step demonstration that should enable a first-time user to perform simulations is given.

*.cif

(a) Specify a query

Coll. Code	HMS	Struct. Form.	Struct. Type	Title	Authors	Reference
43493	F m-3 m	Cu	fcc(ccp)-Cu	Lattice parameter determinations with an X-ray spectrometer by the Debye-Scherrer method and the effect of specimen condition	Otto, H.M.	Journal of Applied Physics (1961) 32, p1536-p1546
52256	F m-3 m	Cu	fcc(ccp)-Cu	Precision measurements of crystal parameters	Owen, E.A.; Yates, E.L.	Philosophical Magazine, Serie 7 (1936-40; 1955) (1933) 15, p472-p488
53246	F m-3 m	Cu	fcc(ccp)-Cu	Accurate evaluation of lattice parameters of alpha-brasses	Srinavasa Rao, S.; Anantharaman, T.R.	Current Science (1963) 32, p262-p263

(b) Download a CIF

Figure B.2.: How to acquire a specific CIF from the ICSD produced by FIZ Karlsruhe

structure Database (ICSD), which is currently produced by FIZ Karlsruhe - Leibniz Institute for Information Infrastructure. Note that the website is not freely accessible.

To start with, one can use a Crystallographic Information File (CIF). This file format was published by the International Union of Crystallography (IUCr²⁰) in 1990. It was described as "a general, flexible and easily extensible free-format archive file" that "can be edited by a simple text editor" by Hall *et al.* (1991) and its outstanding features were emphasized by Brown & McMahon (2002). A large number of CIFs for a wide variety of chemical composition is gathered in the Inorganic Crystal Structure Database (ICSD), which is currently produced by FIZ Karlsruhe - Leibniz Institute for Information Infrastructure. Note that the website is not freely accessible.

²⁰www.iucr.org

Demo - step 1:

If we exemplarily wish to download a CIF of a copper unit cell, we will navigate to icsd.fiz-karlsruhe.de and fill 'Cu' in the form field *Composition*. The space character between the element identifiers is mandatory. We fill '1' in the field *Number of elements* and click on the button *Run Query* close to the right upper corner (see figure B.2(a)). In contrast, if we liked to search for any 2-element-compositions containing oxygen, we would need to put 'O' and '2' in the corresponding fields.

However, after the query has been performed, we get to see a listing of database entries matching your request. We choose one of them and download it via clicking on the floppy disk button (see figure B.2(b)).

Crystal-modeling

Once a CIF has been obtained, the file, which typically contains a single unit cell, can be manipulated using a crystal/molecule modeling software package, e.g. Avogadro²¹, CrystalMaker, Crystal Studio²², or VESTA²³. Here, the usage of any software package regarding crystal manipulation other than CrystalMaker is not covered.

Demo - step 2:

We launch CrystalMaker and open the downloaded CIF. We select *Transform* from the menu bar, choose *Set Range...*, set some arbitrary, though not too large values (Your computer might get overstrained, which is not necessary for this purpose.) for *Minimum* and *Maximum* in *x*, *y*, and *z* (see figure B.3) and press *Apply*. While pressing Ctrl, using the left mouse button and the scroll wheel are the easiest ways to rotate and resize the view of our super cell. Now we save the result as a CMDF²⁴, which, in contrast to CMMF²⁵, contains unit cell and symmetry information.

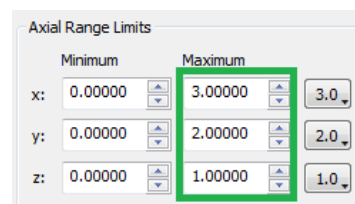


Figure B.3.: Set range of a super cell to enlarge the model

²¹avogadro.cc

²²www.crystalsoftcorp.com

²³jp-minerals.org/vesta

²⁴CrystalMaker Crystal File

²⁵CrystalMaker Molecule File

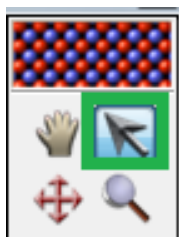


Figure B.4.:
Select Arrow
Tool

As our next goal, we would like to insert a single substitutional foreign atom. In order to achieve that, we select *Transform* from the menu bar, choose *Molecule to Crystal...* and press *Convert*. We switch to the *Arrow Tool* in the Tools Palette (see figure B.4), left-click an atom, select *Selection, Atoms, Change Atom Type...*, fill in the element symbol of the desired foreign atom, label it and give it a different color (see figure B.5). The possibility to set an arbitrary radius is a visual, though physically irrelevant, gimmick. Press *OK* and take a look at our constructed point defect. We save the model as a CMMF, which, as stated above, contains no unit cell or symmetry information. Additionally, change an atom type without converting the crystal to a "molecule" before and inspect the result.

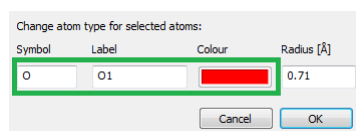


Figure B.5.: Introduce a substitutional foreign atom into a crystal

***.xyz (or *.xtl optionally)**

After creating the desired structure, one exports the model to an XYZ²⁶- or XTL²⁷-file, alternatively.

Demo - step 3:

We export the model via *File, Export* and *XYZ*.

***.cfg**

Arrived at an XYZ-/XTL-file, one converts it to a QSTEM Atomic Configuration File (CFG) with the tool "Convert to CFG" included in the QSTEM software package.

Demo - step 4:

We launch 'Convert to CFG' in our QSTEM (start menu) folder and adjust shift

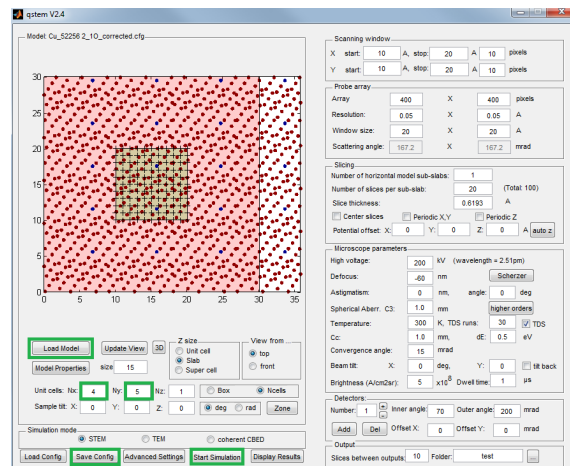
²⁶The format is not strictly defined (yet), but, as labeled *xyz*, it contains the values of the Cartesian coordinates of every atom in the structure. Just take a look at it with a text editor.

²⁷used e.g. by VESTA

vector as well as super cell size on demand. Changes of the latter are mostly used if you wish your model to be replicated by QSTEM afterwards, because the displacement of replicant super cells with respect to the original one can be modified this way.

QSTEM, *.qsc

Finally, one loads the CFG-file into QSTEM, sets the numerous parameters and saves the configuration to a QSTEM Simulation Config File (QSC). A simulation using the stored QSC can be performed on any computer, although the CFG-file must have the same path as it had when it was originally loaded.



Demo - step 5:

We launch QSTEM. As marked in figure B.6, we press *Load Model*, select the generated *.cfg, adjust some microscope and/or model parameters (feel free to try anything out!), save a QSC-file via *Save Config* and are now ready to run.

Figure B.6.: How to start a simulation in QSTEM